AD-A113 086   CHICAGO UNIV IL DEPT OF GEOPHYSICAL SCIENCES   F/G 4/2
THEORETICAL STUDIES OF SQUALL-LINE TYPE AND TORNADO-LIKE DISTUR--ETC(U)
DEC 81 H L KUO, W H RAYMOND, K SEITTER   F19628-80-C-0012
UNCLASSIFIED   AFGL-TR-82-0005   NL

1 of 2

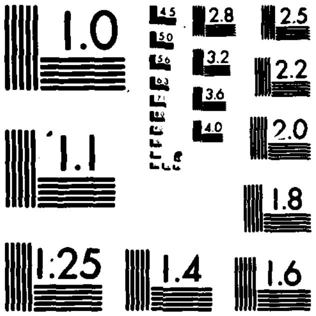

MICROCOPY RESOLUTION TEST CHART

Unclassified
SECURITY CLASSIFICATION OF THIS PAGE (When Data Entered)

REPORT DOCUMENTATION PAGE	READ INSTRUCTIONS BEFORE COMPLETING FORM
1. REPORT NUMBER AFGL-TR-82-0005	2. GOVT ACCESSION NO. AD-A113C86
	3. RECIPIENT'S CATALOG NUMBER
4. TITLE (and Subtitle) THEORETICAL STUDIES OF SQUALL-LINE TYPE AND TORNADO-LIKE DISTURBANCES IN THE ATMOSPHERE	5. TYPE OF REPORT & PERIOD COVERED Final Report Nov 1979 to Nov 1981
	6. PERFORMING ORG. REPORT NUMBER
7. AUTHOR(s) H.L. Kuo, W. H. Raymond, K. L. Seitter	8. CONTRACT OR GRANT NUMBER(s) F19628-80-C-0012
9. PERFORMING ORGANIZATION NAME AND ADDRESS Department of Geophysical Sciences The University of Chicago Chicago, Illinois 60637	10. PROGRAM ELEMENT, PROJECT, TASK AREA & WORK UNIT NUMBERS 61102F 2310G2AL
11. CONTROLLING OFFICE NAME AND ADDRESS Air Force Geophysics Laboratory Hanscom AFB, Massachusetts 01731 Monitor/Samuel Yee/LYP	12. REPORT DATE 16 December 1981 13. NUMBER OF PAGES 134
14. MONITORING AGENCY NAME & ADDRESS(if different from Controlling Office)	15. SECURITY CLASS. (of this report) Unclassified 15a. DECLASSIFICATION/DOWNGRADING SCHEDULE

16. DISTRIBUTION STATEMENT (of this Report)

Approved for public release; distribution unlimited

17. DISTRIBUTION STATEMENT (of the abstract entered in Block 20, if different from Report)

18. SUPPLEMENTARY NOTES

19. KEY WORDS (Continue on reverse side if necessary and identify by block number)

Squall line type storms
Vortex motions

20. ABSTRACT (Continue on reverse side if necessary and identify by block number)

A multi-two-dimensional squall line model is constructed by approximating the three-dimensional variable by the sum of three components which can be considered as its projections in the three orthogonal planes when taken alone, and use the maturely dependent sets of two-dimensional equations to represent the three-dimensional flow. Condensation and precipitation processes are also included. A wide variety of numerical simulations may be performed with this model. The question of the upshear slope of the squall line type thunderstorm is investigated separately by using the pure two- → 2nd page

DD FORM 1 JAN 73 1473

Unclassified
SECURITY CLASSIFICATION OF THIS PAGE (When Data Entered)

dimensional version of the model. Influence of the fictitious side boundaries is minimized by the use of a radiation condition based on the phase velocity of the disturbance.

The question of the conditions that lead to the development of the two-cell type vortex motion with descending motion at the center is attacked by extending Kuo's similarity solutions to higher order in z.

Preface to the final report. - H. L. Kuo, the principal investagator

As stated in our renewal proposal, our tasks during the first year of this contract are synthesis of shallow and deep convection systems and formulation of tractable dynamic models of the squall-line type thunderstorms, and the tasks during the second year are to analyze the influences of the vertical shear of the mean wind on the organization of these meso-scale thunderstorms and the integration of the squall-line models formulated, plus investigations of other subjects related to severe storms. We have by and large followed this research scheme and the results we obtained are presented in the four papers included in this final report.

It is well known that all squall-line type thunderstorms are prominently two-dimensional in structure even though new cells often form at the leading edge and old cells decay at the trailing edge along the line, so that the variation in the direction parallel to the squall-line is also of some importance. Further, the velocity in the direction parallel to the squall-line is often also of importance both for the generation and for the development of the storm system and it usually varies significantly both in the direction parallel to the line and perpendicular to the line, as examplified by the moisture leaden southerly current from the gulf of Mexico for most of the squall-line type storms in mid-west United States. In order to include these effects and yet avoid the use of the very complicated and time consuming three-dimensional model, a multi-two-dimensional model has been developed by the principal investigator in which the variable $\chi(x,y,z,t)$ is approximated by the sum of its projections $\chi_1(x,z,t)$ and $\chi_2(y,z,t)$ on the xz- and the yz-planes. A third component $\chi_3(x,y,t)$ can also be added to the system to represent the prominent z - independent part of the flow field such as the rotational motion in tornadoes. We shall use this model to investigate the various aspects of the squall-line type storms, especially those aspects which are related to the development and the structure of these storms and the formation of new disturbances. This model and the results obtained from it up to now are presented in paper (1).

One very characteristic and dynamically also very important feature of the squall-line type thunderstorm is that the updraft and downdraft usually slope upward in the direction opposite to the vertical shear of the mean wind. Even though this aspect of the squall-line structure has been discussed by many dynamic meteorologist, no satisfactory explanation has yet been found for it. Here we shall consider it as one of our major goals of this research. Our analyses on the various factors which influence the vertical structure of these prominently two-dimensional squall-line type storms indicate that this arrangement is the result of water loading and precipitation because, with the upshear slope, the precipitation process relieves the liquid and solid water loading from the updraft and turns the downward drag exerted by them to an accelerating force for the downdraft, thereby making the storm system most efficient energetically whereas with either a vertical or a downshear slope the downward drag always tends to destroy the updraft. It is also evident that a sloped updraft-downdraft can be maintained in convective systems only when a vertically shearing mean wind is present. This conclusion can also be reached from their influences on the vorticity field. We consider the verification of this hypothesis as one of our major goals of our research, and shall treat it both as an integral part of the general squall-line development problem by the use of our multi-two-dimensional squall-line model in work (1) in the future and directly as a separate problem by the use of the much simpler purely two-dimensional model. This latter approach is more advantages so far as the upshear slope problem is concerned because it addresses only to this problem and we have adopted it in paper (2). In this approach, we start from a finite amplitude disturbance with updraft and downdraft adjacent to each other and let it evolve into a steady state with the influences of liquid and solid water loading and evaporation included, and try to find out whether an upshear slope will result. A case study of a real squall-line type storm is also included in this research both for demonstrating the nearly two-dimensional structure of the real storm and to illustrate the unstable stratification of the atmosphere under which the storm develops.

As in all meso-scale disturbance modellings, we always have to deal with the boundary conditions at the side boundaries. Since no real boundary is present,any boundary condition imposed may generate some ficticious responses. It is thought that the radiative boundary condition which allows outward propagating disturbances to go out un-impedded will do least damage to the results. Paper (3) is concerned with the most advantageous treatment of the conditions at these open boundaries.

Aside from these works which deal either with the dynamics of the squall-line type disturbance directly or is concerned with the most advantageous treatment of the open boundary conditions used in the modeling, Dr. Raymond and I have also worked on higher order similarity solution for the tornado-like vortex, which represents an extension of my first order similarity solution and allows the inclusion of the influence of variation of the horizontal velocities with height on the vortex structure. The results of this study is presented in paper (4).

Contents

Multi-Two-Dimensional Model of Squall Line Type Disturbances

Abstract

A multi-two dimensional dynamic model has been formulated for the simulation of the development of squall line type thunderstorms by approximating every flow variable by the sum of three components defined by averaging in y, x and z directions respectively, so that every component taken by itself represents a purely two-dimensional system. This system of equations is integrated from an initial state characterized by the geostrophic basic currents $U(y,z)$ and $V(x,z)$ to 24 hours under four different conditions, namely, cases 1a and 2a are from the dry and wet versions of the purely two-dimensional model while cases 1b and 2b are from the dry and wet versions of the coupled two-dimensional model. It is found that in general the disturbance evolves to a cold front type, and the variation of the flow variables in the direction parallel to the squall line enhances the intensity. Further, the vertical velocities in the xz-plane usually show a double maxima, one at the 2.5 km level and another at 7 km, while in the yz-plane the disturbance consists of a number of cells with a horizontal scale of about 400 km.

1. Introduction

It is well known that the structure of the squall line is predominantly two-dimensional but some of the very important behaviors of the system, such as the formation of new convection cells at the leading edge and the supply of moist air to the storm, are also significantly influenced by the variation of the flow variables in the direction parallel to the squall line. In order to take these effects into account and yet avoid the use of the very time consuming completely three-dimensional model, a multi-two dimensional dynamic model has been formulated on the basis of the mean flow condition defined by the averages of the flow variables in y, x and z- directions, which are taken as parrallel and perpendicular to the squall line and in vertical direction, respectively. That is to say, we replace or approximate the flow variable χ by the variable χ_S defined by

$$\chi_S(x,y,z,t) = \chi_1(x,z,t) + \chi_2(y,z,t) + \chi_3(x,y,t), \qquad (1)$$

and take χ_1, χ_2 and χ_3 as the averages of $\chi(x,y,z,t)$ in y- and x- and z-directions, respectively, viz.,

$$\chi_1 = \chi = \frac{1}{D}\int_{y_1}^{y_1 + D_1} \chi\, dy,\ \chi_2 = \bar{\chi} = \frac{1}{D_2}\int_{x_1}^{x_1 + D_2} \chi\, dx,\ \chi_3 = \chi = \frac{1}{H}\int_{0}^{H} \chi\, dz \qquad \text{(1a-c)}$$

Through this splitting procedure, every dynamic equation is replaced by three seperate equations containing the two-dimensional variables in the particular direction plus average values of other quantities.

2. The Governing Equations

On averaging the equations of motion, the heat equation, the water vapor and cloud liquid water mixing ratio equations and the anelastic continuity equation in x-, y- and z- directions we then obtain the following set of equations

$$D_j u_j = f v_j - \frac{\partial \pi_j}{\partial x} + \frac{\partial}{\partial x_i}\left(\nu_i \frac{\partial u_j}{\partial x_i}\right) , \tag{2}$$

$$D_j v_j = - f u_j - \frac{\partial \pi_j}{\partial y} + \frac{\partial}{\partial x_i}\left(\nu_i \frac{\partial u_j}{\partial x_i}\right) , \tag{3}$$

$$D_j w_j = g\left(\frac{\theta_{vj}}{\theta o} - c_j\right) - \frac{\partial \pi_j}{\partial z} + \frac{\partial}{\partial x_i}\left(\nu_i \frac{\partial w_j}{\partial x_i}\right) , \tag{4}$$

$$D_j \theta_j = \frac{L}{C_p}\left(\frac{P}{p}\right)^{\kappa} \delta_j + \frac{\partial}{\partial x_i}\left(\nu_{ei} \frac{\partial \theta_j}{\partial x_i}\right) , \tag{5}$$

$$D_j q_j = - \delta_j + \frac{\partial}{\partial x_i}\left(\nu_{ei} \frac{\partial q_j}{\partial x_i}\right) , \tag{6}$$

$$D_j C_i = \delta_j + \frac{\partial}{\partial x_i}\left(\nu_{ei} \frac{\partial c_j}{\partial x_i}\right) , \tag{7}$$

$$\frac{\partial \rho_0 u_1}{\partial x} + \frac{\partial \rho_0 w_1}{\partial z} = 0 , \tag{8a}$$

$$\frac{\partial \rho_0 v_2}{\partial y} + \frac{\partial \rho_0 w_2}{\partial z} = 0 , \tag{8b}$$

$$\frac{\partial u_3}{\partial x} + \frac{\partial v_3}{\partial y} = 0 , \tag{8c}$$

where the diffusion terms involving the repeated index i imply summation over $i = 1,2,3$. Here $\pi = p/\rho_o$, $\kappa = R/c_p$, $\rho_o = \rho_o(z)$ is the undisturbed density of the air, θ is potential temperature and $\theta_o(z)$ is its undisturbed value, $\theta_v = \theta + 0{\cdot}61q\left(\frac{P}{p}\right)^{\kappa}\theta$ is the virtual potential temperature, q and c are the water vapor and cloud liquid water mixing ratios, ν_i and ν_{ei} are the eddy viscosity and eddy conduction coefficients in x_i -direction, L is the latent heat of condensation and sublimation, δ is the condensation rate, $j = 1,2,3$ and

$$D_1X_1 = X_{1t} + (u_1 + \overline{u}_2 + \overline{u}_3)\,X_{1x} + (w_1 + \overline{w}_2)\,X_{1z} + v_1'\,\overline{(X_2 + X_3)}_y \,, \tag{9a}$$

$$D_2X_2 = X_{2t} + (v_2 + \bar{v}_1 + \bar{v}_3)\,X_{2y} + (w_2 + \bar{w}_1)\,X_{2z} + u_2'\,\overline{(X_1 + X_3)}_x \,, \tag{9b}$$

$$D_3X_3 = X_{3t} + (u_3 + \hat{u}_1 + \hat{u}_2)\,X_{3x} + (v_3 + \hat{v}_1 + \hat{v}_2)\,X_{3y} \,, \tag{9c}$$

where X stands for any one of the dependent variables u,v,w,θ and q and the subscripts t,x,y,z denote partial differentiations, and $v_1' = v_1 - \overline{v}_1$, $u_2' = u_2 - \bar{u}_2$. For simplicity, we shall limit ourselves in this investigation to the xz-plane and yz-plane systems only by assuming $X_3 = 0$. According to the continuity equations (8a) and (8b), the velocities u_1 and w_1 and v_2 and w_2 can be expressed in terms of the momentum stream functions ψ_1 and ψ_2, respectively, viz.,

$$u_1 = -\alpha_o\,\psi_{1z},\quad w_1 = \alpha_o\,\psi_{1x}\;; \tag{10a}$$

$$v_2 = -\alpha_o\,\psi_{2z},\quad w_2 = \alpha_o\,\psi_{2y}\,, \tag{10b}$$

where $\alpha_o = 1/\rho_o$. For convenience, we shall eliminate the pressure gradient terms in (2) - (4) by cross-differentiation between (2) and (4) and between (3) and (4) to obtain the equations for the vorticities η_1 and η_2 in y- and x-directions, and write the two sets of prognostic equations as

$$\eta_{1t} = \mathscr{L}_1(\eta_1) + u_{1x}\,\overline{u}_{2z} + u_{1z}\,\overline{w}_{2z} - v_{1x}\,\overline{w}_{2y} + (v_1'\,\overline{u}_{2y})_z + \frac{g}{\theta_o}\theta_{v1x} - f\,v_{1z} - gC_{1x} + \nu\mathscr{D}_1^2\,\eta_1 \,. \tag{11}$$

$$v_{1t} = -\mathscr{L}_1(v_1) + \sigma_z w_1 v_1 - f\,u_1 - v_1'\,\overline{v}_{2y} + \nu\mathscr{D}_1{}^2 v_1 \,, \tag{12}$$

$$\theta_{1t} = -\mathscr{L}_1(\theta_1) + \sigma_z w_1\theta_1 - v_1'\,\overline{\theta}_{2y} + \nu_e\mathscr{D}_1{}^2\theta_1 + \frac{L}{c_p}\left(\frac{P}{p}\right)^{\kappa}\delta_1 \,, \tag{13}$$

$$q_{1t} = -\mathscr{L}_1(q_1) + \sigma_z w_1 q_1 - v_1'\,\overline{q}_{zy} + \nu_e\mathscr{D}_1{}^2 q_1 - \delta_1 \,, \tag{14}$$

$$C_{1t} = -\mathscr{L}_1(C_1) + \sigma_z w_1 C_1 - v_1'\,\overline{C}_{2y} + \nu_e\mathscr{D}_1^2 C_1 + \delta_1 \,, \tag{15}$$

$$\eta_{2t} = -\mathscr{L}_2(\eta_2) + v_{2y}\,\bar{v}_{1z} + v_{2z}\bar{w}_{1z} - u_{2y}\,\bar{w}_{1x} + (u_2'\,\overline{v}_{1x})_z + \frac{g}{\theta_0}\theta_{v2y} + f\,u_{2z} - gC_{2y} + \nu\mathscr{D}_2^2\,\eta_2 \,, \tag{16}$$

$$u_{2t} = -\mathscr{L}_2(u_2) + \sigma_z w_2 u_2 + f v_2 - u_2' \bar{u}_{1x} + \nu \mathscr{D}_2^2 u_2 , \tag{17}$$

$$\theta_{2t} = -\mathscr{L}_2(\theta_2) + \sigma_z w_2 \theta_2 - u_2' \bar{\theta}_{1x} + \nu_e \mathscr{D}_2^2 \theta_2 + \frac{L}{c_p} \left(\frac{p}{p}\right)^{\kappa} \delta_2 , \tag{18}$$

$$q_{2t} = -\mathscr{L}_2(q_2) + \sigma_z w_2 q_2 - u_2' \bar{q}_{1x} + \nu_e \mathscr{D}_2^2 q_2 - \delta_2 . \tag{19}$$

$$c_{2t} = -\mathscr{L}_2(c_2) + \sigma_z w_2 c_2 - u_2' \bar{c}_{1x} + \nu_e \mathscr{D}_2^2 c_2 + \delta_2 , \tag{20}$$

where δ_1 and δ_2 are the contributions of the two two-dimensional flow fields to the total condensation rate $\sigma \doteq \sigma_S = \sigma_1 + \sigma_2$, L is the latent heat of condensation and sublimation and η_1, η_2, σ_z and the operators $\mathscr{L}_1, \mathscr{L}_2, \mathscr{D}_1^2$ and $\mathscr{D}_2^2$ are given by

$$\eta_1 = w_{1x} - u_{1z} = \alpha_o(\psi_{1xx} + \psi_{1zz} + \sigma_z \psi_{1z}) , \tag{21a}$$

$$\eta_2 = w_{2y} - v_{2z} = \alpha_o(\psi_{2yy} + \psi_{2zz} + \sigma_z \psi_{2z}) , \tag{21b}$$

$$\sigma_z = \rho_o^{-1} \rho_{oz} , \mathscr{D}_1^2 \chi_1 = K\chi_{1xx} + \chi_{1zz}, \mathscr{D}_2^2 \chi_2 = K\chi_{2yy} + \chi_{2zz}, \tag{21c,d,e}$$

$$\mathscr{L}_1(\chi_1) = \psi_{1x}(\alpha_o \chi_1)_z - \psi_{1z}(\alpha_o \chi_1)_x + \overline{u_2} \chi_{1x} + \overline{w_2} \chi_{1z} , \tag{21f}$$

$$\mathscr{L}_2(\chi_2) = \psi_{2y}(\alpha_o \chi_2)_z - \psi_{2z}(\alpha_o \chi_2)_y + \bar{v}_1 \chi_{2y} + \bar{w}_1 \chi_{2z} . \tag{21g}$$

Here the factor k in $\mathscr{D}_1^2$ and $\mathscr{D}_2^2$ is introduced to represent the difference in the values of the eddy diffusion and eddy conduction coefficients in horizontal and vertical directions.

The condensation rates δ_1 and δ_2 in (13) - (20) are calculated by the scheme developed by Kuo and Qian (1981) which is to compute the temperature and humidity T' and q' at time $t + \Delta t$ from the above mentioned equations with δ_1 and δ_2 deleted, and then determine the amount of condensation during the time from t to $t + \Delta t$ when $q_S' = q_1'(t+\Delta t)+q_2'(t+\Delta t)$ is higher than k times the saturation mixing ratio $q_s(T_S')$ where $T_S' = T_1'(t+\Delta t)+T_2'(t+\Delta t)$ and k is taken as slightly less than 1 to take into account the situation where condensation takes place only in a fraction of the area represented by the discrete grid point. Our formula used for calculating δ_j is

$$\delta_j \Delta t = \frac{[q_S' - kq_s(T_S')]}{\left[1 + \frac{kL^2}{C_p R_v T_S'^2} q_s(T_S')\right]} \quad \frac{\Delta q_j}{\Delta q_S'} \tag{22}$$

provided the first factor is positive. When this factor is negative, δ_j is set to zero. When condensation takes place, the final temperature $T_j(t+\Delta t)$ is given by $T_j'(t+\Delta t) + L\delta_j \Delta t/C_p$ and the mixing ratio is given by $q_s(T_j)$, while the liquid water mixing ratio C is calculated by (15) and (20). The detailed scheme of C-calculation is given in Raymond and Kuo (1981).

3. The Initial State

In this preliminary study we have taken the initial perturbation vorticity fields as zero and assigned the following horizontal velocity fields:

$$u_1(x,z) = 2 + 3\cdot 0 \tanh\ (z/z_1) \tag{23a}$$

$$v_1(x,z) = -\frac{1}{4}\frac{x}{x_o} v_m \left\{1 - \tanh[\beta(x - \alpha z - x_o)]\right\} + v_m \exp\left\{-R_1^{-2}\ [(z - z_o)^2 + \gamma_1^2(x - x_o)^2]\right\}; \tag{23b}$$

$$u_2(y,z) = u_m \exp\left\{-R_2^{-2}[\gamma_3^2(z - z_2)^2 + \gamma_2^2(y - y_o)^2]\right\}, \tag{24a}$$

$$v_2(y,z) = u_m \exp\left\{-R_3^{-2}(z - z_o)^2\right\}, \tag{24b}$$

where

$\beta = (48\text{m})^{-1}$, $\alpha = -100$, $R_1 = 2{,}000/\sqrt{2}\text{m}$, $R_2 = 10{,}000/\sqrt{2}\text{m}$,

$R_3 = 2000/\sqrt{2}\text{m}$, $z_o = 4000\text{m}$, $z_1 = 5000\text{m}$, $z_2 = 9{,}000\text{ m}$,

$x_o = 480$ km, $y_o = 1440$ km, $\gamma_1 = 0.03$, $\gamma_2 = 0.02$, $\gamma_3 = 8.0$,

$v_m = 15\text{ m s}^{-1}$, $u_m = 25\text{ m s}^{-1}$.

The eddy diffusion coefficients are currently taken as $\nu_e = 5\text{ m}^2\text{ s}^{-1}$, $\nu = 3\cdot 5\text{ m}^2\text{ s}^{-1}$ and the factor K is taken as 1000 for the dry case and 400 for the wet case. The density stratification factor σ_z is taken as equal to $0.95\times 10^{-4}\text{ m}^{-1}$. Here only a small vertical shear is assigned to u_1 because we wanted to compare the results obtained from the purely two-dimensional system with $\chi_2 = 0$ with the results obtained by Olanski and Ross (1977) which were based on a small shear in u_1 but a relatively large vertical shear has been included in u_2 in the second system. This apparent inconsistency will be removed in our further investigations.

The initial temperature fields $\theta_1(x,z)$ and $\theta_2(y,z)$ are taken as in thermal wind balance with the initial velocity fields v_1 and u_2 and hence they are obtained from the following relations:

$$\frac{1}{\theta o}\frac{\partial\theta_1}{\partial x} = \frac{f}{g}\frac{\partial v_1}{\partial z} , \qquad (25a)$$

$$\frac{1}{\theta o}\frac{\partial\theta_2}{\partial y} = -\frac{f}{g}\frac{\partial u_2}{\partial z} . \qquad (25b)$$

The initial humidity is expressed in terms of the relative humidity γ which is assumed to increase linearly from its surface value of 0.8 to its maximum value of 0.90 at the 2 km level and then decreases linearly with increasing height above this level according to the following formula:

$$\begin{aligned} \gamma(z) &= 0.8 + 0.05\,z \qquad \text{for} \qquad 0 \le z \le 2.0 \text{ km}, \\ &= 0.983333 - 0.04166\,z \qquad \text{for} \qquad 2 \text{ km} \le z , \end{aligned} \qquad (26)$$

where z is in km. The humidity field is taken as unaltered during the first 6 hours and the mixing ratio equations (14), (15) and (19) and (20) are activated at t = 6 hours.

4. The Boundary Conditions

4a. The bottom boundary conditions

- The conditions we impose at the surface level z = 0 are

$$\psi_1 = 0, \quad u_{1z} = 0, \quad \theta_{1z} = 0, \quad q_{1z} = 0; \qquad (27a\text{-}d)$$

$$\psi_2 = 0, \quad v_{2z} = 0, \quad \theta_{2z} = 0, \quad q_{2z} = 0. \qquad (28a\text{-}d)$$

The first two conditions of these sets are equivalent to the vanishing of the vorticities η_1 and η_2 at the surface. The conditions for v_1 and u_2 are that they satisfy the thermal wind relations (25a) and (25b) at the surface.

4b. Boundary Conditions At the Top $z = H$

At the top we assume that both ψ_j, η_{jz}, θ_{jz}, v_{1z} and u_{2z} retain their initial values while $q_j(H)$ is obtained from linear extrapolation from below, and δ_{jz} is taken as zero.

4c. The Side Boundary Conditions

The side boundaries $x = 0$ and $x = D_2$, $y = o$ and $y = D_1$ of the system are taken as open boundaries and the conditions we impose on the flow variables at these boundaries are the following:

$$\frac{\partial \eta_1}{\partial t} + c_{11} \frac{\partial \eta_1}{\partial x} + c_{12} \frac{\partial \eta_1}{\partial z} = 0 \ , \qquad (29a)$$

$$\frac{\partial \chi_1}{\partial x} = 0 \ , \quad \chi_1 = v_1, \ \theta_1, \ q_1, \ c_1 ; \qquad (29b)$$

$$\frac{\partial \eta_2}{\partial t} + c_{21} \frac{\partial \eta_2}{\partial y} + c_{22} \frac{\partial \eta_2}{\partial z} = 0 \ , \qquad (30a)$$

$$\frac{\partial \chi_2}{\partial y} = 0 \ , \quad \chi_2 = u_2, \ \theta_2, \ q_2, \ c_2 \ . \qquad (30b)$$

Here C_{11} and C_{12} are taken as the x-component and the z-component of the phase velocity $\vec{c}_1$ of the vorticity field η_1 while C_{21} and C_{22} are the y-component and the z-component of the phase velocity $\vec{c}_2$ of η_2, respectively. Further, we assume that $\vec{c}_1$ and $\vec{c}_2$ are proportional to $\nabla\eta_1$ and $\nabla\eta_2$, respectively, so that we have

$$c_{11} = - \frac{\eta_{1t}\ \eta_{1x}}{\eta_{1x}^2 + \eta_{1z}^2} \ , \quad c_{12} = - \frac{\eta_{1t}\ \eta_{1z}}{\eta_{1x}^2 + \eta_{1z}^2} \ ; \qquad (31a,b)$$

$$c_{21} = - \frac{\eta_{2t}\ \eta_{2y}}{\eta_{2y}^2 + \eta_{2z}^2} \ , \quad c_{22} = - \frac{\eta_{2t}\ \eta_{2z}}{\eta_{2y}^2 + \eta_{2z}^2} \ . \qquad (32a,b)$$

The values of these phase velocity components at the boundaries are obtained from extrapolations from the interior and the generalized multi-dimensional radiation conditions (29a) and (30a) are applied only when C_{11} and C_{21} are in the outward directions, whereas they are set to zero when the phase velocities are inward. The advantages of this multi-dimensional radiation condition and the ways of its implementation have been demonstrated and described by the authors in another paper (Raymond and Kuo, 1981).

5. Scheme of Integration

The prognostic equations (11) - (20) are integrated at discrete grid points and time defined by $x_i = i\Delta x$, $z_j = j\Delta z$, $y_k = k\Delta y$, $t = n\Delta t$, with i, j, k ranging from 1 to I, J, K, respectively, $\Delta x = 20$ km, $\Delta z = 500$m, $\Delta y = 40$ km, and with I and K both taken as equal to 73 and K = 29 in the first experiment and I = K = 99, J = 37 in the second experiment in order to reduce the errors created by the side and top boundaries. In our approach, the space variations are expressed by finite element representation based on bilinear basis functions while the time integration is by centered difference leap-frog method, with Δt taken as 100 sec.

The stream functions ψ_1 and ψ_2 are obtained by solving the poisson equations (21a) and (21b) together with the boundary conditions for these variables. However, since the mesoscale disturbances under consideration are quasi-hydrostatic in nature and since our use of the large horizontal grid sizes $\Delta x \gg \Delta z$ and $\Delta y \gg \Delta z$ is based on this property, we can take the non-hydrostatic terms ψ_{1xx} and ψ_{2yy} of (21a) and (21b) as small corrections and represent ψ_1 and ψ_2 by series expansions in powers of the small parameter $\varepsilon = \left(\Delta z/_{\Delta x}\right)^2$, where $\Delta z/\Delta x$ can be taken as representative of the ratio between the vertical and the horizontal scales of variation of the disturbance. This scheme is equivalent to the one adopted by Orlanski (1981), which is to represent ψ_1 by the following series

$$\psi_1 = \sum_{j=o}^{m} \psi_j^{(1)} \tag{33}$$

with the different components satisfying the following equations

$$\psi^{(1)}_{ozz} + \sigma_z \psi^{(1)}_{oz} = \rho_o \eta_1 \ , \qquad (34a)$$

$$\psi^{(1)}_{jzz} + \sigma_z \psi^{(1)}_{jz} = \psi^{(1)}_{j-1xx}, \ j \geq 1. \qquad (34b)$$

Here ψ_o represents the hydrostatic component of ψ_1 while the $\psi^{(1)}_j$'s , $j \geq 1$, are the non-hydrostatic contributions. In these forms, the various components $\psi^{(1)}_j$ are solved with respect to z only. The associated boundary conditions are

$$\psi^{(1)}_j = o \ \text{ at } z = o \ \text{ for all } j, \qquad (35a)$$

$$\psi^{(1)}_o = \Psi = \text{initial value of } \psi_1, \ \psi^{(1)}_j = 0, \ j \geq 1 \text{ at } z = H \qquad (35b)$$

Since ε is rather small for the disturbances under consideration, the series (33) converges rapidly and taking $m = 2$ is sufficient for our purposes.

At the lateral boundaries, say at $x = o$ and $x = D_2$, the right hand side of (34b) must be approximated, or with $\psi^{(1)}_j$ evaluated from a given relation such as $w^{(1)}_x = o$. This procedure is utilized in the ψ_1 and ψ_2 calculations.

6. Some Preliminary Results

The system of equations given above have been integrated under four different conditions in order to investigate the influences of the variation of the flow variables in y-direction on the squall line type disturbance, namely, cases 1a and 2a are from the dry and wet versions of the purely two-dimensional ($\chi_2 = 0$) model while cases 1b and 2b are from the dry and wet versions of the coupled multi two-dimensional model. Here we shall present some of these preliminary results and discuss them briefly.

Case 1a and 1b. Each of these two dry cases has been integrated to 24 hours from the initial conditions given by (23a) - (24b) and the thermal wind relations (25a,b) and the vertical velocity $w_1(x,z)$ given by these two different versions at t = 15 hr. are represented in Figures 1 and 2, respectively. From Fig. 1 we see that the 2 units (= 0.15 cm s^{-1}) upward velocity given by the purely two-dimensional xz-plane model reaches to just the z = 5.3 km level and is centered near the x = 700 km mark on the horizontal scale, and the maximum upward velocity in the xz-plane given by the coupled multi-two-dimensional model at $t = 15$ hr. reaches the $z = 8.67$ km level, and this w_1 has two maxima instead of one, namely, one at the 2.5 km level with $w_{max1} = 0.49$ cm s^{-1} and another one at the 7.0 km level, with $w_{max2} = 0.38$ cm s^{-1}. These results show that the variations of the flow variables in y-direction contributes significantly to the flow in the xz-plane even under dry conditions in addition to their influences on the flows in the yz-plane, and we expect that this influence will become larger when condensation process is included.

Case 2a. This moist purely two-dimensional case has been integrated for 45 hours and the results show that the vertical motion w_1 develops rapidly just after $t = 6$ hr. and the maximum upward velocity is reached at $t = 16$ hr., while the intensity of the disturbance decreases gradually afterward. The distributions of the vertical velocity w_1 and the northward velocity v_1 given by this model at $t = 15$ hr. in the xz-plane are illustrated in figures 3 and 4, respectively. From fig. 3 we see that in this moist case with condensation the maximum vertical velocity reached at $t = 15$ hr is 9.25 cm s^{-1} which is about 19.2 times that of the dry case 1a and it also occurs at the 3 km level. From fig. 4 we see that the positive and negative northward velocities are separated by a surface which slopes upward toward west and therefore the disturbance is of the cold front type, and the northward velocity reaches 22.1 m s^{-1} at the 5 km level. Here the vertical circulation in the xz-plane dissipates rapidly after 18 hours but the v_1 field dissipates more slowly as it is nearly in thermal wind balance with the temperature distribution $\theta_1(x,z)$.

Case 2b. This moist case has been integrated from the coupled multi-two-dimensional model up to 24 hours and the results show that for this case the vertical motion w_1 in the xz-plane did not start to increase until $t = 12$ hr. but it continued to increase thereafter for a much longer time until $t = 27$ hr., and its maximum value at $t = 24$ hr. is 27.5 cm s^{-1} which is about 3 times the 9.25 cm s^{-1} value in fig.4. The maximum value of v_1 given by this model at t = 24 hr. is 25.2 m s^{-1} which is only slightly higher than the 22.1 ms^{-1} value given by 2a. The distributions of w_1 and v_1 in the xz-plane for this case at t = 15 hr. and t = 24 hr. are illustrated in Figs. 5 and 6 and Figs. 7 and 8, respectively. From fig. 5 we also see that w_1 has two maxima in the vertical, one at the 2.5 km level and the other at the 7 km level. On comparing fig. 6 with fig. 8 we see that the cold front has moved about 100 km in 9 hours and the southerly jet has also widened somewhat during this time. In addition, we also present the stream function $\psi_2(y,z)$ for t = 24 hr. in fig. 9 to illustrate the pattern of the meridional circulation. This figure shows that this flow is composed of a number of cells on the forward northern edge, with a horizontal scale of about 400 km, and the maximum value of the vertical velocity w_2 of this circulation is 9.32 cm s^{-1}, which is about 1/3 of w_{1max} in fig. 8. These results show that the variations of the variables in y-direction is very important for the development of the vertical circulations in both the xz-plane and in the yz-plane for the squall-line type disturbance. The cellular structure of the circulation in the yz-plane is apparently the result of the instability of the vertical shear of the u_2 profile with regard to overturning or symmetric perturbation in the yz-plane, and the location of these cells indicates that new cells are being generated on the forward edge of the squall-line.

References

Kuo, H. L. and Y. F. Qian, 1981: Influence of Tibetian plateau on Cumulative and Diurnal Changes of Weather and Climate in Summer. Mon. Wea. Rev. 109. In press.

Orlanski, I., 1981: The Quasi-Hydrostatic Approximation. J. Atmos. Sci., 38, 572-582.

Orlanski, I., and B. B. Ross, 1977: The circulation associated with a cold front. Part I: Dry Case. J. Atmos. Sci., 34, 1619-1633.

Raymond, W. H. and H. L. Kuo, 1981: A Radiation Boundary Condition for Multi-Dimensional Flows. Submitting to J. Comp. Phys.

Legend of Figures

Fig. 1. W_1 distribution given by 1a at $t = 15$ hr.

Fig. 2. Same as Fig. 1 but given by 1b at $t = 15$ hr.

Fig. 3. Same as Fig. 1 but given by 2a at $t = 15$ hr.

Fig. 4. U_1 distribution given by 2a at $t = 51$ hr.

Fig. 5. W_1 distribution given by 2b at $t = 15$ hr.

Fig. 6. V_1 distribution given by 2b at $t = 15$ hr.
contour interval 4 m s^{-1}.

Fig. 7. W_1 distribution given by 2b at $t = 24$ hr.
contour interval $\Delta w_1 = 10$ cm s^{-1}.

Fig. 8. U_1 distribution given by 2b at $t = 24$ hr.
contour interval $\Delta u_1 = 5$ m s^{-1}.

Fig. 9. Stream function ψ_2 in yz-plane given by 2b at $t = 24$ hr.
contour interval $= 7.0 \times 10^5$ m^2 s^{-1}.

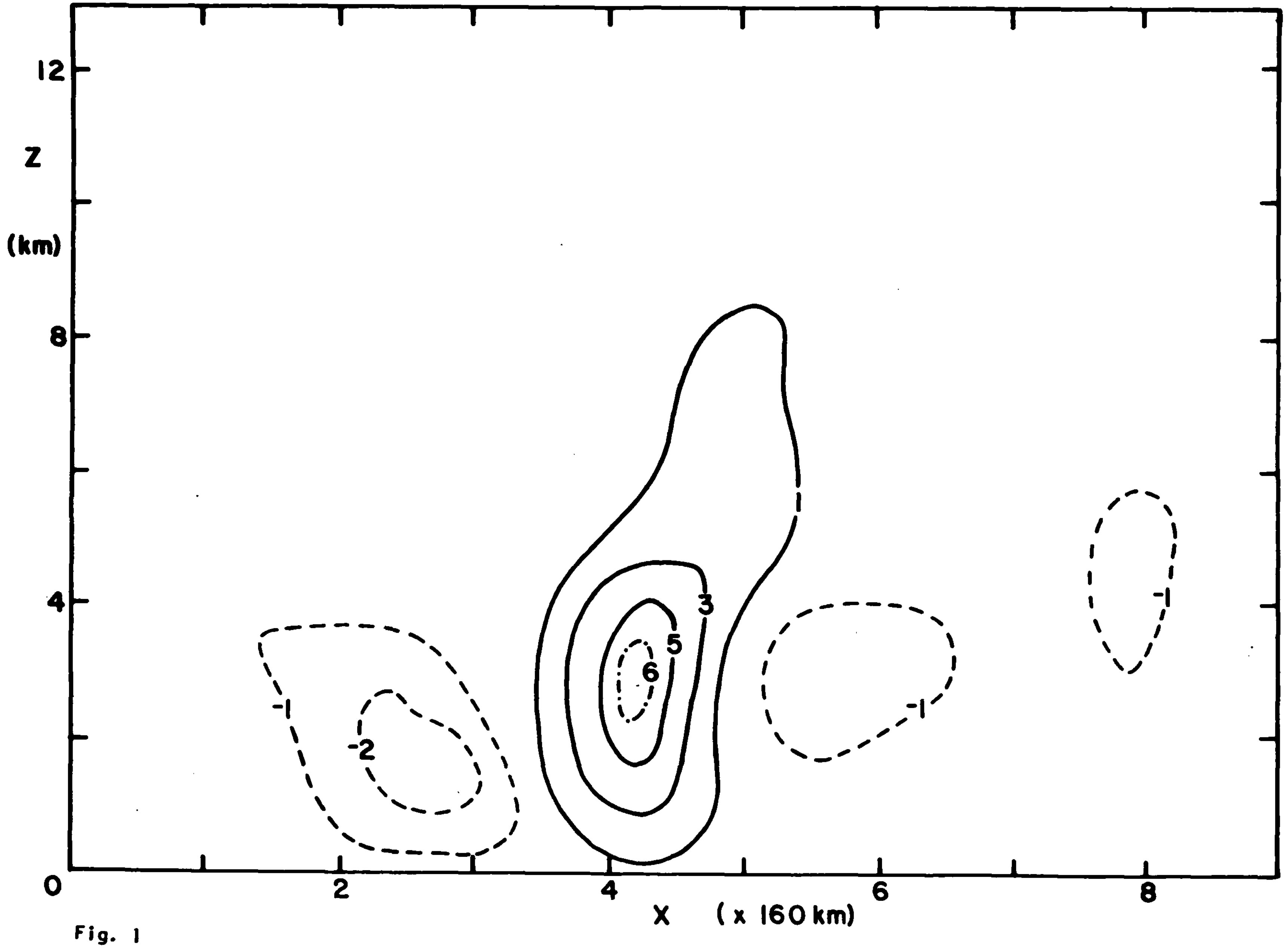

Fig. 1

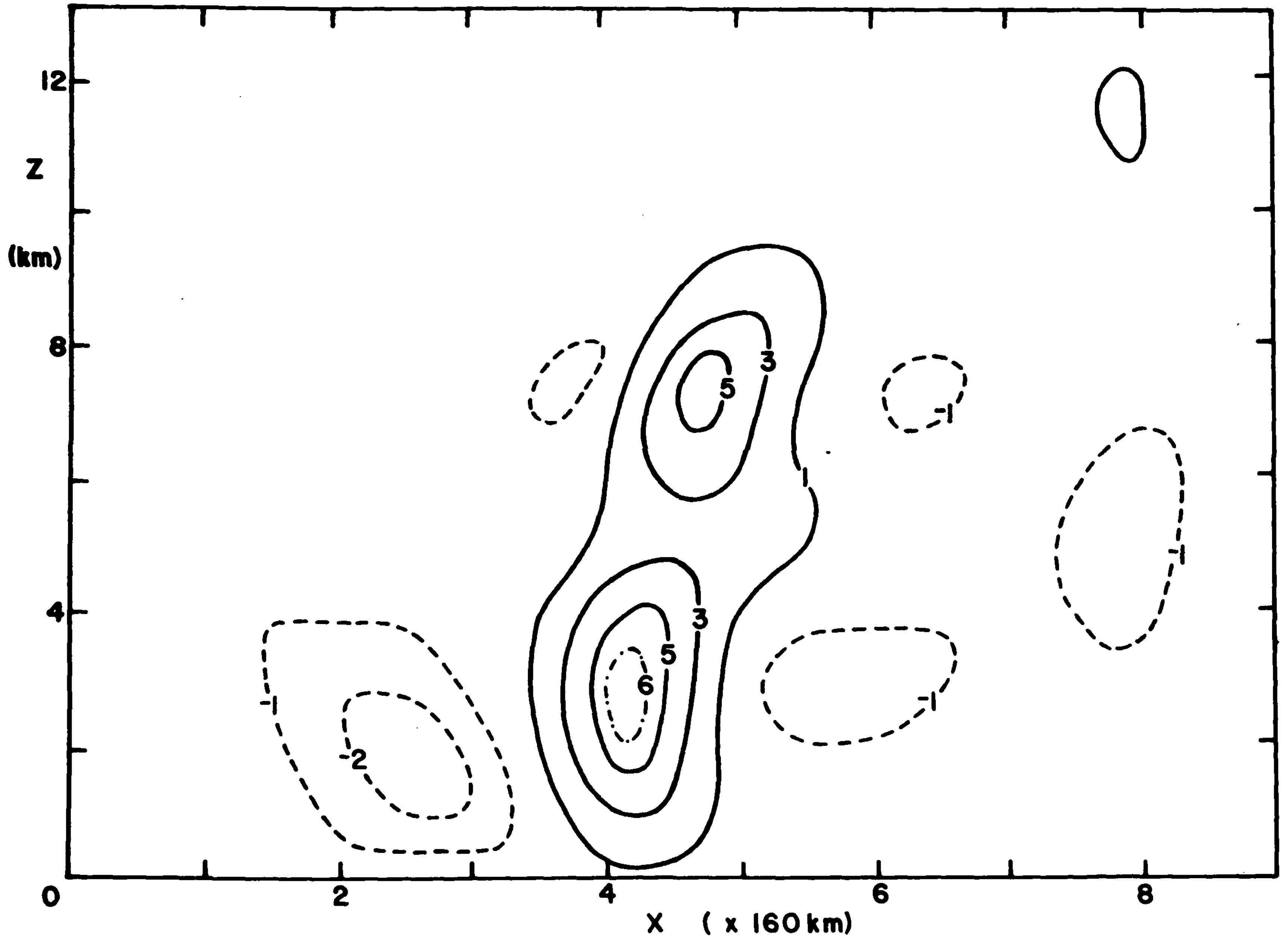

Fig. 2

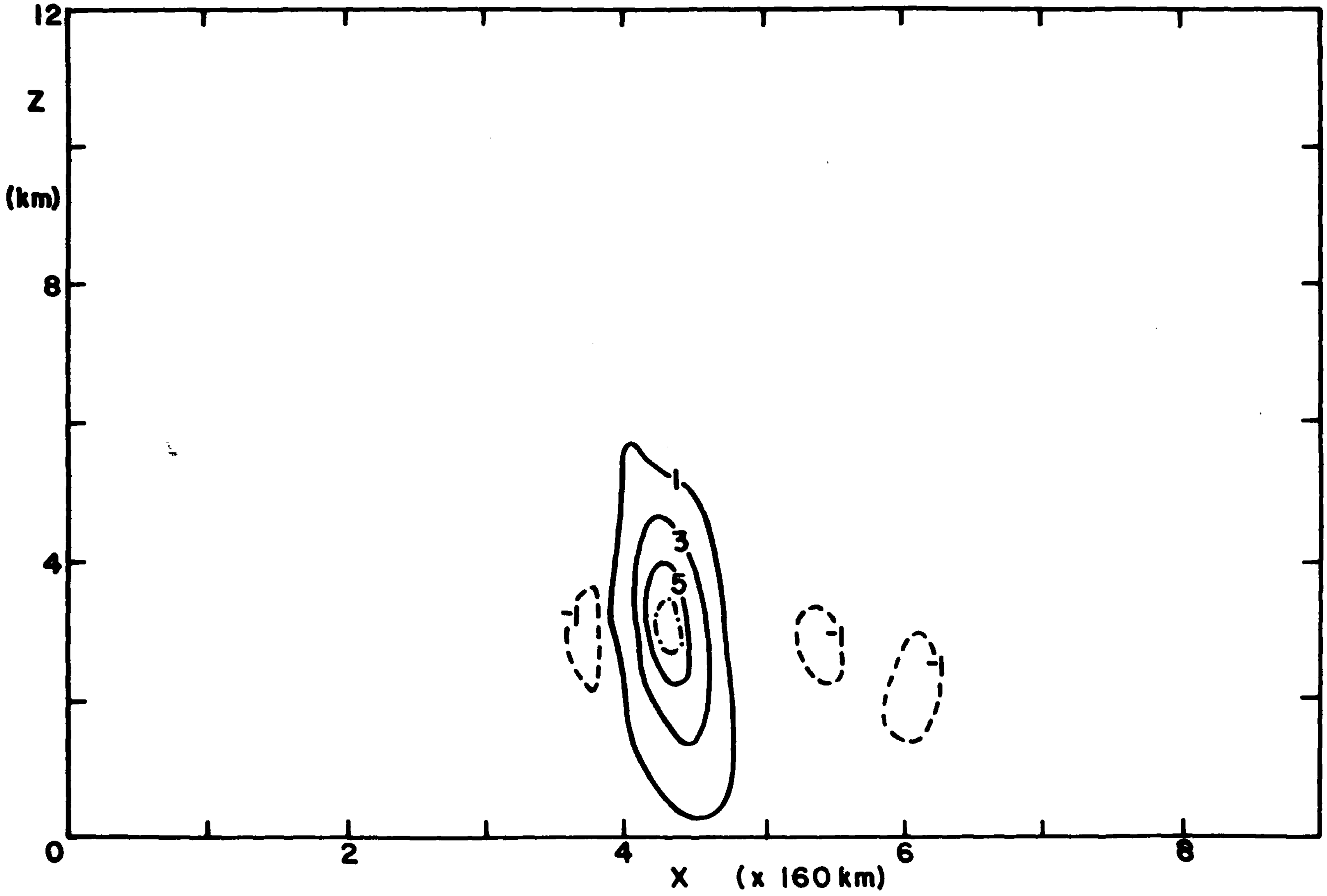

Fig. 3

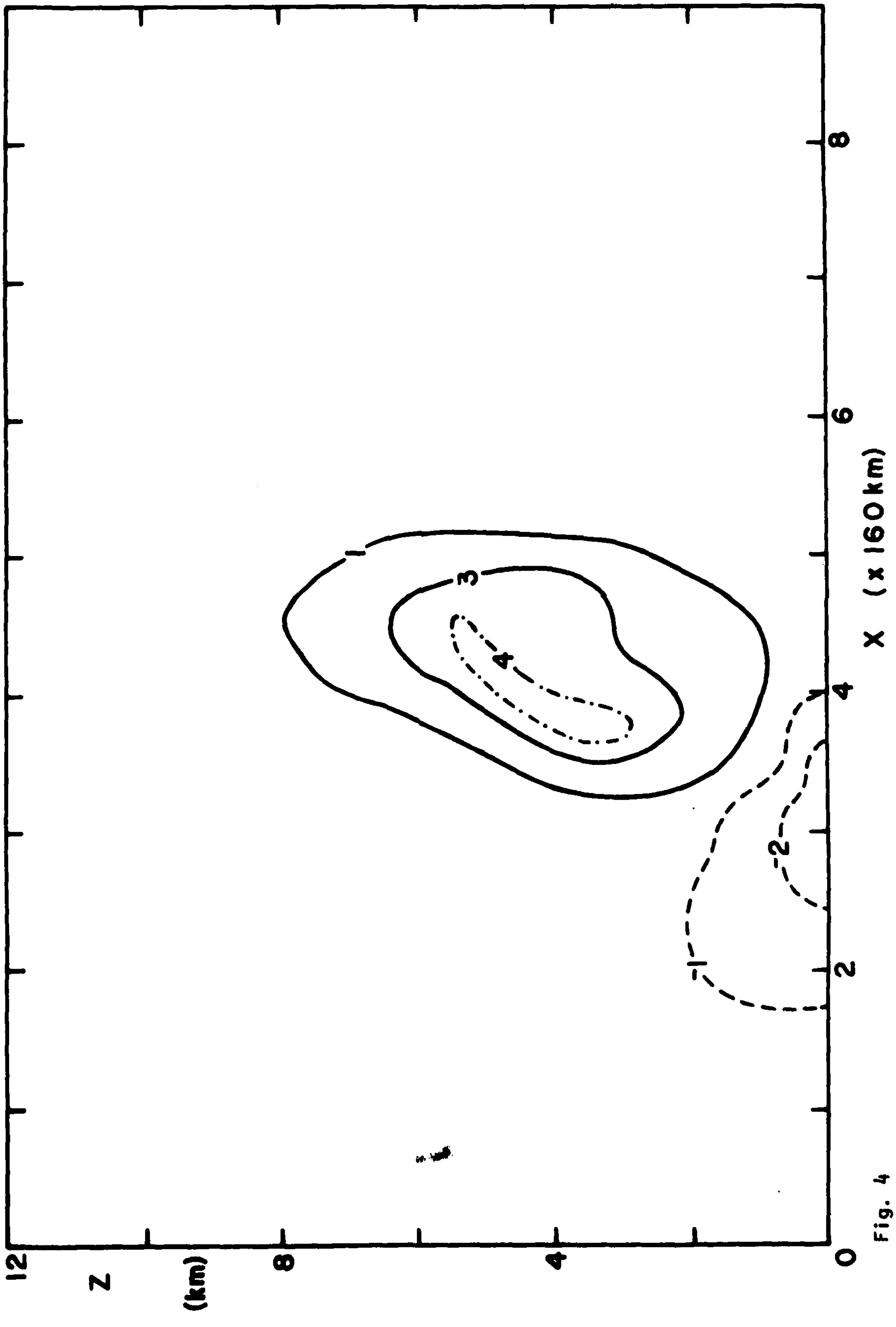

Fig. 4

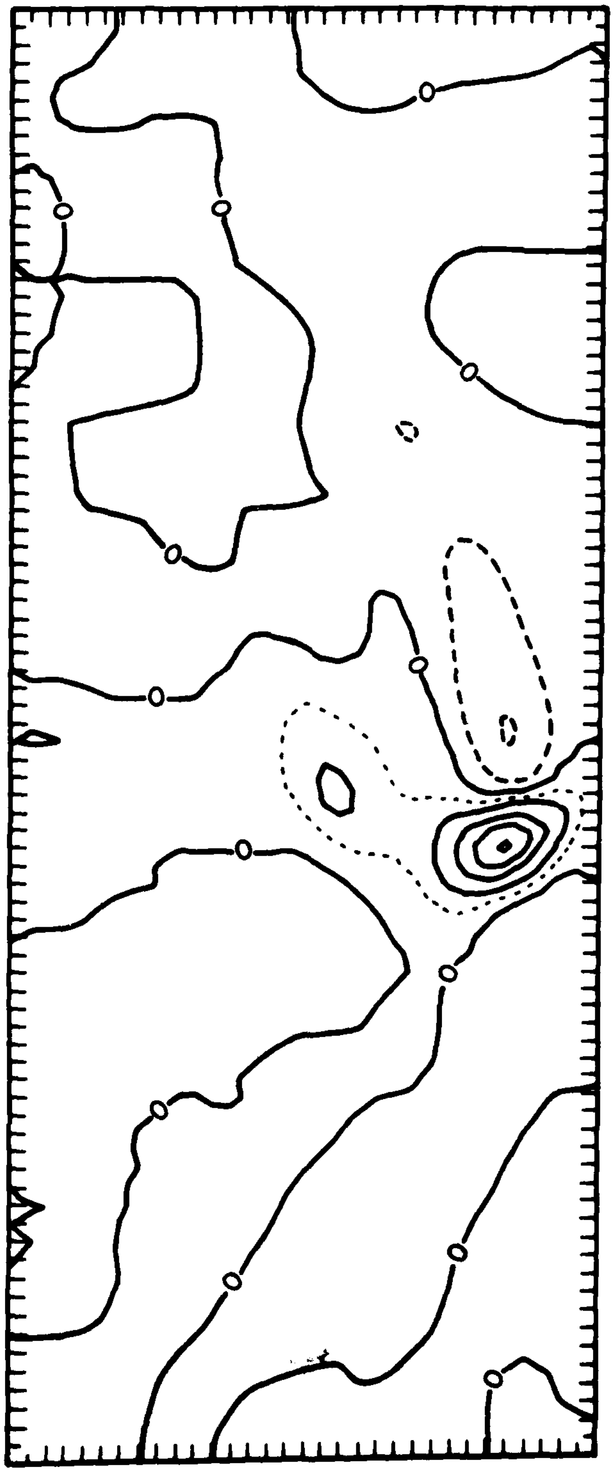

Fig. 5

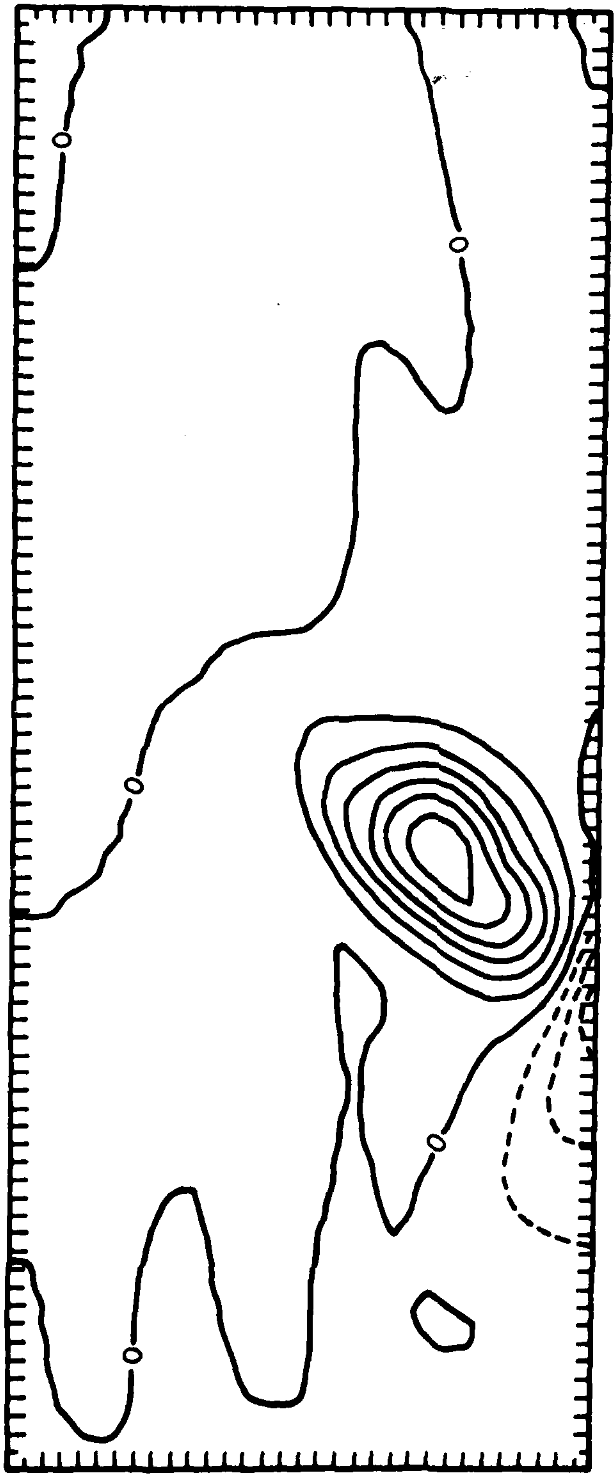

Fig. 6

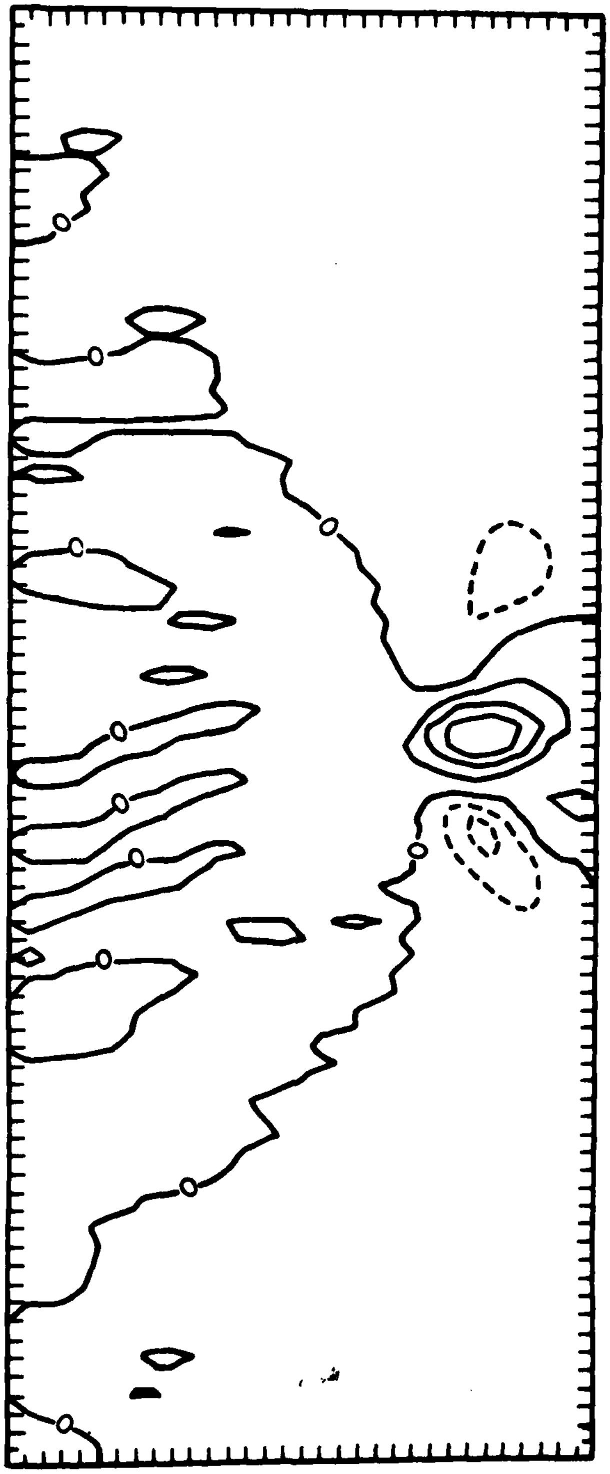

Fig. 7

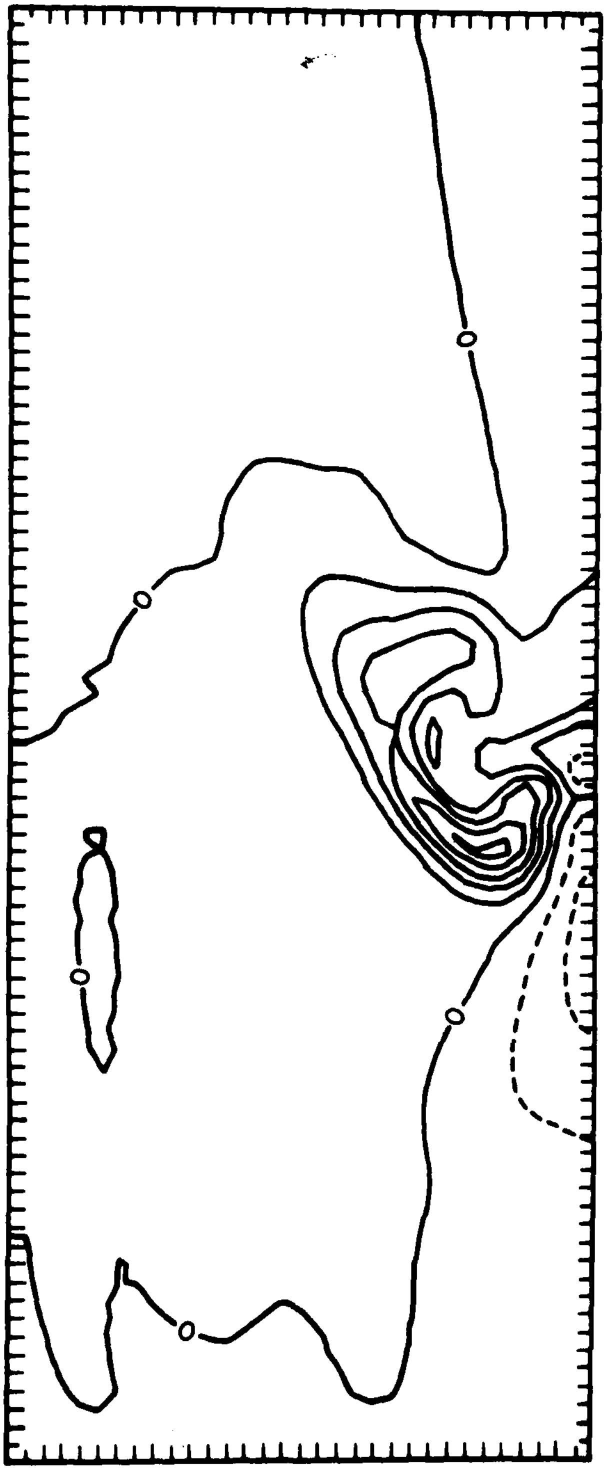

Fig. 8

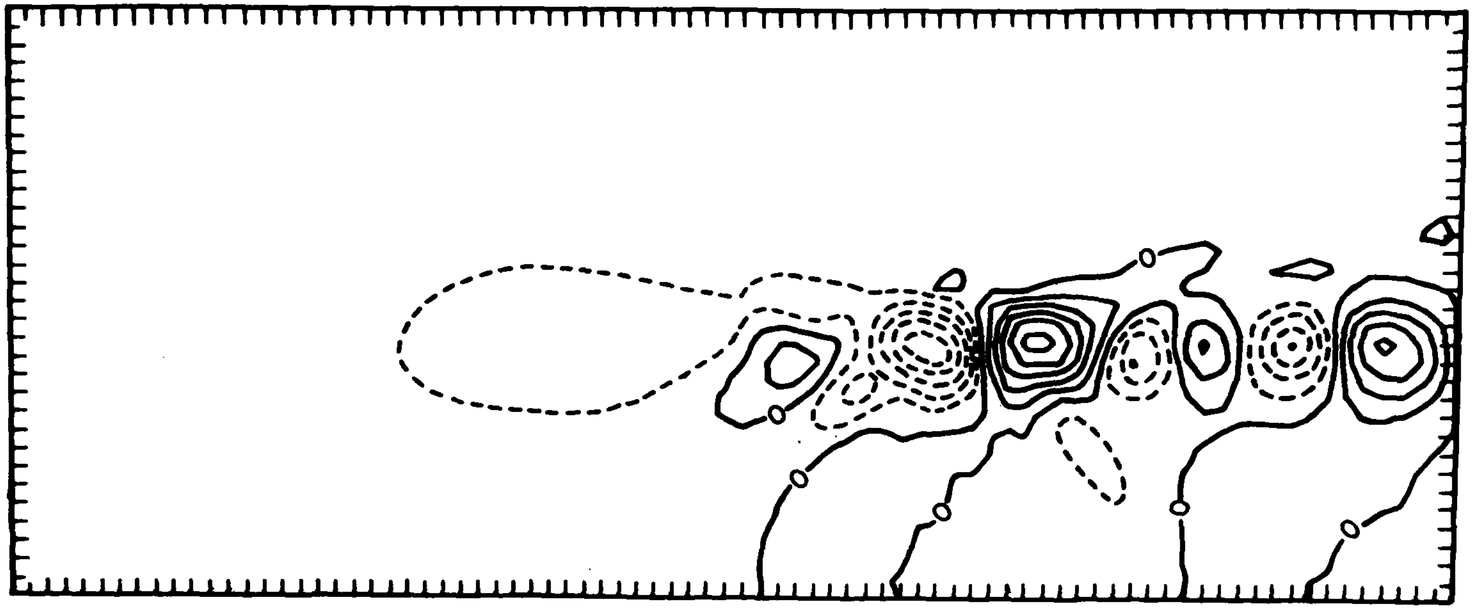

Fig. 9

The Dynamical Structure of Squall-Line Type Thunderstorms

Abstract

The vertical structure of the squall-line type thunderstorm is investigated through the use of a purely two-dimensional model and the flow field is taken as occurring in an unstably stratified atmosphere with a vertically shearing mean wind. A case study of a real squall-line appears to justify this simple approach. The mechanism which leads to the most characteristic upshear slope of these storms is attributed to liquid and solid water loading and attempts are made in this work to verify this hypothesis by integrating the dynamic model from a given initial state to see whether it will evolve to such an arrangement, and also by analysis of the influence of a reasonably chosen but fixed liquid water distribution on the vorticity field in the vicinity of the updraft-downdraft interface. The preliminary results indicate that the proposed mechanism is working.

1. Introduction

This work constitutes a part of our effort to study the dynamics of the squall-line type thunderstorm and it deals only with the usually observed upshear slope of this type of storms. The main thrust of this research is to determine the cause of the upshear slope of the updraft-downdraft couplet in the squall-line type thunderstorms under the influence of the vertically shearing mean flow, and especially to find out whether this arrangement can be attributed to the downward drag or load of the liquid and solid water and evaporative cooling from the falling precipitation, which, according to the reasoning of the senior author, indicates that the upshear arrangement is most efficient energetically for the disturbance in the presence of precipitation because it relieves the loading from the updraft and turns the precipitation drag into an accelerating force for the downdraft, whereas with either vertical or downwind slope these forces tend to destroy the updraft. Further, it is evident a non-vertical slope can not be maintained without a vertically shearing mean wind in the convective storm.

In order to illustrate the nature of the actual squall-line type storms, a brief case study of a squall-line which moved through Chicago area recently is presented in section 2. This is followed by a presentation of the model and the numerical method used to solve it in sections 3 and 4, while section 5 discusses the results that have been obtained from the model. The influence of the liquid water content on the slope is discussed further in section 6 on the basis of the vorticity $\eta = {}^{\partial w}/\partial x - \frac{\partial u}{\partial z}$. Plans for further improvement of the results and future works are discussed briefly in section 7, while a few concluding remarks are added in section 8.

2. Squall line case study

In the late evening of 6 August 1981 a squall line developed and moved across the area of southern Wisconsin and northern Illinois. Although no severe weather was reported in conjunction with this squall line, it did produce high winds and heavy rain. The line formed along a trough line which ran southwest from a surface low in northern Wisconsin to northern Mossouri. The 0000 GMT 7 August 1981 souding from Peoria, IL, is shown in figure 1. Note that the atmosphere is nearly dry adiabatic below 900 mb and very dry above 900 mb except for a few thin moist layers. This sounding shows the atmosphere to be "ripe" for convection, and with a wind shear of about 40/m sec through the depth of the troposphere, we would expect the convection to be organized.

Figure 2 shows the Marsailles, IL radar PPI display for four times during the squall line at approximately 1 h 10 m intervals, starting at 0037 GMT, 7 August 1981. At the earliest time shown, there is a line of broken individual cells of moderate intensity. As the cells increased in intensity, they became elongated and began merging into an unbroken line. By 0148 GMT, portion A of the line is over 25 miles long but less than 10 miles wide, and showed a very uniform reflectivity along its length. The storm reached its peak intensity at approximately 0256 GMT. At this time the line was very long and uniform. The line remained like this for about 40 minutes before breaking up into the weaker cells shown in the last picture at 0405 GMT. In all, portion A of this squall line was visible as long, thin, coherent line of at least moderate intensity for over 2 hours.

Figure 3 shows the hodograph plotted from the wind data of the 0000 GMT Peoria sounding. The speed and direction of portion A, and the orientation of the squall line where determined from the radar pictures and are also shown on this diagram. As can be seen, the winds were somewhat complicated but show a generally unidirectional shear. That is, there is no systematic veering or backing of the winds with height. One also sees that the cells in the squall line move in a direction of approximately the mean wind.

It is common practice in studying squall lines to take a two-dimensional cross-section perpendicular to the squall line. This "slab symmetry" approach assumes that the line is uniform along its length so any motion into or out of this plane is not important. In this case, however, the line is oriented at an angle of nearly 45° to the plane of the mean wind. Thus, a cross-section taken perpendicular to the line would have winds into and out of the plane of the same magnitude as the winds in the plane. Even though this case shows a striking uniformity along the squall line, it is not totally uniform and so this slab symmetry approach does not seem appropriate.

A schematic representation of what appears to be happening in this case is shown in figure 4. In the squall line the updraft and downdraft branches of the circulation are confined to the plane of the mean wind, which is parallel to the direction of motion. The line, however, is oriented at an angle to this plane to form a sort of "snowplow" effect. With this view in mind, it is clear that the plane parallel to the direction of motion is the physically relevant plane of cross-section. We shall use the term two-dimensional in this sense, that is, the circulation is approximately confined in a plane, and therefore refrain from using the term slab symmetry since it does not necessarily imply the same meaning.

Taking the cross-section parallel to the direction of cell motion and defining a new coordinate system with x' parallel to the plane and y' perpendicular to it, one can decompose the winds into the components u' and v' as in figure 5. This shows the v' component to be nearly zero in the mean and, therefore, probably insignificant to the organization of the storm. The u' component shows the storm to be imbedded in an environmental shear of about 3.3×10^{-3} sec^{-1}.

Ludlum (1980) defines a Richardson number for storm circulations as

$$-Ri = \frac{CAPE}{(\Delta U)^2} \tag{2.1}$$

where CAPE is the Convective Available Potential Energy and can be expressed as the positive area of a lifted parcel on a skew-T log-P thermodynamic diagram. The quantity ΔU is the algebraic difference of the horizontal windspeed of the parcel on outflow and inflow, or more simply, the difference between the winds at the storm top and the surface. Using the Peoria sounding, the Richardson number for the parcel lifted from the surface is $-Ri = 1.98$. If the surface to 950 mb average values of temperature and moisture are used we obtain $-Ri = 1.45$. Ludlum (1980) argues that $-Ri \leq 5$ implies organized supercell type convection since then the energy due to shear is comparable to the energy released by latent heat.

The above case exhibits the features which are indicative of the squall-line type supercell which is being investigated in this research effort. It is quasi-steady, maintaining itself with little change for a period of 2 hours. The circulation is two-dimensional in the sense that the environmental wind is basically confined to a plane parallel to the direction of motion. And, the circulation is embedded in an atmosphere of moderate to strong shear, yielding a small Richardson number for the storm.

3. Equations and boundary conditions

Instead of treating it as an initial value problem, here we shall seek the time dependent model and allowing an initial overturning circulation to converge towards a steady state. This is an established method in this type of problem (Roache, 1976). There is also no boundary between the updraft and the down-draft. If a free-slip boundary was present between the updraft and downdraft, it would represent a sheet of infinite vorticity and infinite temperature gradient. Clearly this is not the case in a real thunderstorm and the generation of vorticity at this interface by the finite temperature gradient is a major dynamical feature of the storm. As well as leading to a more realistic model, the removal of the interface simplifies the numerical treatment of the problem.

The basic form of the equations is the same as that given in Seitter (1980) but with density stratification included. They are

$$\frac{\partial \eta}{\partial t} + u\frac{\partial \eta}{\partial x} + w\frac{\partial \eta}{\partial z} + 2w\left(-\eta + u\frac{\partial \rho}{\partial z}\right)\frac{1}{\rho}\frac{\partial \rho}{\partial z} - wu\frac{\partial^2 \rho}{\partial z^2} = -g\rho\frac{1}{T_v}\frac{\partial Tv}{\partial x} + g\frac{\partial M}{\partial x} \tag{3.1}$$

$$\frac{\partial T}{\partial t} + u\frac{\partial T}{\partial x} + w\frac{\partial T}{\partial z} + w\,\Gamma = \frac{\beta(z)L}{C_p}\,G \tag{3.2}$$

$$\frac{\partial q}{\partial t} + u\frac{\partial q}{\partial x} + w\frac{\partial q}{\partial z} = -G \tag{3.3}$$

$$\frac{\partial M}{\partial t} + u\frac{\partial M}{\partial x} + w\frac{\partial M}{\partial z} + v\frac{\partial M}{\partial z} - w\frac{M}{H_o} = \rho G \tag{3.4}$$

where

u, w = horizontal and vertical velocities

η = momentum vorticity

T = temperature

q = water vapor mixing ratio

M = liquid water content

and

$\rho = \rho_s \exp(-z/H_o)$ = density

$T_v = (1 + 0.61q)T$ = virtual temperature

Γ = dry adiabatic lapse rate

L = latent heat of condensation

c_p = specific heat at constant pressure for dry air

$\beta(z) = \exp (z/H_o \cdot R/c_p)$

R = gas constant for dry air

H_o = density scale height

G = liquid water generation term (condensation rate for q)

V = terminal velocity of raindrops

The velocities, u and w, and the vorticity, η, can be written in terms of a streamfunction

$$\rho u = \frac{\partial\psi}{\partial z} \qquad \rho w = -\frac{\partial\psi}{\partial x} \tag{3.5a}$$

$$\eta = \nabla^2\psi \tag{3.5b}$$

where $\nabla^2 = \frac{\partial^2}{\partial x^2} + \frac{\partial^2}{\partial z^2}$. The liquid water generation term is given by

$$G = \begin{cases} 0 & q < q_s,\ M = 0 \\ -E & q < q_s,\ M > 0 \\ -w\dfrac{\partial q_s}{\partial z} & q = q_s \end{cases} \tag{3.6}$$

where E is the evaporation rate, a constant, and q_s is the saturation mixing ratio, determined from the Clausius-Clapeyron equation. The terminal fall-speed of raindrops is taken as a constant with a value of 7 m/sec (Seitter, 1980).

A schematic of the model circulation is shown in figure 6. The inflow characteristics of ψ, T, q, and M are specified for both the updraft inflow, $0 < z < z_{*u}$, and the downdraft inflow, $z_{*d} < z < H$. A condition on η is also needed and is taken as $\frac{\partial\eta}{\partial x} = 0$. On outflow all quantities must satisfy

$$\frac{\partial A}{\partial x} = 0 \qquad A = \psi,\ T,\ q,\ M,\ \text{and}\ \eta \tag{3.7}$$

The value of ψ is fixed on the top and bottom boundary with $\psi_{top} = \psi_{bottom} = \psi_b$. The value of ψ_b is determined such that $\psi = 0$ at the steering level $z = z_*$

for a given inflow shear. The values of T and q are fixed on the top and bottom except when precipitation is present. Then if precipitation has reached the lower boundary, a method similar to Schlesinger (1973) will be employed to allow the boundary to cool and become saturated in response to the presence of rainwater. At the top boundary no liquid water can be present so $M = 0$ there, on the bottom boundary we set $\frac{\partial M}{\partial z} = 0$ to allow rainwater to "fall through" the surface.

With the advective terms written in the flux form no boundary value for the vorticity need be specified on the horizontal boundaries since $w = 0$ on them. However, if the Arakawa Jacobian is used or if a diffusion term of the form $\nu\nabla^2\eta$ is added to (3.1), a value of η on the boundary is needed. Since this model is intended to simulate a nearly inviscid atmosphere, a free-slip condition is appropriate. Roache (1976) has stated that the proper free-slip condition on the vorticity is $\frac{\partial \eta}{\partial z} = 0$ for a finite difference formulation. This form for the boundary condition gives a less viscous effect of the boundaries than the normally used $\eta = 0$ condition, even though the latter is analytically correct.

4. Numerical Method

Equations (3.1) through (3.4) have been nondimensionalized and written in finite difference form, with the velocities u and w written in terms of the streamfunction using (3.5a). All space derivatives were written in centered difference form. Care must be taken to write products of quatities in a finite difference form which is consistent with the form of the advective terms. These four equations and (3.5b) form a complete set in η, T, q, M and ψ. The method of solution consists of starting with an initial field for each of the variables and integrating (3.1) through (3.4) forward in time by an appropriate method. Equation (3.5b) is solved by successive-over-relaxation (SOR) for the new streamfunction field after each time step. This process is continued for the desired time or until a steady state is reached.

Three methods of time integration have been used in the development and testing of this model. A forward-in-time centered-in-space method was used initially as a simple method to test the model. This method was soon abandoned, however, since it required a large diffusion term for linear stability. The inviscid equations were also integrated using the two-step Lax-Wendroff method (Richtmeyer, 1962). Although this method has been used with success in meteorological problems (Houghten, et. al., 1966), Lilly (1965) warns that it can lead to severe inaccuracies in certain types of subsonic fluid flow problems. This seemed to be the case with the current problem, as it was not possible to eliminate small, but accumulating, errors which are inherent in the Lax-Wendroff method and which eventually destroyed the accuracy of the integration. This method was ultimately abandoned, although some important results were obtained while it was being used (see Section 6). The very accurate method of Adams and Bashforth (Lilly, 1965) has been used with success both in integrating the truly inviscid equations and in solving the equations with an added viscosity term.

The Adams-Bashforth method can be written by considering the equation for some quantity A,

$$\frac{\partial A}{\partial t} = f \tag{4.1}$$

where f is a function of the other variables and their derivatives. We let $f^{(n)}$ be the value of f evaluated by using the values of the variables at time $t = n\Delta t$. Then the value of A at time $t = (n + 1)\,\Delta t$ is given by

$$A^{(n+1)} = A^{(n)} + \Delta t\left[\frac{3}{2}\,f^{(n)} - \frac{1}{2}\,f^{(n-1)}\right] \tag{4.2}$$

This method is slightly amplifying and, therefore, not stable in the strict sense of the word. The amplification factor is small, however, and does not pose a problem as long as the integration is not extended for too long.

The method can be stabilized by adding a viscous term of the form $\nu\nabla^2 A$. This is included by writing (4.2) as (Roache, 1976)

$$A^{(n+1)} = A^{(n)} + \Delta t\left[\frac{3}{2} f^{(n)} - \frac{1}{2} f^{(n-1)}\right] + \Delta t\nu\nabla^2 A^{(n)} \tag{4.3}$$

Note that this is not equivalent to including a viscous term in f.

Since the Adams-Bashforth method can be used successfully on the fully inviscid equations, the viscosity which is added can be made whatever size is appropriate for the problem. This is preferable to the Lax-Wendroff method that has a built in numerical diffusion which selectively damps small wavelengths.

The current version of the model has 21 grid points in the horizontal and 11 in the vertical. The grid spacing is even and taken as 1 km in both the horizontal and vertical, giving a domain of 20 km by 10 km. The choice of a 10 km depth for the domain was somewhat arbitrary. Excluding the overshooting top of the updraft, observed thunderstorm circulations extend from the surface to a height of 10 km to 14 km (Chisholm 1973, Ludlum, 1980). The depth of the model makes very little difference when the density is held constant, but in simulations in which the variation of density with height is included, the depth of the model may have to be adjusted.

5. Numerical results

As discussed in Moncrieff (1978), the case of a neutrally stratified, incompressible atmosphere with $M = 0$ is quite simple. In this case the vorticity equation reduces to

$$\frac{d}{dt}\eta = 0 \tag{5.1}$$

So, vorticity is conserved along a streamline. If we consider an environment of linear shear, then on inflow the vorticity is given by

$$\eta = \frac{\partial u}{\partial z} = \text{constant} \tag{5.2}$$

since $\frac{\partial w}{\partial z} = 0$ on inflow. Thus, the vorticity will be constant throughout the circulation, and the steering level height will be at $z_{*u} = z_{*d} = H/2$. Moncrieff shows that in this case the interface between the updraft and downdraft will be vertical. This situation is shown in figure 7.

Figure 7 was determined by performing a relaxation on a vorticity field which had constant vorticity everywhere except on the dividing streamline. On the dividing stream line the vorticity was adjusted to yield a streamfunction value equal to that on the upper and lower boundaries. The nondimensional streamfunction values marked on the figure correspond to a linear shear 2×10^{-3} $\sec^{-1}$.

The inviscid, incompressible form of the vorticity equation was integrated forward in time as a test of the numerical model for this case. The flux form of finite difference was used for the advective derivatives and the Adams-Bashforth method was used for the time integration. The vorticity field of figure 7 was used as the initial condition. After 20 minutes of simulated time the change in this field was less than the initial errors in it. This demonstrates that the flux form for the advective derivatives was able to accurately maintain this known solution to the equations, and that the slight amplification inherent in the Adams-Bashforth method was too small to pose a problem.

This is the only case in which the Adams-Bashforth method was used without diffusion term as described in the preceding section. Without diffusion of some sort, all disturbances must be advected out of the domain and very small temperature variations can lead to large variations in the vorticity.

b. Dry, convectively unstable case

In order to further test the model by reproducing Moncrieff's results of downshear orientation, the equations were reduced to the case of a dry, convectively unstable, incompressible atmosphere. Then the equations are

$$\frac{\partial \eta}{\partial t} + u \frac{\partial \eta}{\partial x} + w \frac{\partial \eta}{\partial z} = - g\rho \frac{1}{T} \frac{\partial T}{\partial x} \tag{5.3}$$

$$\frac{\partial T}{\partial t} + u \frac{\partial T}{\partial x} + w \frac{\partial T}{\partial z} + w \Gamma = 0 \tag{5.4}$$

Since Γ is taken as a constant equal to 6.5 °C/Km, a constant environmental lapse rate which is greater than this yields a convectively unstable atmosphere and exactly models the equations used by Moncrieff (1978).

Moncrieff defines a type of Richardson number given by

$$R = \frac{\text{CAPE}}{\frac{1}{2} u_o^2} \tag{5.5}$$

where u_o is the horizontal velocity at the surface in the updraft inflow. This is related to, but larger in absolute value than, the Richardson number defined by (2.1). Figures 8(a) and 8(b) show the results of Moncrieff's calculations for $R = \frac{1}{2}$ using his analytical and numerical models, respectively. The method of solution for the analytical result has been described previously (Seitter, 1980). The numerical solution was found using a method similar to the current model except that a staggered grid Lax-Wendroff integration scheme was used.

The current model was run with an unstable lapse rate which gave $R = \frac{1}{2}$. The initial condition was given by the circulation shown in figure 7 and an initially adiabatic atmosphere. Diffusion was included in the model with the value of the eddy viscosity set at 450 m^2/sec. While this is about an order of magnitude larger than the value in cumulus clouds (Tag, 1979), it does not seem to be too large in light of the measurements of kinetic energy dissapation in thunderstorms (Frisch and Strauch, 1975), and is much smaller than the numerical diffusion included in many previous models (Schlesinger, 1973). It was found necessary to include a diffusion term because without it the generation of negative vorticity at the updraft-downdraft interface by the temperature gradient there formed a countercirculation at the interface.

The results of this model after 21 minutes simulated time are shown in figure 9. There are some distinct differences between this result and those of Moncrieff. The most notable difference being that the current result shows the circulation sloping less steeply downshear. Also, the steering level heights for both the updraft and downdraft are located at $z = H/2$. It is felt that both of these differences are a result of the inclusion of diffusion in the model. The diffusion of temperature weakened the gradients and hence the production of vorticity, and the diffusion of vorticity "slowed down" the flow. It is felt that this circulation represents the case in which the instability is great enough to overcome the viscosity of the fluid but not great enough to accelerate the flow appreciably and thus raise the steering level height z_{*u}. Thus, the modeled flow represents a flow which would correspond more directly to a smaller value of R and, hence, would slope downshear less steeply (Moncrieff, 1978).

Although the Lax-Wendroff method has a built in diffusion, it is felt that this did not alter Moncrieff's results in the way it did in the current model because the diffusion in the Lax-Wendroff method is highly selective toward short wavelengths. This allows the method to prohibit the development of a counter-circulation at the interface while allowing the rest of the flow to remain virtually inviscid. This kind of selective damping can be incorporated into the present model for a quantity A by replacing $\nu\nabla^2 A$ with $K|\nabla^2 A|\nabla^2 A$ (Cullen, 1976). It is felt at this time, however, that the simpler diffusion term is preferable.

The shape of the interface in the results of the current model more closely resembles the shape of Moncrieff's analytical result (figure 8(a)) than does Moncrieff's numerical result (figure 8(b)). This is felt to be significant and is a favorable indication as to the accuracy of the current model.

Although no details are given in either his paper (Moncrieff, 1978) or his thesis (Moncrieff, 1970), it is assumed that Moncrieff must have used a much smaller grid spacing than the current model to overcome the problems associated with the Lax-Wendroff method. The author has found that a very small grid spacing does improve the Lax-Wendroff method, but the cost of increasing the number of grid points substantially, as well as the inherent high cost of this method (over twice as time consuming per time step as the Adams-Bashforth method), make the Adams-Bashforth method more desirable.

6. The mechanism for upshear slope in the light of the vorticity η

It has long been recognized that the upshear slope of the updraft in thunderstorms is beneficial to their maintenance from a thermodynamic point of view. However, no adequate theory has been proposed which explains how the updraft is able to oppose the shear in which it is imbedded. The framework of the present model allows a dynamical theory for the upshear slope based on vorticity arguments.

Consider the incompressible vorticity equation

$$\frac{\partial \eta}{\partial t} + u\frac{\partial \eta}{\partial x} + w\frac{\partial \eta}{\partial z} = - g\rho \frac{1}{T_{vo}} \frac{\partial Tv}{\partial x} + g\frac{\partial M}{\partial x} \qquad (6.1)$$

Now, consider a flow pattern as shown in figure 10(a), with the updraft-downdraft interface vertical. Let the updraft have a positive temperature excess and the downdraft have a negative temperature excess, and let there be precipitation in the updraft. In figure 10(a), the precipitation is shown in the lowest half of the updraft because it would tend to be heaviest there and thus have the most dynamical effect in this region. As can be seen from (6.1), it is the horizontal derivatives of the temperature and liquid water which are important. The circulation is driven by the temperature distribution, which produces negative vorticity generation ($\frac{\partial \eta}{\partial t} < 0$) along the interface and hence maintains the strong shear across the interface. Positive vorticity is generated ($\frac{\partial \eta}{\partial t} > 0$) in both the updraft and downdraft branches away from the interface, and this also acts to maintain the circulation. Now, consider the effect of the liquid water. On the downdraft side of the precipitation column ($\frac{\partial M}{\partial x} > 0$), positive vorticity will be generated, and on the updraft side of the column ($\frac{\partial M}{\partial x} < 0$), negative vorticity will be generated. There are two ways that the updraft branch can respond to this negative vorticity generation: 1) the shear can be reduced to make the shear vorticity less positive; 2) the streamlines can curve less sharply as they enter the updraft to reduce the curvature vorticity. Both of these responses probably take place, and both tend to cause the streamlines to enter the updraft at a more upshear, rather than vertical, angle. A similar argument leads to the streamlines in the lower downdraft becoming more sharply curved as they exit the downdraft, which is consistent with the entire circulation sloping upshear.

Consider now the situation shown in figure 10(b), which more closely resembles the flow in a real thunderstorm. This diagram is very similar to the schematic given by Ludlum (1963). The flow is still driven by the positive and negative temperature excesses. (Now, the downdraft is shown to have a negative temperature excess only in the region where rain water can cause evaporation cooling, as is the case in real storms.) The streamlines show less curvature in the updraft inflow where negative vorticity is being generated and more curvature in the downdraft outflow where positive vorticity is being generated. This vorticity generation by the liquid water term does not operate unchecked, of course, it opposes the effects of the environmental shear which tends to tilt the circulation downshear until a balance is established.

A simple means of testing this hypothesis is to integrate (6.1) with fixed distributions of temperature and liquid water. This was done while the model was in the Lax-Wendroff phase of development.

Figure 11 shows the results of the integration after 14 minutes of simulated time, starting with an initially vertical interface. In this run, a temperature excess of $\pm.25$ °C was fixed in the updraft and downdraft regions respectively and no liquid water was present. The vertical shear on inflow was 2×10^{-3} $\sec^{-1}$. This should, in a simple way, model the results of Moncrieff (which were modeled more accurately in the previous section). Consistent with Moncrieff's results, the flow is oriented downshear. The flow is not steady at this time but is intensifying and beginning to form a closed counter circulation between the updraft and the downdraft (note the closure of the 96 streamline). The steering level heights z_{*u} and z_{*d} reflect the fact that the flow is being accelerated so the depth of the inflow must be greater than the depth of the outflow.

Using the same temperature distribution and the same initial circulation, a region of liquid water equalling 2g m^{-3} was added to the lower half of the updraft. Figure 12 shows the results of this run after the same period of time. Now, the vorticity generation due to the precipitation has had a marked effect on the flow. While the circulation does not have a truly upshear orientation, the trend is definitely to oppose the effects of the shear. The flow is also weakened in the updraft branch by the effects of the water loading and the reverse circulation is inhibited except in the region above the precipitation.

The previous results seem to strongly support the hypothesis that the upshear orientation of the updraft-downdraft couplet is both caused and maintained by the effects of the liquid water which is produced in the storm. This would explain why strong thunderstorms which have the ability to produce large amounts of rain exhibit an upshear slope and small showers and cumulus clouds slope downshear.

7. Discussion and future plans

The preceding sections have shown the current model to reproduce the results of Moncrieff fairly well. The differences can be explained by simple reasoning based on the differences between the current model and Moncrieff's model. The simple model has also given insight into the mechanism which causes the upshear slope of the updraft. These results give one confidence in the model and show that the proposed extension of the model to include precipitation is warranted. This section will discuss the improvements which have been made in the model and plans for its use in further investigations, which will include the addition of the equations for water vapor and liquid water to the system of equations (3.1)-(3.4) and their integration to a steady state. To improve the resolution, the grid spacing will be cut in half. It is felt that a grid spacing of no greater than 500 m in both the vertical and horizontal is necessary since large variations can occur over the distance of a kilometer or two, especially in the interface region.

It is hoped that the compressibility of the atmosphere does not significantly affect the qualitative behavior of the storm structure. This, however, will have to be tested. The equations were proposed in the anelastic form and have been finite differenced in this form for the model. Most of the runs are expected to be carried out with the density held constant due to the relative ease in interpreting the results. A few compressible simulations can then serve to show that the qualitative structure remains the same as well as providing a more realistic picture of the storm's structure.

The moisture equations have been finite differenced and tested to prepare for their inclusion into the model. Figure 13 shows the thermodynamic diagram which is produced by the equations for an incompressible atmosphere. The dry adiabatic lapse rate is taken as a constant with the value 9.76 °C/km. The moist adiabats are reproduced quite accurately in the model. Diagrams like figure 13 will allow an environmental profile to be plotted and the corresponding Ri to be calculated for each case using (2.1) and

$$\mathrm{CAPE} = g\int_0^H (\ln \theta_a - \ln \theta_e)dz \tag{7.1}$$

where θ_a is the potential temperature of a parcel ascending from the surface and θ_e is the environmental potential temperature.

The situation of characterizing a flow by its value of Ri will not be as easy now compared to Moncrieff's model in which constant lapse rates for both the ascending parcel and the environment were assumed. Now, two very different profiles could be constructed to yield the same numerical value of Ri. Differing profiles of environmental moisture can also be expected to influence the resulting flow. While it is not possible in this more complicated model to completely characterize a flow by the value of Ri, this still is expected to be an important parameter and will be continued to be used as a measure of the relative importance of bouyancy and shear.

The first case to be run with the complete model will be for an environment with a linear temperature profile having a surface temperature of 300 K and a temperature of 237 K at 10 km ($\gamma = 6.3$ °C/km). The moisture will be given by 90% relative humidity throughout the atmosphere, and the environmental shear will be constant with a value of 4×10^{-3} sec^{-1} ($\Delta U = 40$ m/sec). This gives a value of -Ri = 1.0. This situation is not meant to model an observed thunderstorm environment, but is a simple environment with the appropriate Ri. This case should provide a definitive test of the upshear slope hypothesis and provide a benchmark for comparisons of runs with different environmental conditions.

8. Conclusions

After a good deal of effort, a numerical method which is reliable and accurate has been developed and the basic results of earlier work (Moncrieff, 1978) have been reproduced. With the approval of a grant of time on the NCAR system, it is now possible to improve and complete the model. The full model is currently being readied, and after testing, it will be run on its first case. This case should confirm the hypothesis which was presented here; that the effects of the liquid water act to produce and maintain the upshear slope of the updraft which is thermodynamically necessary for the maintenance of the squall-line type thunderstorm.

References

Chisholm, A. J., 1973: Radar case studies and airflow models. Meteor. Mono., 14, No. 36, 1-36.

Cullen, M. J. P., 1976: On the use of artificial smoothing in Galerkin and finite difference solutions of the primitive equations. Quart. J. Roy. Meteor. Soc., 102, 77-93.

Frisch, A. S., and R. G. Strauch, 1976: Doppler radar measurements of turbulent kinetic energy dissipation rates in a north-eastern Colorado convective system. J. Appl. Meteor., 15, 1012-1017.

Houghten, D., A. Kasahara and W. Washington, 1966: Long-term integration of the barotropic equations by the Lax-Wendroff method. Mon. Wea. Rev., 93, 141-150.

Lilly, D. K., 1965: On the computational stability of numerical solutions of time-dependent non-linear geophysical fluid dynamics problems. Mon. Wea. Rev., 93, 11-26.

Ludlum, F. H., 1963: Severe local storms: A review. Meteor. Mono., 5, No. 27, 1-30.

_____________, 1980: Clouds, and storms. Penn. State Univ. Press, University Park, Penna., 404 pp.

Moncrieff, M. W., 1970: Cumulonimbus convection in shear. Ph.D. Thesis, Dept. Meteor., Imperial College, London.

_______________, 1978: The dynamical structure of two-dimensional steady convection in constant vertical shear. Quart. J. Roy. Meteor. Soc., 102, 77-93.

Richtmeyer, R. D., 1962: A survey of difference methods for non-steady fluid dynamics. NCAR Tech. Note 63-2, 25 pp.

Roache, P. J., 1976: Computational Fluid Dynamics. Hermose Publ, Alburquerque, N.M., 446 pp.

Seitter, K. L., 1980: The dynamical structure of squall-line type thunderstorms. Research Prospectus, Dept. of Geophys. Sci., Univ. of Chicago, Chicago.

Tag, P. M., 1979: A comparison of several forms of eddy viscosity parameterization in a two-dimensional cloud model. J. Appl. Meteor., 18, 1429-1441.

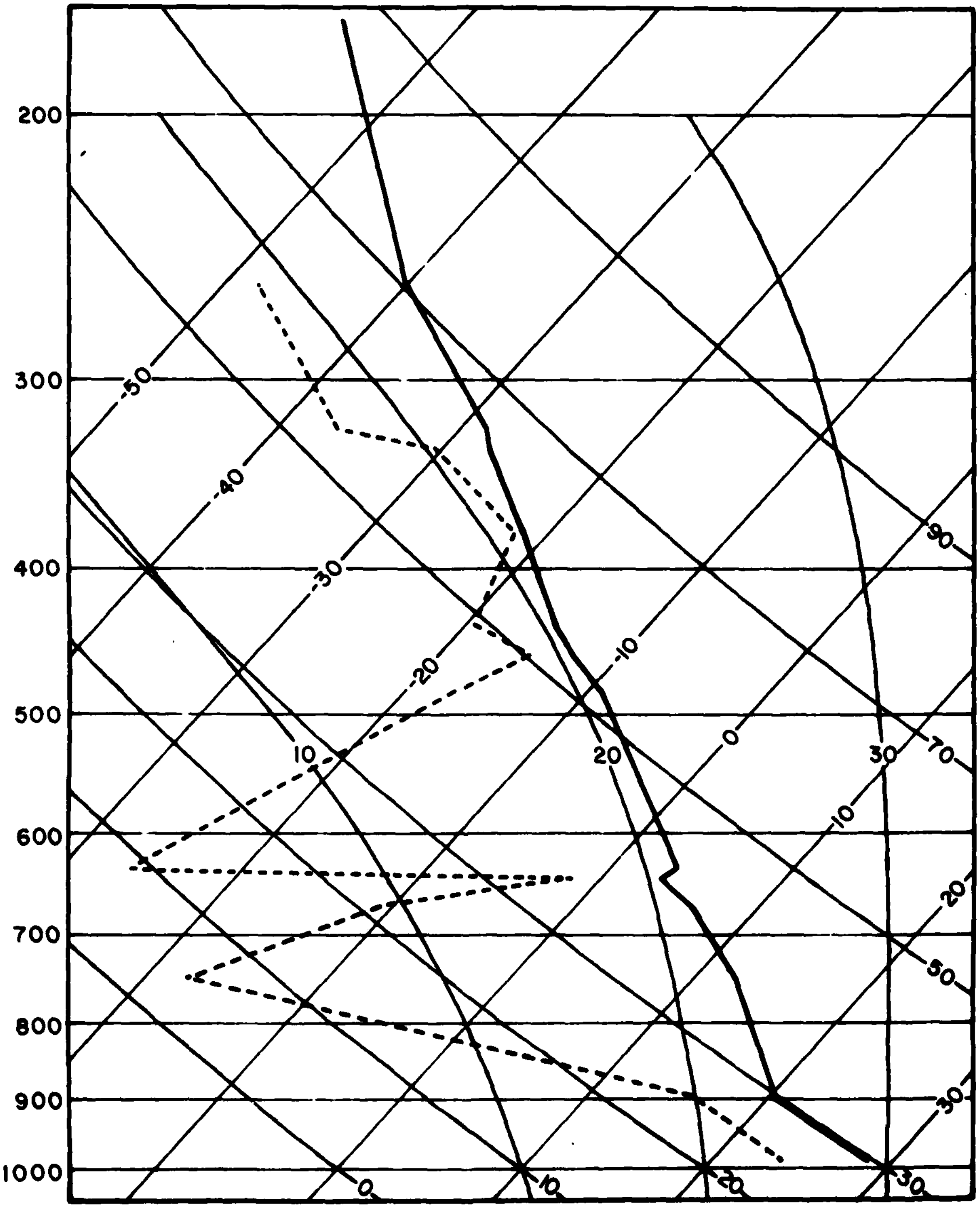

Figure 1. The 0000 GMT, 7 August 1981 sounding for Peoria, IL. The temperature is given by the heavy solid line and the dewpoint temperature by the broken line.

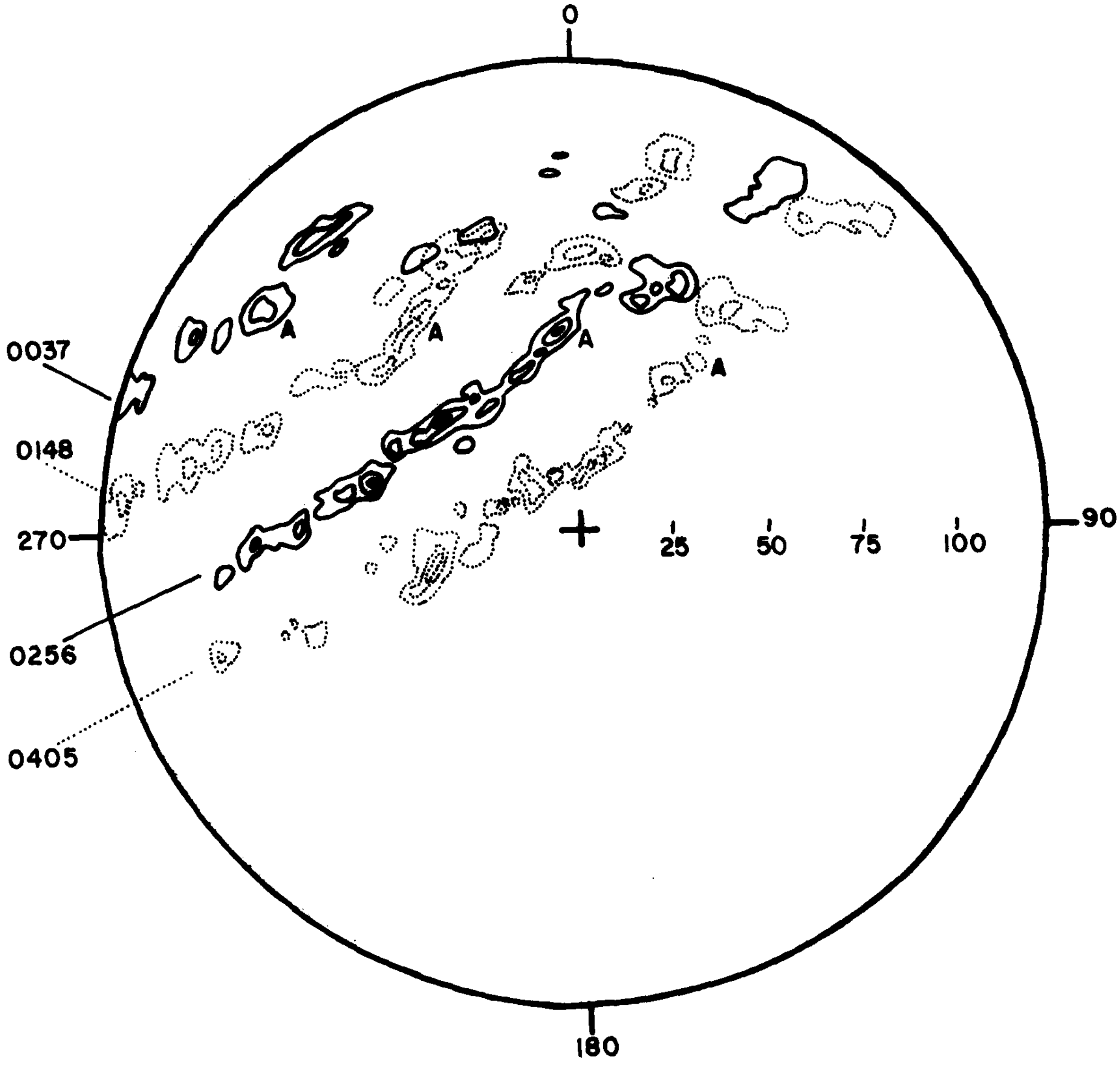

Figure 2. Marsailles, IL. Radar PPI display for four times during squall line passage. The reflectivity contours are for levels 1, 3 and 5, and alternate between solid and dotted for sequental times. Times indicated are in GMT on 7 August 1981. The distance scale along the 90° radius is in miles.

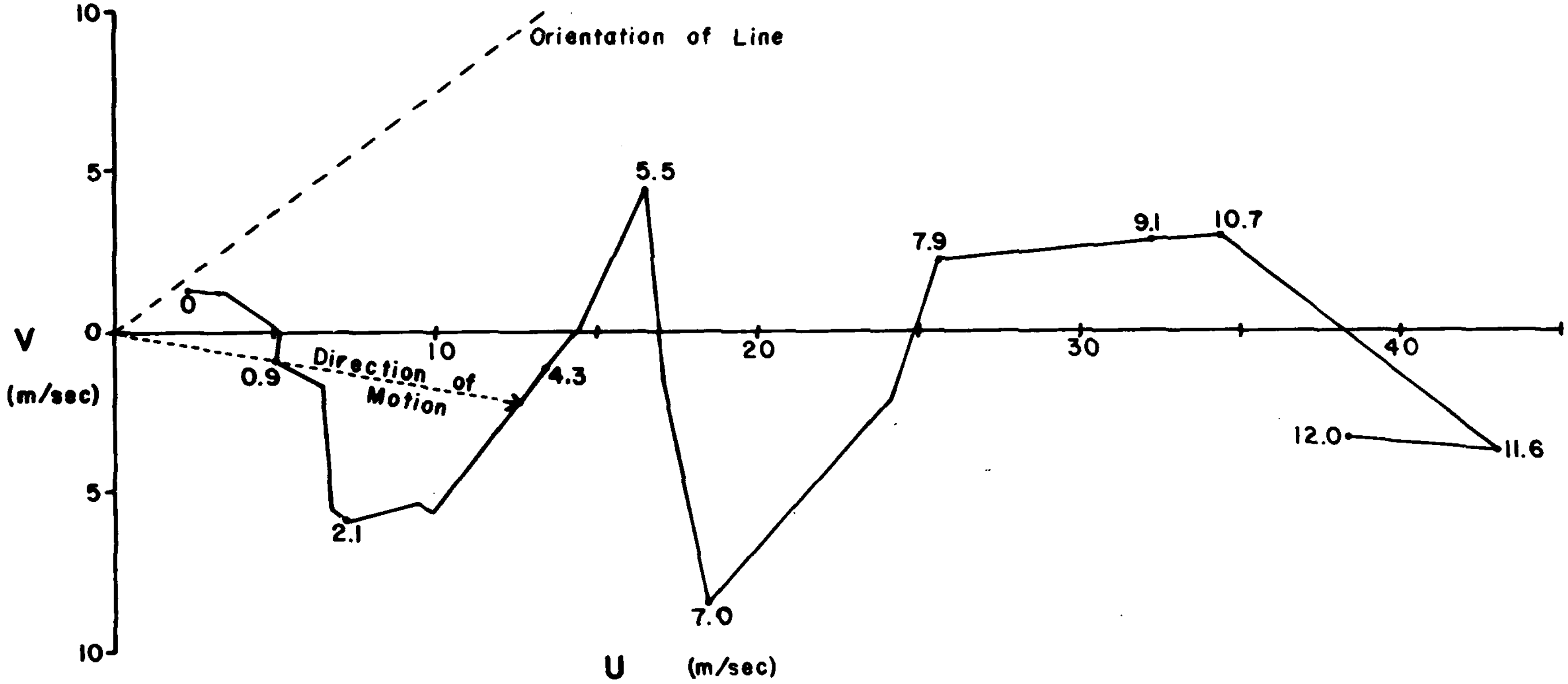

Figure 3. *Hodograph of the environmental wind taken from the* 0000 GMT Peoria sounding. The height of points on the hodograph is shown in kilometers, and the direction of cell motion and orientation of the line is also shown.

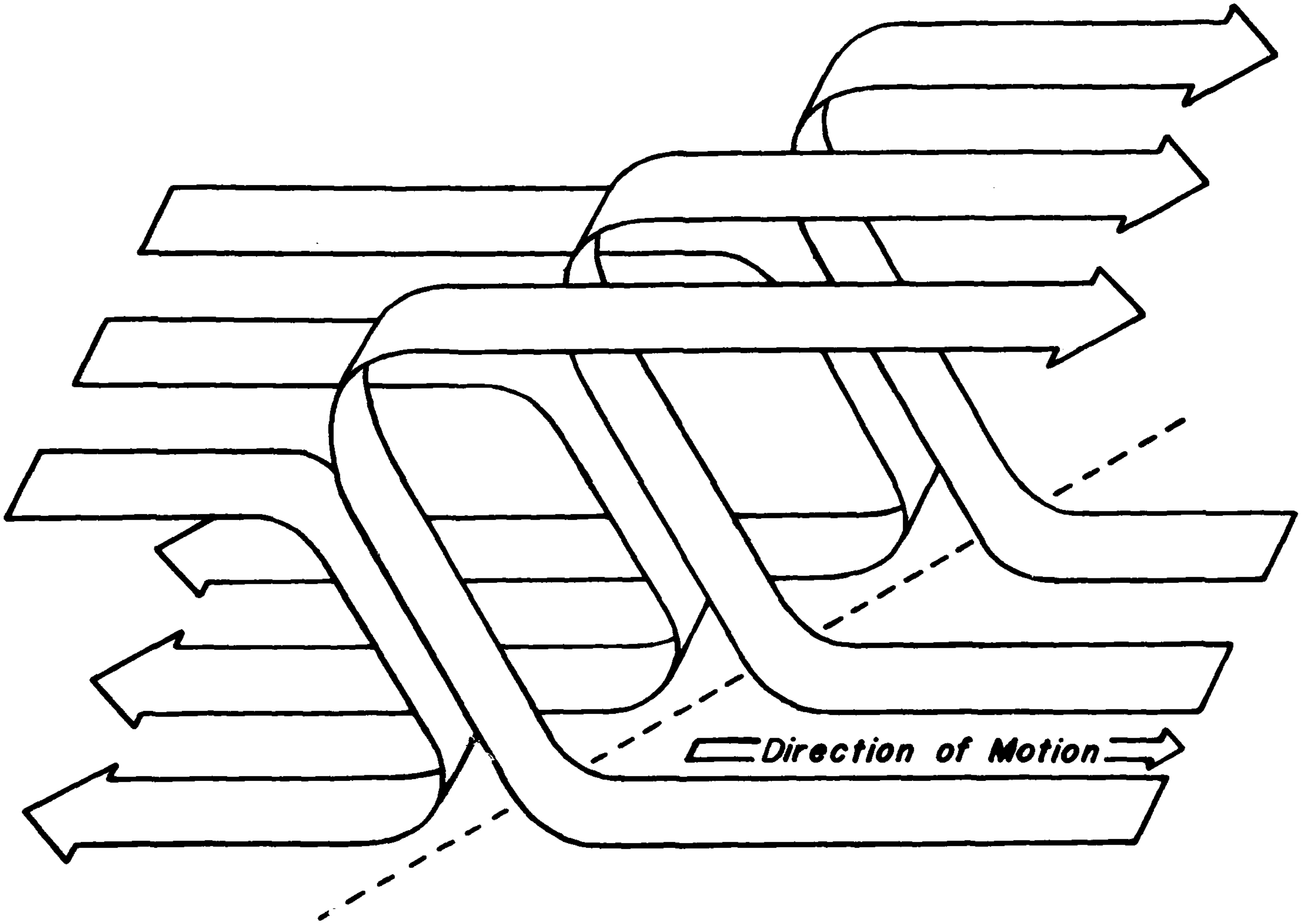

Figure 4. Schematic of the circulation in the squall line. The motion is restricted to the plane parallel to the direction of motion, but the line is oriented at a sharp angle to this plane.

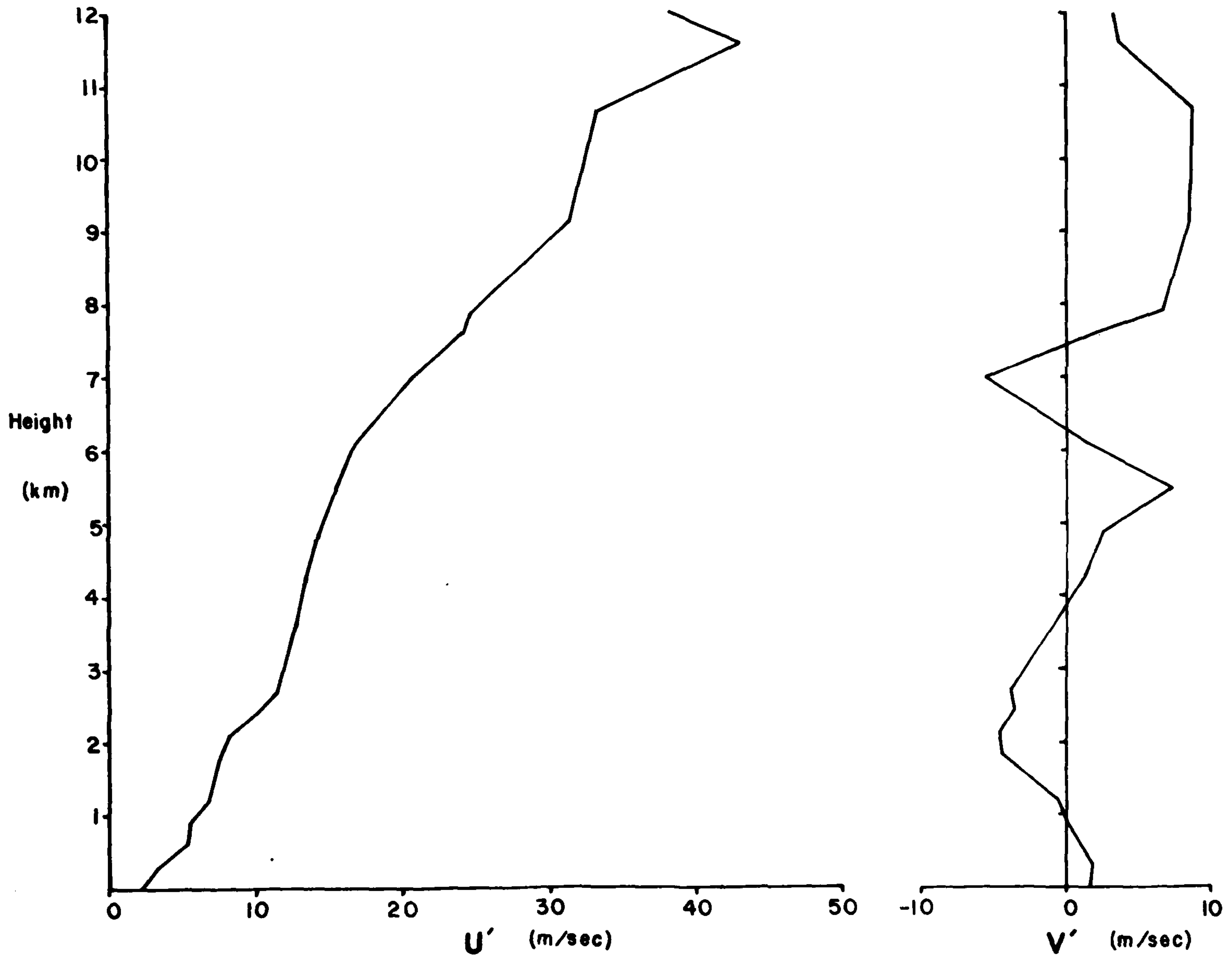

Figure 5. Wind components parallel to (u') and perpendicular to (v') the direction of motion.

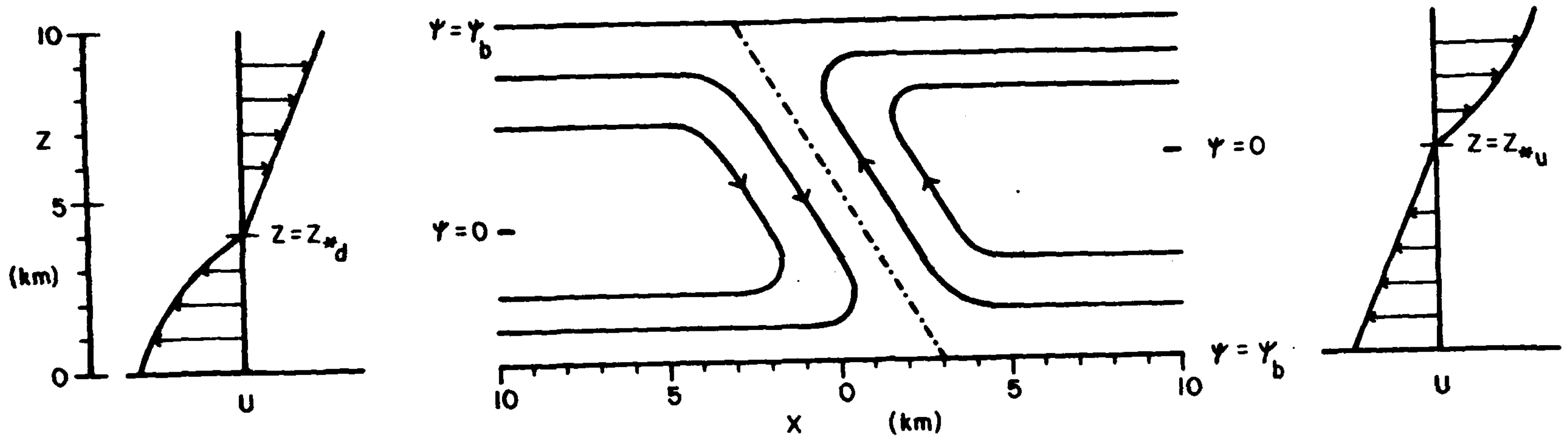

Figure 6. Schematic of the model showing the domain and the velocity profiles at the lateral boundaries for the updraft and downdraft circulations.

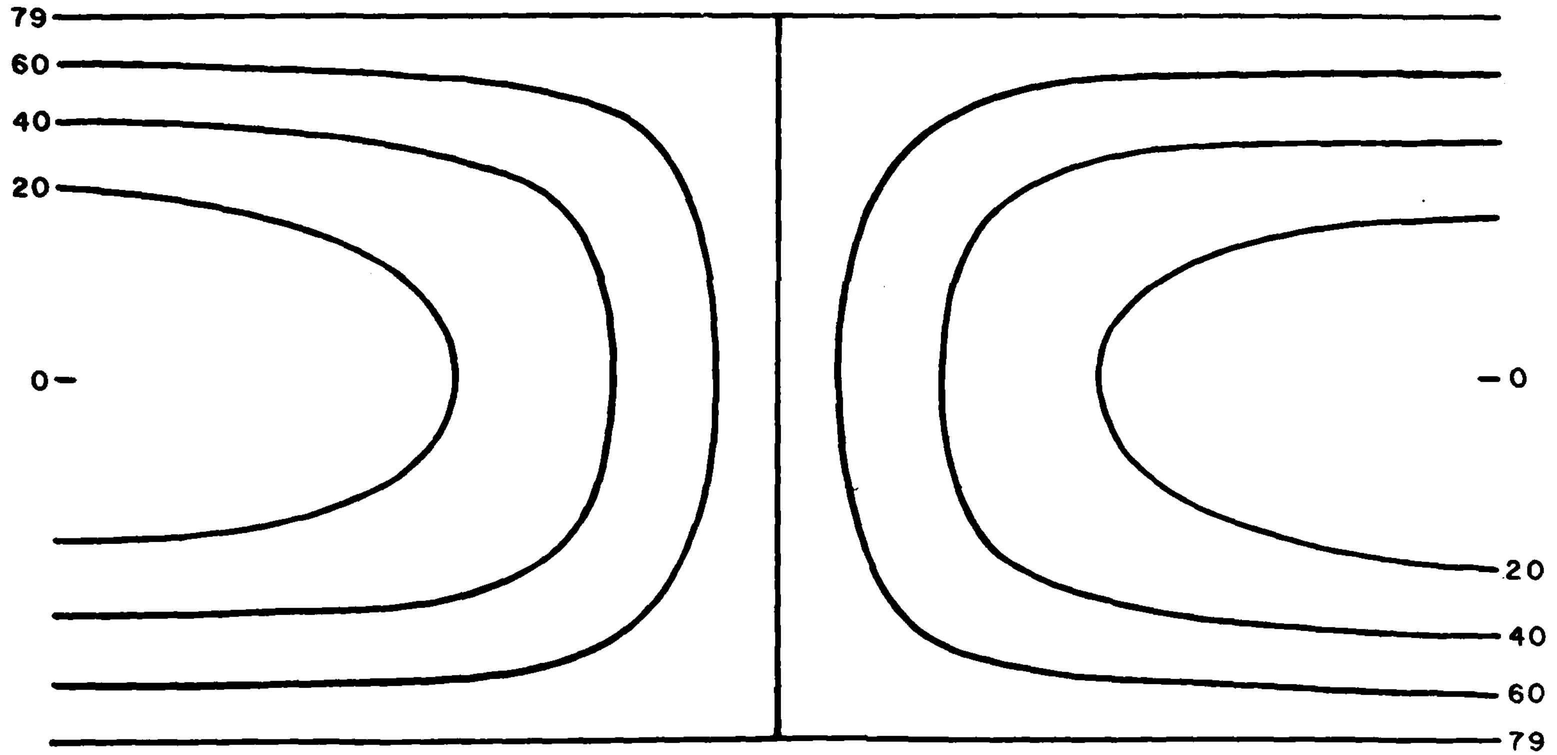

Figure 7. Solution for a neutral, incompressible atmosphere. The value of the nondimensional streamfunction is marked at the inflow point of the streamlines and corresponds to a shear of 2×10^{-2} sec^{-1}.

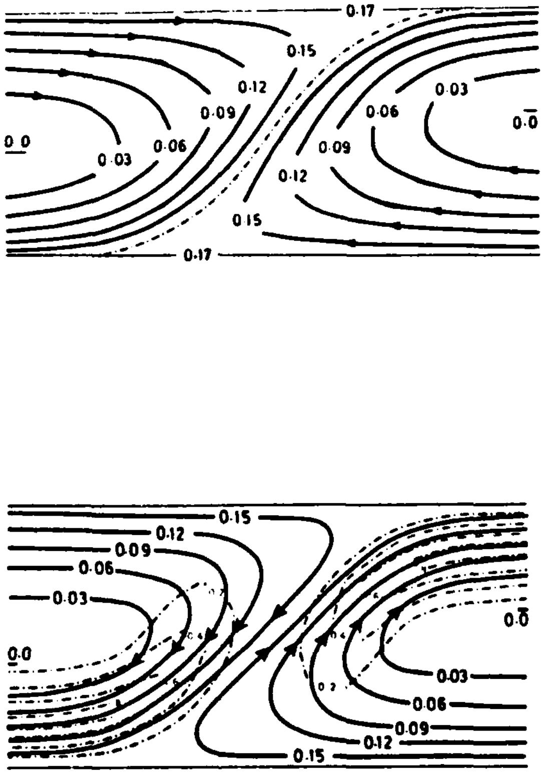

Figure 8. Results of Moncrieff's analytical (a) and numerical (b) model for R = ½. Chain line in (a) represents the interface between the updraft and downdraft. In (b) the nondimensional temperature excess is shown as a chain line (From Moncrieff, 1978.)

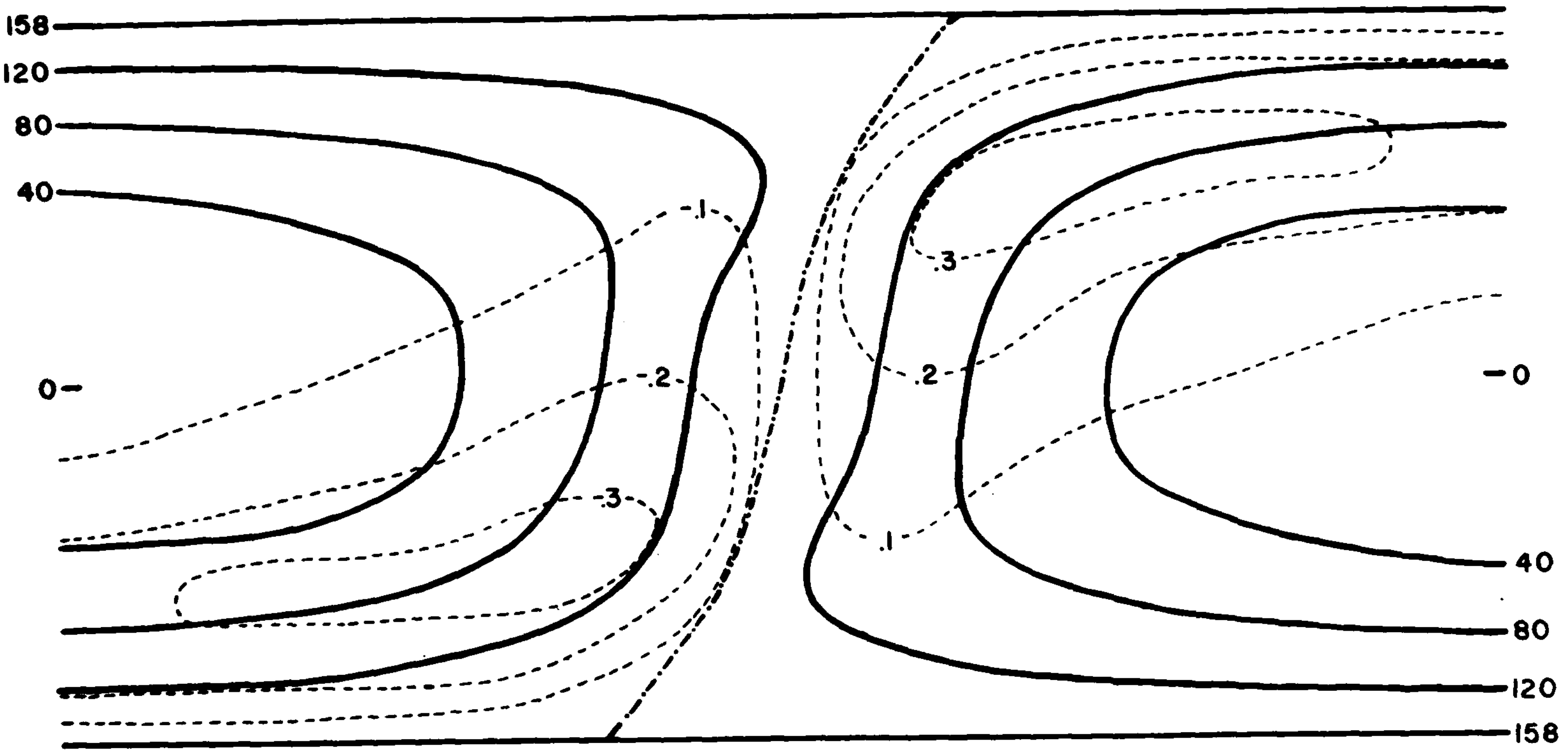

Figure 9. The results of the current model for R = ½. Dashed lines represent isotherms of temperature excess in °C. The interface between the updraft and downdraft is shown as a chain line.

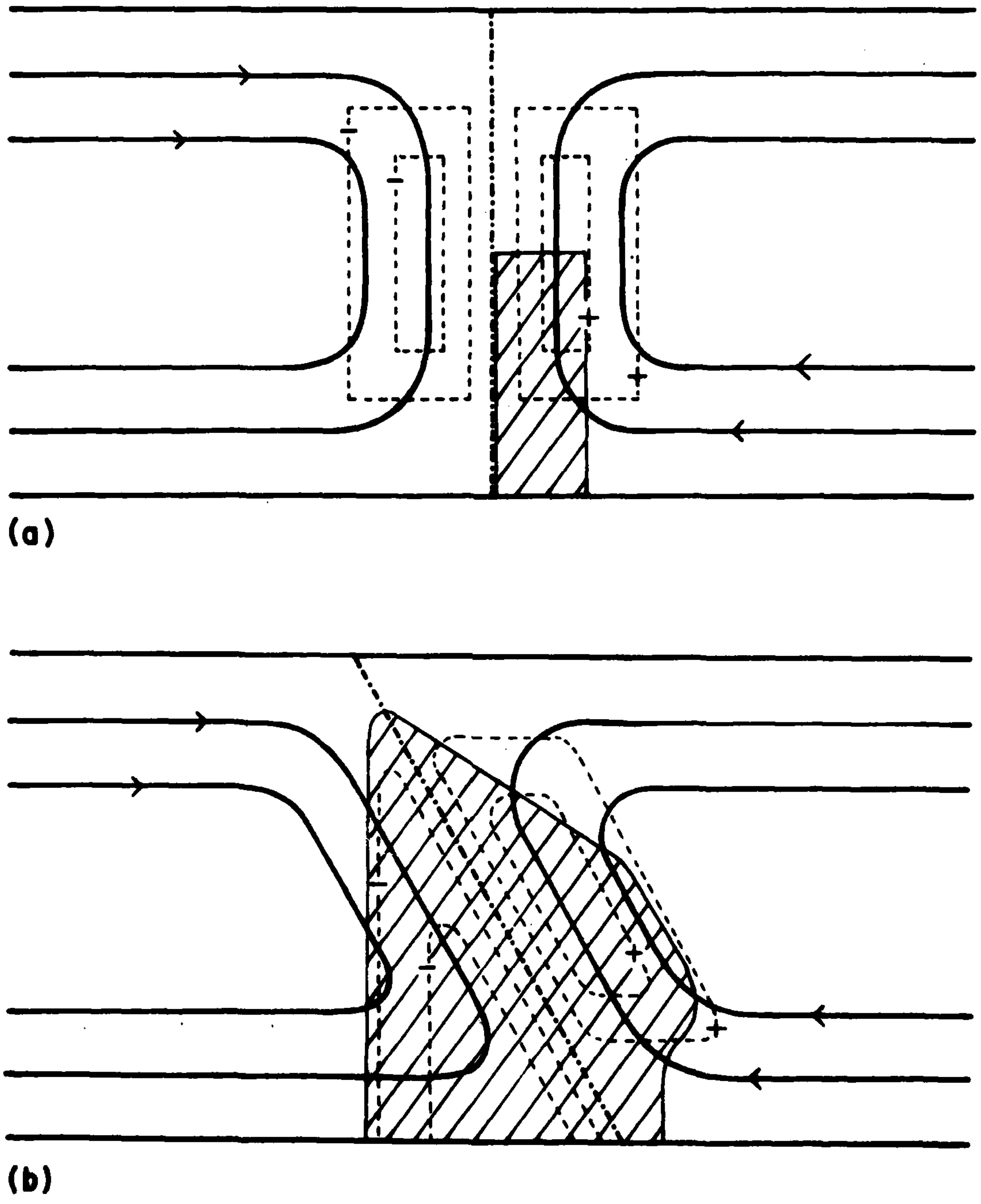

Figure 10. Schematic of overturning circulations. The solid lines are streamlines, the dashed lines are isotherms of positive or negative temperature excess, and the cross-hatched areas represent heavy precipitation.

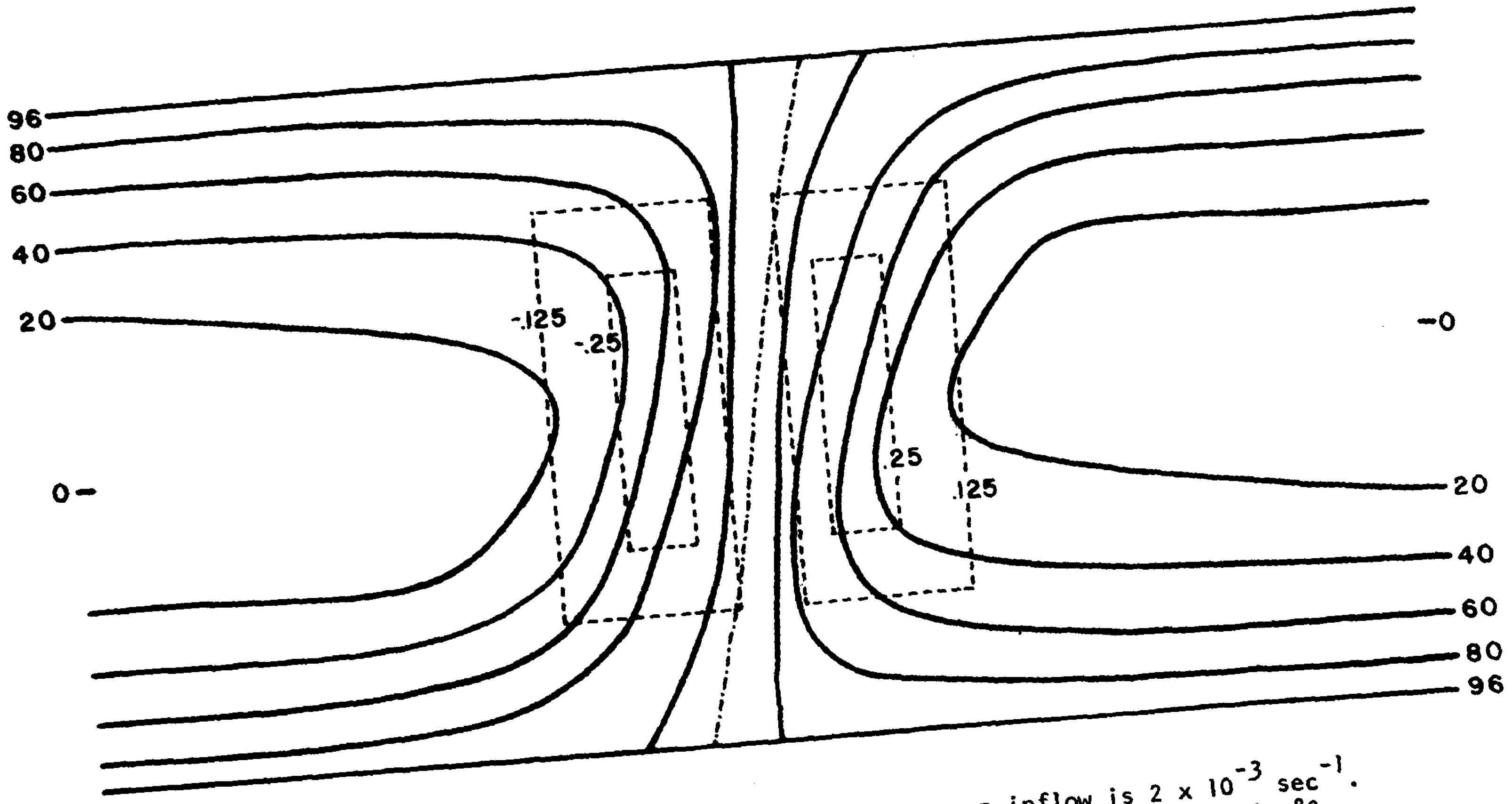

Figure 11. Results of integrating (6.1). The shear on inflow is 2×10^{-3} sec^{-1}. The isotherms of temperature excess are shown as dashed lines and marked in °C. The interface between the updraft and downdraft is shown as a chain line.

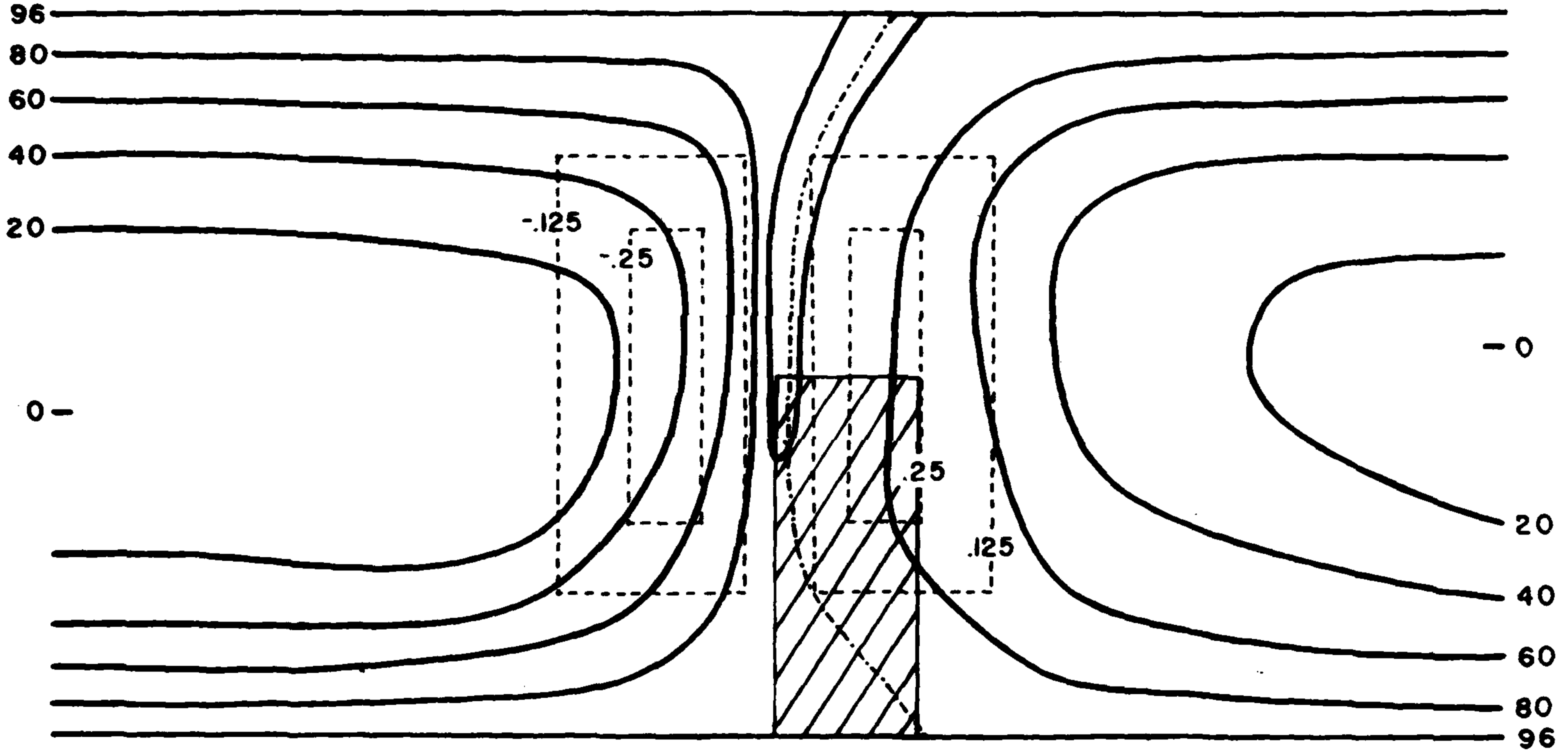

Figure 12. Same as figure 11, except with a liquid water content of 2 gm^{-3} in the cross hatched-area.

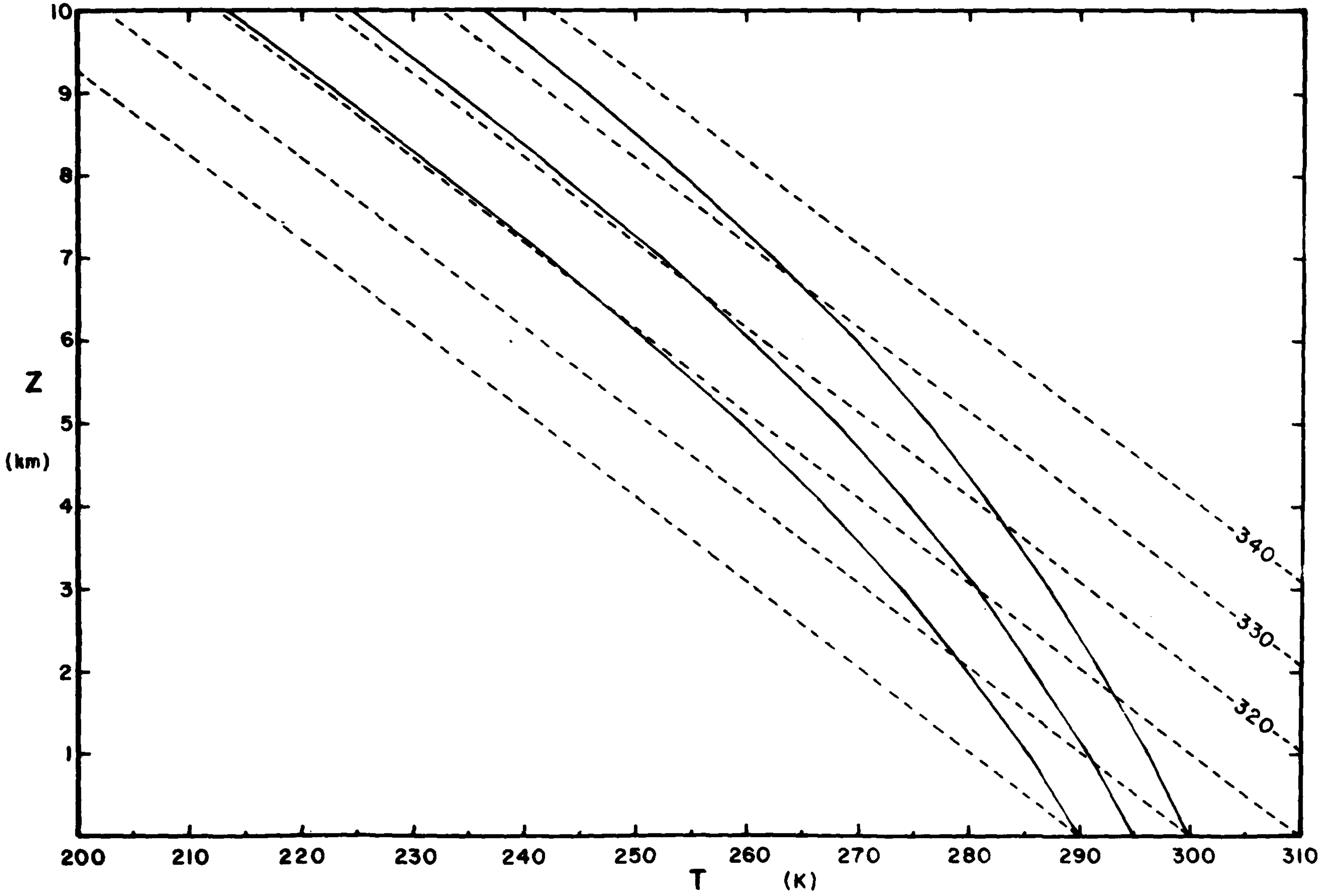

Figure 13. Thermodynamic diagram produced by the model equations for an incompressible atmosphere. The dashed lines are dry adiabats and the solid lines are moist adiabats.

A Radiation Boundary Condition for Multi-Dimensional Flows

Abstract

A 'n' dimensional radiation boundary condition for application at open or computational boundaries is formulated and tested on three two-dimensional problems (n=2). Two of these problems model a simple wave propagation and possess analytic solutions so that the effectiveness of the boundary condition can be measured in terms of a RMS error. A more subjective analysis must be used in the final problem which is the the simulation of an atmospheric cold front. The proposed radiation boundary condition requires the scalar components of the phase velocity. A formula for computing these components is given and various numerical schemes are tested. The traditionally used one-dimensional Sommerfeld radiation condition is recovered when n=1. The higher dimensional radiation boundary condition is found to give significant improvement over the one-dimensional method when the flow is multidimensional.

1. INTRODUCTION

One of the problems facing modelers of meso and other small scale atmospheric phenomena is that in these finite area simulations there is a difficulty in prescribing lateral boundary conditions since no true physical boundary exists. The nature of the environment outside the region under investigation is also unknown. This problem has been forced on many mesoscale investigators and a variety of techniques have been utilized to help eradicate this difficulty, e.g.,

(a) a Sommerfeld radiation condition;
(b) an absorbing boundary;
(c) one sided differencing of the equations;
(d) various other types of extrapolation.

Commonly, these procedures are utilized on some very complicated problems where analytical solutions do not exist hence the impact of any one of these boundary conditons is not known fully. For example, Clark [2] using different expressions for the phase velocity associated with method (a) has found, for flow over a bell-shaped mountain, significant variations in the interior calculations.

What is needed in problems where advection or wave motions dominates, as pointed out by Orlanski [9], is an 'open' boundary condition. Such a condition entails determining if the 'flow pattern' is entering or exiting across a boundary. In the latter case the disturbance should be allowed to propagate out without reflection. It is in this spirit that Orlanski [9] and Pearson [11] proposed to use the following form of the Sommerfeld radiation condition at the boundary:

$$\frac{\partial\phi}{\partial t} + C\frac{\partial\phi}{\partial n_r} = 0, \tag{1}$$

where ϕ is the variable, C the phase velocity, t the time and n_r the coordinate perpendicular to the boundary in question. Pearson [11] proposed estimating C from a linearized dispersion relation while Orlanski [9] proposed to determine C locally and hence to predict the boundary value of ϕ without finding the dispersion relation which as a rule is unknown. It is clear that with the Orlanski approach Eq. (1) can predict accurately one dimensional motion but it does not seem adequate to represent the higher dimensional flows. In this study a 'n' dimensional radiation condition is proposed and tested together with different techniques in evaluating the components of the phase velocity on three two-dimensional problems two of which possess analytic solutions. For more information on other boundary techniques see, e.g., Engquist and Majda [3], Gustafsson and Kreiss [4], Rudy and Strikwerda [13] and Schubert et al. [14].

Typically in limited area or mesoscale atmosphere studies the boundaries are placed as far as possible from the center of activity. To test and evaluate the proposed boundary condition a somewhat different philosophy is taken in that we study the distortion as a phenomena nears and passes through a boundary.

2. A 'n' DIMENSIONAL RADIATION BOUNDARY CONDITION

According to the definition of the phase velocity $\vec{C}$ of the field ϕ, in general we have

$$\frac{\partial\phi}{\partial t} = - \vec{C}\cdot\nabla\phi = - \sum_{i=1}^{n} C_i \frac{\partial\phi}{\partial x_i}, \quad i = 1,2,\ldots,n, \tag{2}$$

where C_i is the component of $\vec{C}$ in the direction of x_i. For our three-dimensional space we have $1 \leq n \leq 3$. We shall use this relation as our general radiation condition at the boundary provided $\vec{C}$ is directed outward from the boundary, and determine C_i by applying the governing equation ϕ which we shall write formally as

$$\frac{\partial\phi}{\partial t} = - F(x_1,\ldots,x_n,t,\phi). \tag{3}$$

Thus, on equating the two expressions of $\partial\phi/\partial t$ given by (2) and (3) we obtain

$$\sum_{i=1}^{n} C_i \frac{\partial\phi}{\partial x_i} = F(x_1,\ldots,x_n,t,\phi) . \tag{4}$$

For the one-dimensional problem, C_1 can be obtained directly from this equation provided F is known. However, for the n dimensional problem with $n > 1$, we need n equations to determine all C_i uniquely. To reduce the number of unknowns to one, we make use of the property of $\vec{C}$ implied by the relation (2), namely $\vec{C}$ is parallel to $\nabla\phi$. In accordance with this property we assume that we have the optimal relation

$$C_i = \alpha \frac{\partial\phi}{\partial x_i} \quad , \tag{5}$$

where the constant of proportionality factor α is the same for all i. On substituting this relation in (4) we then obtain $\alpha = F/\sum_{i=1}^{n} \left(\frac{\partial\phi}{\partial x_i}\right)^2$ and therefore

$$C_i = F \frac{\partial\phi}{\partial x_i} \Bigg/ \sum_{i=1}^{n} \left(\frac{\partial\phi}{\partial x_i}\right)^2 \quad . \tag{6}$$

Equivalently, we may write that each component of $\vec{C}\times\nabla\phi=\vec{0}$ is satisfied and together with Eq. (4) this yields n equations and n unknowns with (6) as the solution. Thus, the value of every C_i at the boundary can be determined from the adequate forms of $\partial\phi/\partial x_i$ and F, such as equating F to the value of $-\partial\phi/\partial t$ at one grid point inside the boundary and one time step earlier, as proposed by Orlanski [9]. This approach will be tested together with the techniques in determining F, by applying it first to two two-dimensional problems where solutions are known analytically, and then to the more complicated two-dimensional cold front problem without known solution.

3. THE THREE TESTING PROBLEMS

Problem A

A two-dimensional advection problem in non-dimensional form given by

$$\frac{\partial u}{\partial t} + \bar{u}\frac{\partial u}{\partial x} + \bar{v}\frac{\partial u}{\partial y} = 0, \quad 0\le x\le 1, \quad 0\le y\le 1, \quad t > 0 \ , \tag{7}$$

is solved for $\bar{u} = \bar{v} = 1$ with initial conditions

$$u(x,y,o) = A\sin 2\pi x \sin 2\pi y. \tag{8}$$

The boundary conditions along the inflow boundaries at $y=0$ and $x=0$ are made to satisfy

$$u(x,y,t) = A\sin 2\pi(x-t)\sin 2\pi(y-t) \quad , \tag{9}$$

which also represents an analytic solution of (7) for every point of the domain.

This solution projects a pattern which moves at a 45° angle toward the upper right corner.

Eq. (7) is solved numerically using a leap-frog scheme, with Robert's filter, for a time step of .01 on a 21 by 21 equally spaced grid having $\Delta x = \Delta y = .05$, and applying the open boundary conditions of the form discussed in section 2 at the outflow boundaries along $x=1$ and $y=1$. The constant A is assigned the value of 100. The RMS error is computed in the traditional manner.

Problem B

Rossby waves, a commonly known large scale atmospheric motion feature represented by the solution of the barotropic nondivergent vorticity equation whose linearized version is given by

$$\frac{\partial \zeta'}{\partial t} + \bar{u}\,\frac{\partial \zeta'}{\partial x} + \bar{v}\frac{\partial \zeta'}{\partial y} + v'\,\frac{\partial f}{\partial y} = 0 \ , \qquad (10)$$

where $\bar{u}$ and $\bar{v}$ are the basic currents in x and y directions, f is the Coriolis parameter and u', v', and ζ' are the perturbation velocities and perturbation vorticity which are expressed in terms of the perturbation stream function ψ by

$$u' = -\frac{\partial \psi}{\partial y}, \quad v' = \frac{\partial \psi}{\partial x}, \quad \zeta' = \frac{\partial v'}{\partial x} - \frac{\partial u'}{\partial y} = \frac{\partial^2 \psi}{\partial x^2} + \frac{\partial^2 \psi}{\partial y^2}, \quad 0 \le x \le x_N \ ,$$

$$0 \le y \le y_M \ . \qquad (11)$$

It is well understood that Rossby waves owe their existence to the variation of the Coriolis parameter f with latitude.

For our testing purposes, i.e., calculations limited to a finite region, we will assume a solution of the form

$$\psi = A \cos k\,(x - \bar{C}_x t) \cos m\,(y - \bar{C}_y t) \ , \qquad (12)$$

$$\zeta' = -A(k^2+m^2) \cos k(x-\bar{C}_x t) \cos m(y-\bar{C}_y t), \qquad (13)$$

where $k = 2\pi/L_x$ is the zonal wave number, $m = 2\pi/L_y$ is the meridional wave number while L_x and L_y are the wave lengths in the x and y directions, respectively. The x component of the phase velocity is

$$\bar{c}_x = \bar{u} - {}^{\beta/}(k^2+m^2), \tag{14}$$

here $\beta = \partial f/_{\partial y}$, while the y component is given by

$$\bar{c}_y = \bar{v}.$$

The initial conditions are given by Eqs. (12) and (13) for t = 0 while the boundaries along x = 0 and y = 0 are also obtained from the analytical solution. The known outflow boundaries along x_N = 3000 km and y_M = 2250 km, for both the vorticity and streamfunction calculations, are used for testing. The unknown streamfunction boundary values are computed using the radiation formulation and the phase velocity components obtained from the vorticity equation. A leap frog scheme is used to solve Eq. (10) and SOR technique is used for Eq. (11). A 21 by 16 evenly spaced grid is used in the x and y directions respectively for a step size of 150 km along with a time step of 2000 s. In addition $\beta = 1.6\times10^{-11}\,\mathrm{sm}^{-1}$, $A = 10^8\ \mathrm{m}^2\ \mathrm{s}^{-1}$, $\bar{u} = 15\ \mathrm{m\ s}^{-1}$, $\bar{v} = 0$ or $5\ \mathrm{m\ s}^{-1}$, L_x = 6000 km and L_y = 3000 km.

Problem C

For the final problem we choose a purely two-dimensional anelastic moist cold front model to simulate the circulation associated with an atmospheric cold front (Ross and Orlanski [12]). A cold front represents a propagating disturbance that can not be described completely as wave motion thus problem C differs from problems A and B. The governing equations for the (x,z) plane are of the form

$$\frac{\partial\eta}{\partial t} = -J(\psi,\alpha_o\eta) + \frac{g}{\theta_o}\frac{\partial\theta_v}{\partial x} - f\frac{\partial v}{\partial z} + \frac{\partial}{\partial x}\left(\nu K\frac{\partial\eta}{\partial x}\right) + \frac{\partial}{\partial z}\left(\nu\frac{\partial\eta}{\partial z}\right) - g\frac{\partial c}{\partial x}, \tag{16}$$

$$\frac{\partial v}{\partial t} = -J(\psi,\alpha_o\eta) + \sigma_z vw + f(u - U_g) + \frac{\partial}{\partial x}\left(\nu K\frac{\partial v}{\partial x}\right) + \frac{\partial}{\partial z}\left(\nu\frac{\partial v}{\partial z}\right), \tag{17}$$

$$\frac{\partial\theta}{\partial t} = -J(\psi,\alpha_o\theta) + \sigma_z\theta w + f\frac{\theta_o v}{g}\frac{\partial U_g}{\partial z} + \frac{\partial}{\partial x}\left(K_e K\frac{\partial\theta}{\partial x}\right) + \frac{\partial}{\partial z}\left(K_e\frac{\partial\theta}{\partial z}\right) + \frac{L\delta}{c_p\pi}, \tag{18}$$

$$\frac{\partial q}{\partial t} = -J(\psi,\alpha_o q) + \sigma_z qw + \frac{\partial}{\partial x}\left(K_e K\frac{\partial q}{\partial x}\right) + \frac{\partial}{\partial z}\left(K_e\frac{\partial q}{\partial z}\right) - \delta, \tag{19}$$

$$\frac{\partial c}{\partial t} = -J(\psi,\alpha_o c) + \frac{\partial}{\partial x}\left(K_e K\frac{\partial c}{\partial x}\right) + \frac{\partial}{\partial z}\left(K_e\frac{\partial c}{\partial z}\right) + \delta + \sigma_z wc. \tag{20}$$

Here u, v and w are the velocity components in x, y and z-directions, $\eta = {}^{\partial w}/\partial x - {\partial u}/_{\partial z}$ is the y-component of vorticity, ψ is the momentum stream function in xz-plane, θ is the potential temperature, g is gravity acceleration, q and c are the water vapor and cloud water mixing ratios, $\theta_v = \theta(1 + .608q)$, U_g is the basic state geostrophic wind, L is the latent heat of condensation, c_p, the specific heat at constant pressure. δ is the condensation rate, ν and K_e are the eddy viscosity and eddy diffusivity coefficients, K is a constant used to enhance the horizontal diffusivity, and $\sigma_z = -\,\partial \ell n \rho_o / \partial z$ is the stratification factor of the undisturbed density ρ_o. Details of how to calculate the condensation rate δ can be found in Ross and Orlanski (12) and Kuo and Qian (7).

In terms of the stream function ψ, the velocities u and w and the vorticity η are given by

$$u = -\,\alpha_o \frac{\partial \psi}{\partial z} \;, \quad w = \alpha_o \frac{\partial \psi}{\partial x} \;, \tag{21a,b}$$

$$\rho_o \eta = \frac{\partial^2 \psi}{\partial x^2} + \frac{\partial^2 \psi}{\partial z^2} + \sigma_z \frac{\partial \psi}{\partial z} \;, \tag{22}$$

where $\alpha_o = {}^1/_{\rho_o}$ and $\rho_o = \rho_{surf} \exp(-\sigma_z z)$ is the vertically varying density.

In our calculations the grid spacing is such that $\Delta x >> \Delta z$. Under these conditions the streamfunction has traditionally been calculated by neglecting the ${\partial^2 \psi}/_{\partial x^2}$ term in Eq. (22) yielding the well known hydrostatic approximation. Orlanski [10] has introduced a quasi hydrostatic approximation in which a correction containing part of the non-hydrostatic contribution is added to the hydrostatic solution. In the Orlanski [10] procedure the streamfunction is represented as

$$\psi = \sum_{j=o}^{m} \psi_j \tag{23}$$

and the components of ψ are obtained from the following equations:

$$\frac{\partial^2 \psi_o}{\partial z^2} + \sigma_z \frac{\partial \psi_o}{\partial z} = \rho_o \eta \;, \tag{24a}$$

$$\frac{\partial^2\psi_j}{\partial z^2} + \sigma_z \frac{\partial\psi_j}{\partial z} = -\frac{\partial^2\psi_{j-1}}{\partial x^2} , \qquad j \geq 1 . \tag{24b}$$

Here ψ_o is the hydrostatic component and the ψ_j's, $j \geq 1$, are an approximation to the non-hydrostatic contribution. The associated boundary conditions are:

$$\text{at } z = 0, \ \psi_j = 0, \text{ for all } j , \tag{25a}$$

$$\text{at } z = H, \ \psi_o = \Psi , \tag{25b}$$

$$\psi_j = 0, \ j \geq 1 . \tag{25c}$$

The series for ψ converges rapidly provided $\Delta x > \Delta z$. Taking $m = 2$ is sufficient for our purposes. Thus the solution of (22) is obtained successively from Eqs. (24a,b).

At the lateral boundaries the right hand side of Eq. (24b) must be approximated. Instead, as an alternative, we choose to let $\frac{\partial\psi_j}{\partial x} = 0$, $j \geq 1$, i.e., the non-hydrostatic terms do not contribute to the vertical velocity at the lateral boundary. Otherwise, there are no lateral boundary conditions required by this procedure.

For the problem in general at the lower boundary, $z = 0$, slip boundary conditions are utilized, e.g., $\eta = 0$, $\frac{\partial\theta}{\partial z} = 0$ and v satisfies the thermal wind relation given by

$$\frac{\partial v}{\partial z} = \frac{g}{f\theta_o}\frac{\partial\theta}{\partial x} . \tag{26}$$

At the upper boundary, i.e., $H = 14$ km., we have a rigid lid so that $w = 0$, thus Ψ is a constant, and in addition η, θ and v keep their initial vertical gradients. Conditions at the lateral boundaries are left for experimentation.

Initially, the thermal wind relation (26) is taken as satisfied by v and θ, and U_g is given some vertical variation. Generally, our initial conditions and the values used in the eddy viscosity formulation as well as all pertinent details for q and c are similar to those used by Ross and Orlanski [12] and thus will not be presented here.

The general numerical approach is composed of a lumped finite element scheme with a leap frog time integration. The Arakawa representation of the Jacobian $J(\psi,\beta)$, where

$$J(\psi,\beta) = \frac{\partial\psi}{\partial x}\ \frac{\partial\beta}{\partial z} - \frac{\partial\psi}{\partial z}\,\frac{\partial\beta}{\partial x} \tag{27}$$

is obtained when bilinear elements (chapeau) are used in the finite element formulation. This was first identified by Jesperson [5]. The diffusion terms are lagged one time step and a Robert's filter is used to reduce the tendency of time splitting. A grid utilizing $\Delta x = 20$ km and $\Delta z = 500$ m is used along with a 100 s time step. The value of Ψ used in Eq. (25b) depends only on the initial u velocity field, the latter is a function of the z coordinate only.

4. NUMERICAL PROCEDURE

Radiation boundary conditions of the form of Eq. (2), for the case n = 2 are to be used in the model problems at the appropriate boundaries as indicated in section 3. For notational purposes rewrite Eq. (2) for the n = 2 case as

$$\frac{\partial\phi}{\partial t} + C_x\frac{\partial\phi}{\partial x} + C_y\frac{\partial\phi}{\partial y} = 0 \quad . \tag{28}$$

Eq. (28) can be used to predict the value of ϕ on an open boundary provided the value of C_x and C_y are known. These values can be obtained via Eq. (6), e.g.,

$$C_x = F\,\frac{\partial\phi}{\partial x}\left[\left(\frac{\partial\phi}{\partial x}\right)^2 + \left(\frac{\partial\phi}{\partial y}\right)^2\right]^{-1} , \tag{29}$$

and

$$C_y = F\,\frac{\partial\phi}{\partial y}\left[\left(\frac{\partial\phi}{\partial x}\right)^2 + \left(\frac{\partial\phi}{\partial y}\right)^2\right]^{-1} . \tag{30}$$

The relationship between C_x and C_y is given by

$$C_x = C_y\ \ {}^{\partial\phi}/_{\partial x}\Big/{}^{\partial\phi}/_{\partial y} \quad . \tag{31}$$

Two methods of evaluating Eqs. (29) and (30) are apparent and are now presented.

An Extrapolation Approach

The values of ϕ at any lateral boundary, say $\phi_{N,j} \equiv \phi(x_N,y_j)$, $j=2,\ldots,M-1$, as predicted by Eq. (28) must be determined numerically. If Eq. (28) is evaluated by a leap frog approach for a time step centered at $t = \tau$ then the correct formulation for C_x^τ and C_y^τ should correspond to the phase velocity components at time τ and centered correctly in space. Provided these C_x's and C_y's are not rapidly varying in time and space an approximation based on previous interior values of ϕ can be made, e.g., Orlanski [9] used $C_N^\tau = C_{N-1}^{\tau-1}$ in the one dimensional radiation boundary condition $(n = 1)$, where $C_N^\tau = C(x_N, t=\tau)$. Other schemes are possible but this approach has the advantage that it is independent of the numerical procedure used in the interior, i.e., to solve Eq. (3). However, various improvements can be made and these will be indicated later.

Assuming, like Orlanski [9], that F is given by $-\partial\phi/\partial t$ centered at $\tau - 1$ and $N - 1$ we find that at the right most boundary (x_N, y_j), excluding corners, of the rectangle region bounded by $0 \le x \le x_N$ and $0 \le y \le y_M$ that Eqs. (29) and (31) can be approximated by

$$C_x = -\frac{1}{2\Delta t}\left[\phi_{N-1,j}^{\tau} - \phi_{N-1,j}^{\tau-2}\right]\frac{\partial\phi}{\partial x}\left[\left(\frac{\partial\phi}{\partial x}\right)^2 + \left(\frac{\partial\phi}{\partial y}\right)^2\right]^{-1}, \tag{32a}$$

$$C_y = C_x \frac{\partial\phi}{\partial y}\Big/\frac{\partial\phi}{\partial x} , \tag{32b}$$

where

$$\frac{\partial\phi}{\partial x} = \left[\frac{\phi_{N-1,j}^{\tau} + \phi_{N-1,j}^{\tau-2}}{2} - \phi_{N-2,j}^{\tau-1}\right]\Big/\Delta x , \tag{32c}$$

and

$$\frac{\partial\phi}{\partial y} = \left[\phi_{N-1,j+1}^{\tau-1} - \phi_{N-1,j-1}^{\tau-1}\right]\Big/2\Delta y . \tag{32d}$$

Thus each of the C_x's and C_y's are located spatially, in the upstream sense, at (x_{N-1}, y_j) and about the $\tau - 1$ time step. The phase velocity components can be used to predict $\phi_{N,j}^{\tau+1}$ via, e.g., an implicit formulation of Eq. (28), yielding,

$$\phi_{N,j}^{\tau+1} = \frac{(1 - C_x\Delta t/\Delta x)}{D}\,\phi_{N,j}^{\tau-1} + \frac{2C_x\;\Delta t/\Delta x}{D}\,\phi_{N-1,j}^{\tau} - \frac{\Delta t C_y}{\Delta y}\left[\frac{\phi_{N,j+1}^{\tau} - \phi_{N,j-1}^{\tau}}{D}\right] , \tag{33}$$

where $D = 1 + C_x\Delta t/\Delta x$ and with the restriction given in Orlanski [9] expanded so that

$$C_x = \begin{cases} 0 \ , & C_x \leq 0 \ , \\ C_x \ , & o \leq C_x \leq \Delta x/\Delta t \ , \\ \Delta x/\Delta t \ , & C_x \geq \Delta x/\Delta t \ , \end{cases} \tag{34a}$$

and

$$C_y = \begin{cases} \Delta y/\Delta t \ , & C_y > \Delta y/\Delta t \ , \\ C_y \ , & -\frac{\Delta y}{\Delta t} \leq C_y \leq \Delta y/\Delta t \ , \\ -\Delta y/\Delta t \ , & C_y < -\Delta y/\Delta t \ . \end{cases} \tag{34b}$$

Similar formula can be written down for the lateral boundaries at (x_i, y_M), etc. If corners are to be computed then both C_x and C_y must be computed using one-sided differencing. Note that the Orlanski [9] formulation for the one dimensional radiation condition is recovered above if $C_y = 0$. Also, if the properties at an inflow boundary are known then Eq. (33) need not be used in that situation.

Bannon [1] and Miller and Thorpe [8] have both proposed an upstream time differencing scheme to evaluate the one-dimensional Sommerfeld radiation boundary condition. The latter authors suggest using

$$\phi_N^{\tau+1} = \phi_N^{\tau} - r\,(\phi_N^{\tau} - \phi_{N-1}^{\tau}) \ , \tag{35}$$

where $r = C\,\Delta t/\Delta x$, $o \leq r \leq 1$, and r is determined from

$$r = \left(\phi_{N-1}^{\tau+1} - \phi_{N-1}^{\tau}\right) \Big/ \left(\phi_{N-2}^{\tau} - \phi_{N-1}^{\tau}\right) \ . \tag{36}$$

In addition, Miller and Thorpe [8] performed a truncation error analysis and found that improved accuracy is obtained when

$$r = \left(\phi_{N-1}^{\tau+1} - \phi_{N-1}^{\tau}\right) \Big/ \left(\phi_{N-2}^{\tau} - \phi_{N-1}^{\tau}\right) + \left(\phi_N^{\tau} - \phi_N^{\tau-1}\right) \Big/ \left(\phi_{N-1}^{\tau-1} - \phi_N^{\tau-1}\right) \tag{37}$$

$$- \left(\phi_{N-1}^{\tau} - \phi_{N-1}^{\tau-1}\right) \Big/ \left(\phi_{N-2}^{\tau-1} - \phi_{N-1}^{\tau-1}\right) \ .$$

We will make comparisons between both the leap frog and upstream time differencing schemes.

Note that Eqs. (36) and (37) require an interior value evaluated for time step $\tau+1$.

If the interior calculations are made using a leap frog or some explicit scheme then the computed solutions at time $\tau+1$ can be utilized in the lateral boundary calculations. Under these conditions τ may be replaced with $\tau+1$ in Eqs (32a) through (33). The phase velocity components are then centered correctly in time for the leap frog integration scheme given above. For some problems it is possible to compute the phase velocity correctly in both time and space.

Equating To The Equation Technique

Again assume a leap frog time integration scheme for Eq. (28). If in Eqs (29) and (30) it is possible to evaluate $F(x,y,t,\phi)$, described by Eq (3), at the boundary at time τ using one-sided differencing then C_x and C_y are obtained centered spatially at $(x_{N-\frac{1}{2}}, y_j)$ and at the τ time step. If F is a complicated function then this one-sided differencing approach will be more involved than the extrapolation procedure. In addition one sided differencing may itself introduce large errors especially if the equation contains terms that are in a state of near quasi balance, e.g. the geostrophic balance condition in the primitive equations of motion and the thermal wind balance condition in the vorticity equations. This error can be removed to a certain extent provided higher order finite differencing approximations are used at the boundaries. It is best to avoid this type of error if possible. Nevertheless in our model problem A and B this technique can be used to help measure the error introduced by using the extrapolation procedure described above. Thus given the values of C_x and C_y for Eqs (29) and (30) the value of $\phi^{\tau+1}_{N,j}$ is obtained as before via Eq (33).

5. DISCUSSION OF RESULTS

In order to test the 'n' dimensional radiation boundary condition, three distinct two-dimensional problems have been proposed. For problems A and B the use of boundary conditions at the known outflow boundaries over specifies these problems since they are first order in each of the independent variables. However this over specification is one possible method that can be used to test the ramifications of any technique that might be proposed for use at an open or computational boundary.

Results From Problem A

Starting with problem A we show in Table 1 the RMS error after one hundred time steps. The results using both a one and two dimensional radiation condition are shown for two methods of determining the phase velocities. The extrapolation approach, described in Eqs (32a-d), as indicated goes back one time step from the last known value at the boundary and interior to the boundary one space step to determine the C_x's and C_y's while the equating to the equation technique evaluates these phase velocity components using one sided finite differencing of terms in the governing equation. Orlanski [9] first proposed the extrapolation procedure with the one dimensional radiation boundary condition. Under the extrapolation approach note that there is a five fold reduction in the RMS error by increasing the radiation boundary condition from one dimension $(n=1)$ to two dimensions $(n=2)$. The RMS error is further reduced for both the one and two dimensional radiation conditions by using the equating to the equation technique. For this problem the two dimensional radiation condition has exactly the same form as the equation being solved so it is not surprising that the RMS error is essentially identical to that given by using one sided finite differencing. Limiting the radiation condition to one dimension increases the error substantially. Using the known analytical solution on all boundaries does not reduce the error, as shown in Table 1, due to inaccuracies in the interior numerical calculations.

In Fig. 1 values of C_x for the first fifty time steps are shown at location (x_N, y_{12}). The solid line is for the one dimensional radiation condition while the dashed curve is for the two dimensional case. Both are for the extrapolation leap frog method of determining the C_x's or C's. The dotted curve represents the C_x's obtained using the two-dimensional equated to the equation technique. For the two-dimensional cases all values are to be compared against the analytically predicted value of 1.

Substituting the analytical solution into the one dimensional boundary condition, Eq (1), yields an analytically predicted time dependent solution for the phase velocity, i.e.,

$$C = 1 + \frac{\tan 2\pi(x-t)}{\tan 2\pi(y-t)} \quad , \tag{38}$$

which becomes infinitely large in magnitude when

$$2\pi(y-t) = \pm j\pi, \quad j = 0,1,\ldots$$

or

$$2\pi(x-t) = \pm\frac{h\pi}{2} \ , \ h = 1,3,5\ldots \quad .$$

This explains why in the numerical procedure the value of C (solid line) fluctuates rapidly and is quasi periodic in time. Nevertheless the value of C must be restricted (Orlanski, [9]) i.e., $o \leq C \leq \frac{\Delta x}{\Delta t}$, otherwise substitution of C back into the formula (Eq 33, n=1) to predict the new boundary value of the dependent variable u would numerically make no sense.

Results for Problem B

In Table II some RMS errors are given for problem B, the Rossby waves, after a total of one hundred time steps or 55.55 hrs. The results are presented in a format similar to that given in Table I except two cases are given. The first two columns of the RMS errors for the vorticity and streamfunction, respectively, are for when the true phase velocity is entirely in the x direction, i.e. $\bar{C}_y = o$, while columns three and four are for when the phase velocity has components in both coordinates. The latter occurs when $\bar{v}$ is non zero.

In Table II note that when $\bar{v} = o$ the one and two dimensional methods give approximately the same RMS errors in each category used to determine the phase velocity. The extrapolation approach gives the largest errors, as compared to the equating to the equation technique, and predicts changes along the $y=y_M$ boundary when in fact no changes occur. When the mean flow contains components in both the x and y directions the two dimensional radiation condition again becomes superior as seen in columns three and four. Also notice that the two-dimensional equating to the equation technique and one sided finite differencing give nearly identical solutions. This implies at the known out flow boundaries that the components of the phase velocity are predicting outflow and thus satisfy the restrictions imposed by Eqs. (34a,b).

In Fig. 2 values of C_x along the boundary $x=x_N$ are displayed at the fiftieth time step. The solid and dashed curves are C's for n=1 and C_x's for the n=2 cases, respectively, obtained by the extrapolation approach. The dotted curve is found from the two-dimensional equated to the equation technique. The analytically predicted value for the components of the phase velocity are $C_x=\bar{C}_x$ and $C_y=\bar{C}_y$. Substituting the analytical solution for the vorticity, Eq (13), into the one dimensional radiation condition gives an analytically predicted value for the phase velocity, i.e.,

$$C = \bar{C}_x + \bar{C}_y \frac{m}{k} \tan m\,(y-\bar{C}_y t) \Big/ \tan k(x-\bar{C}_x t) \quad . \tag{39}$$

Here our previous finding is again repeated since this equation predicts that in the one dimensional case the phase velocity can take on values much in excess of the acceptable upper limit, i.e., $C = \frac{\Delta x}{\Delta t}$, and values much less than the lower limit $C = 0$. The latter is obtained inspite of the fact that the flow is continuously outward. The sharp spike in the solid curve, Fig 2, reflects this large variability and is commonly found at least at one grid point at almost every time step and often exceeds the maximum magnitude allowable. It is clearly seen in Eq. (39) and in Tables I and II that theuseof the one dimensional radiation boundary condition incursgreater errors as the flow becomes increasely multi-dimensional.

In Table III the RMS errors associated with the upstream time differencing schemes of Miller and Thorpe [8] are given. The simplier of their two schemes, computed using Eq (36) for n=1, gives nearly identical results with the one-dimensional (n=1) case evaluated using Eqs (32a-d) with τ replaced by $\tau + 1$. Utilizing the interior solutions evaluated at time $\tau + 1$ in the lateral boundary calculations does not change the RMS error appreciatively either positively or negatively as seen by comparing Tables II and III. The interpolation of r and hence C by Eq (37) does show definite improvement except for the streamfunction calculations when there is two-dimensional mean flow. With further integrations the large error in the latter category will eventually deteriorate the vorticity solutions.

Some severe storm modelers have had success using a constant phase velocity in the one-dimensional radiation condition, e.g., see Klemp and Wilhelmson [6]. Table IV shows the RMS errors when C_x and C_y are each held fixed. Using the analytically predicted values of $C_x = 12.082$ and $C_y = 0$ or 5 in Eq (33) gives RMS errors essentially identical to the one-sided finite differencing. From Table IV we also see that for one dimensional flow the error occurred by over estimating C_x is less than when C_x is underestimated. However this pattern is not clearly reproduced when the flow is two-dimensional. With the higher dimensional radiation condition it may also be acceptable, under some circumstances, to use a fixed or constant value for each component of the phase velocity provided enough information is available to determine the nearly correct magnitudes and directions.

Results For Problem C

Problem C requires the numerical solution of several equations. Even though complicated by the release of the latent heat the procedure is nevertheless straight foreward except for the conditions to be used at the open boundaries. At the lateral boundaries we tested a variety of different conditions for the various equations. These tests show that the procedure used by Clark [2], and many others, is very satisfactory, i.e., the velocity component normal to the lateral boundary is computed at the boundary from the radiation condition while all other dependent variables have zero normal gradients. Thus in our problem at the lateral boundaries θ,q,c and v satisfy $\frac{\partial}{\partial x}(\ ) = 0$ while the radiation boundary condition is applied to the vorticity equation from which the normal velocity component is computed via the streamfunction.

Our results for the atmospheric cold front simulation are very similar to those obtained by Ross and Orlanski [12]. Details of the various fields, e.g., vorticity, streamfunction, etc., are very involved and it is not easy to gauge from these the influence that the lateral boundaries might play. A clearer picture showing the influence of the various radiation boundary condition formulations is gained by examining plots of an averaged quantity or spacial norm verses time. Figs. 3 and 4 display our choices.

In Fig. 3 we plot $\bar{u}'$ verses time where $\bar{u}'$ is the norm of the perturbation velocity as defined by

$$\bar{u}' = \frac{1}{N\cdot M} \sum_{i=1}^{N} \sum_{j=1}^{M} |u_{i,j} - U_g| \quad . \tag{40}$$

Here u is the computed x component of the velocity field while U_g is the geostrophic wind which is a function of the vertical coordinate only. This norm is choosen because it allows for an easy interpretation of the magnitude of the perturbation velocity.

In Fig. 3 the solid curve displays the results obtained using the two dimensional radiation condition (n=2) for the extrapolation techniques while the dashed-dot curve is the Orlanski procedure (n=1) and the dashed curve is the Miller-Thorpe technique using the improved estimates of r as given in Eq (37). The dotted curve which is essentially identical to the solid curve uses phase velocity components (n=2) centered correctly at time τ for the leap frog scheme but still computed by the extrapolation procedure. In these calculations only the radiation boundary condition has been changed. Also the area of computation coincides with the region over which the averaging is performed. The grid is as defined in section 3 for the x and z coordinate system utilizing N=55 and M=29. The above mentioned curves are to be compared and contrasted with the plus (+) curve which gives an average over the same area but when the calculations are performed on a larger area having N=73.

Two features are pronounced in comparing the various curves. First, there is some adjustment to the initial conditions and all the curves show an increase in magnitude which reaches a maximum at sixteen hours. During this process the curves are very similar. After the adjustment process the plus curve shows that a quasi steady state exists. Here the small variations are due to the presence of internal gravity waves. The second feature is now apparent since the other curves reveal that the lateral boundary has a large impact if the disturbance is too close. The Miller-Thorpe procedure is particularly susceptible since boundary influences cause the value of $\bar{u}'$ to more than double the maximum magnitude observed in the plus curve. The two dimensional radiation boundary condition (solid or dotted curves) displays the smallest increases for times greater than thirty hours. The small differences between the curves computed using the one and two-dimensional radiation boundary conditions, before thirty three hours, can be explained by the fact that away from the frontal zone the u component of the velocity is at least two orders of magnitude larger than the vertical velocity component. Thus the flow is essentially one dimensional except near the front. This is clearly seen by the magnitudes of $\bar{w}$ in Fig. 4.

In Fig. 4 values of $\bar{w}$, where

$$\bar{w} = \frac{1}{N \cdot M} \sum_{i=1}^{N} \sum_{j=1}^{M} |w_{ij}| \tag{41}$$

are shown for calculations using the same radiation conditions as in Fig. 3 except now the dashed curve is the Miller-Thorpe upstream technique computed using Eq(36). Again the lateral boundary effects are clearly evident after thirty three hours in the leap frog schemes which give very similar results and after twenty six hours in the upstream procedure (dashed curve). The latter technique generates vertical velocity averages twice as large as the leap frog scheme. The exact reason the upstream procedure is less effective is unclear in light of its performance in problem B (Table III). The flow pattern is however much more complicated in problem C and it seems reasonable that a boundary procedure that uses the same time integration scheme (leap frog) as used in the interior calculations would be the most compatible for long time integrations.

In Eqs. (17) through (20) w appears explicitly in one term in each equation. In our calculations we compute w from calculated streamfunction values via the formula $w = \alpha_o \frac{\partial\psi}{\partial x}$ in finite element representation.

Along the lateral boundaries however the finite element technique predicts each w using streamfunction values in a one sided differencing scheme from six grid points. To test whether the reduced accuracy associated with the one sided differencing scheme might be enhancing the error at the lateral boundaries we replaced the direct calculation of w with the condition that $\frac{\partial w}{\partial x} = o$. This greatly reduces the noise generated at the lateral boundaries as seen by comparing values of $\bar{w}$ in Table V, computed using $\frac{\partial w}{\partial x} = o$, against our earlier calculations of $\bar{w}$ in Fig. 4 in which w was calculated at the lateral boundaries. All categories of radiation boundary conditions show improvement with now almost no differences between the n=1 and n=2 cases. However the leap frog approach still remains superior to the up-stream technique.

In our lumped finite element scheme every term in Eqs. (17) through (20) is expressed in a nine point configuration except for the time term. Hence the contribution from every term that includes w can be interpreted in terms of the streamfunction as representing even more grid points since the calculation of each w involves ψ on nine grid points. Consequently using w instead of the streamfunction representation explicitly obviously results in some smoothing. This fact is reflected in the values of $\bar{w}$ shown in Table VI. In the last two lines in Table VI it is clear that when the calculations are performed using $\alpha_o \frac{\partial\psi}{\partial x}$ explicitly in place of w the values of $\bar{w}$ are nearly a magnitude larger after forty-eight hours. The differences are small during the first six hours but as latent heat is released at grid point locations in the condensation process the differences grow. Unfortunately the intensified flow characteristics obtained when using the streamfunction representation explicitly also enhances all noise and the solutions become very noisy after twenty simulation hours. Thus it is difficult to test radiation conditions when the meteorological fields deteriorate beyond the point of interpretation. Nevertheless the result for $\bar{w}$ displayed in Table VI agrees essentially with our previous findings.

To determine if the error at the lateral boundaries can be reduced even further we tested several other ideas. For example, in an attempt to center the phase velocity component correctly in space we computed two columns of components adjacent to the boundary and then utilized a Taylor series expansion to predict the value at the boundary. These calculations did not significantly improve the results presented above. Using higher order approximations of the derivatives also did not significantly change our results. Also averaging all quantities over six grid points, as computed via the finite element method with bilinear basis elements, yields essentially the same results. As previously mentioned the equating to the equation technique cannot be utilized in this problem because of the internal balance between two derivative terms in the vorticity equation, i.e., the thermal wind relation.

6. SUMMARY

A 'n' dimensional radiation boundary condition has been tested on three two dimensional problems. When the flow is outward across a lateral boundary and when the pattern of movement is multi-dimensional the proposed radiation condition has been found to be clearly superior to various formulations of the traditionally used one dimensional Sommerfeld radiation condition. For outflow the 'n' dimensional radiation boundary condition, as proposed, is equivalent to one-sided differencing of the governing equation provided the components of the phase velocity are correctly centered in time and space. When this centering procedure is not feasible or gives unrealistic results extrapolation procedures provide an alternative technique to determine the phase velocity components.

REFERENCES

1. P. R. Bannon, "On the Dynamics of the East African Jet", Ph.D. Thesis, University of Colorado, Boulder, CO, 1979.
2. T. L. Clark, *J. Atmos. Sci. 36* (1979), 1291.
3. B. Engquist and A. Majda, *Math. Comp. 31* (1977), 639.
4. B. Gustafsson and H. -O. Kreiss, *J. Comput. Phys. 30* (1979), 333.
5. D. C. Jespersen, *J. Comput. Phys. 16* (1974), 383.
6. J. B. Klemp and R. B. Wilhelmson, *J. Atmos. Sci. 35* (1978), 1070.
7. H. L. Kuo and Y. F. Qian, *Mon. Weather Rev.*, to appear.
8. M. J. Miller and A. J. Thorpe, *Quart. J. Roy. Meteorol. Soc. 107* (1981), 615.
9. I. Orlanski, *J. Comput. Phys.* 21 (1976), 251.
10. I. Orlanski, *J. Atmos. Sci.* 38 (1981), 572.
11. R. A. Pearson, *J. Atmos. Sci. 31* (1974), 1481.
12. B. B. Ross and I. Orlanski, *J. Atmos. Sci. 35* (1978), 445.
13. D. H. Rudy and J. C. Strikwerda, *J. Comput. Phys. 36* (1980), 55.
14. W. H. Schubert, J. J. Hack, P. L. Silva Dias and S. R. Fulton, *J. Atmos. Sci. 37* (1980), 1464.

TABLE I

RMS errors after 100 time steps for problem A.

Boundary Condition	RMS error
(I) Extrapolated	
$\frac{\partial\phi}{\partial t} + C\frac{\partial\phi}{\partial n_r} = 0$ (Ia)	2.024
$\frac{\partial\phi}{\partial t} + C_x\frac{\partial\phi}{\partial x} + C_y\frac{\partial\phi}{\partial y} = 0$ (Ib)	.3956
(II) Equated to the equation	
$\frac{\partial\phi}{\partial t} + C\frac{\partial\phi}{\partial n_r} = 0$ (IIa)	.4224
$\frac{\partial\phi}{\partial t} + C_x\frac{\partial\phi}{\partial x} + C_y\frac{\partial\phi}{\partial y} = 0$ (IIb)	.1383
(III) One sided finite differences	.1380
(IV) Analytical exact value	.2020

TABLE II

RMS errors after 100 time steps for problem B.

	$\bar{u} = 15$ m s^{-1} $\bar{v} = 0$		$\bar{u} = 15$ m s^{-1} $\bar{v} = 5$ m s^{-1}	
Boundary Condition	Vorticity, $10^{-5} s^{-1}$	Streamfunction, 10^{6} m^{2} s^{-1}	Vorticity, 10^{-5} s^{-1}	Stream-function, 10^{6} $m^{2}s$
(Ia)	.1336	.8650	.5971	1.5072
(Ib)	.1308	.7180	.1521	.2878
(IIa)	.0112	.0296	.0674	.6995
(IIb)	.0112	.0270	.0475	.1929
(III)	.0113	.0270	.0448	.1977

TABLE III

RMS errors after 100 time steps for upstream and leap-frog radiation schemes used in problem B.

	$\bar{u} = 15$ m s^{-1} $\bar{v} = 0$		$\bar{u} = 15$ m s^{-1} $\bar{v} = 5$ m s^{-1}	
Schemes	Vorticity, 10^{-5} s^{-1}	Streamfunction, 10^{6} m^{2} s^{-1}	Vorticity, 10^{-5} s^{-1}	Stream function 10^{6} m^{2} s^{-1}
Up stream Eq. (36)	.128	.8166	.561	1.4631
Eq. (37)	.0298	.1245	.1300	1.6006
Leap Frog				
n = 1	.1285	.8171	.5864	1.5106
n = 2	.1287	.6861	.1642	.3212

TABLE IV

RMS errors after 100 time steps for constant phase velocity components in the radiation condition used in problem B

Boundary Condition		$\bar{u} = 15$ m s^{-1} $\bar{v} = 0$		$\bar{u} = 15$ m s^{-1} $\bar{v} = 5$ m s^{-1}	
C_y	C_x	Vorticity, $10^{-5}s^{-1}$	Streamfunction, 10^6 m^2s^{-1}	Vorticity, $10^{-5}s^{-1}$	Stream function, 10^6 m^2 s^{-1}
0.0	12.082	.0114	.0298	.6846	1.2197
5.0	12.082			.0434	0.1974
0.0	5.0	.1521	.6614	.8748	1.4602
0.0	25.0	.0640	.3658	.6116	1.6686

TABLE V

Values of $\tilde{w}$ (10^{-2}) computed for problem C when $\partial w/\partial x = 0$ at the lateral boundaries.

	Time (hrs)					
Scheme	25	30	35	40	45	48
Upstream						
Eq.(36)	.319	.509	.638	.554	.379	.319
Eq.(37)	.413	.457	.467	.360	.340	.228
Leap frog						
n = 1	.298	.286	.308	.263	.245	.267
n = 2	.299	.296	.318	.268	.247	.260
Large area						
n = 2	.247	.259	.283	.265	.222	.211

TABLE VI

Values of $\tilde{w}$ (10^{-2}) computed for problem C when w is replaced with $\alpha_o\ \partial\psi/\partial x$ in Eqs (17) through (20) or when w is used explicitly.

	Time (hrs)						
	1	4	8	16	24	28	48
using ψ							
Up stream Eq. (36)	.104	.203	.339	2.431	2.098	2.565	3.577
Eq. (37)	.104	.203	.341	2.584	2.353	2.418	1.489
Leap frog							
n = 1	.104	.206	.342	2.374	2.459	1.897	1.502
n = 2	.104	.207	.342	2.376	2.464	1.929	1.556
Large area							
n = 2	.104	.202	.305	2.344	1.918	1.818	1.491
using w							
Large area							
n = 2	.098	.184	.222	.452	.273	.283	.211

List of Figures

Fig. 1. Values of the phase velocity components are displayed for the first fifty time steps for location (x_N, y_{12}) in problem A. Values computed using the one dimensional, n=1, (solid curve) and two dimensional, n=2, extrapolated (dashed) and equated to the equation technique (dotted) are to be compared against $C_x=1$.

Fig. 2. Same as Fig. 1 except for problem B and computed for the fiftienth time step along the right lateral boundary. The known analytical solution is shown by the $C_x = \bar{C}_x$ curve.

Fig. 3. For problem C values of $\bar{u}'$ verses time are shown when in the radiation condition n=2 (solid and dotted curves), for n=1 (dashed dot) and for an upstream time differencing scheme (dashed curve) using Eq. (37).

Fig. 4. Same as Fig. 3 except for $\bar{w}$ and the upstream scheme uses Eq. (36).

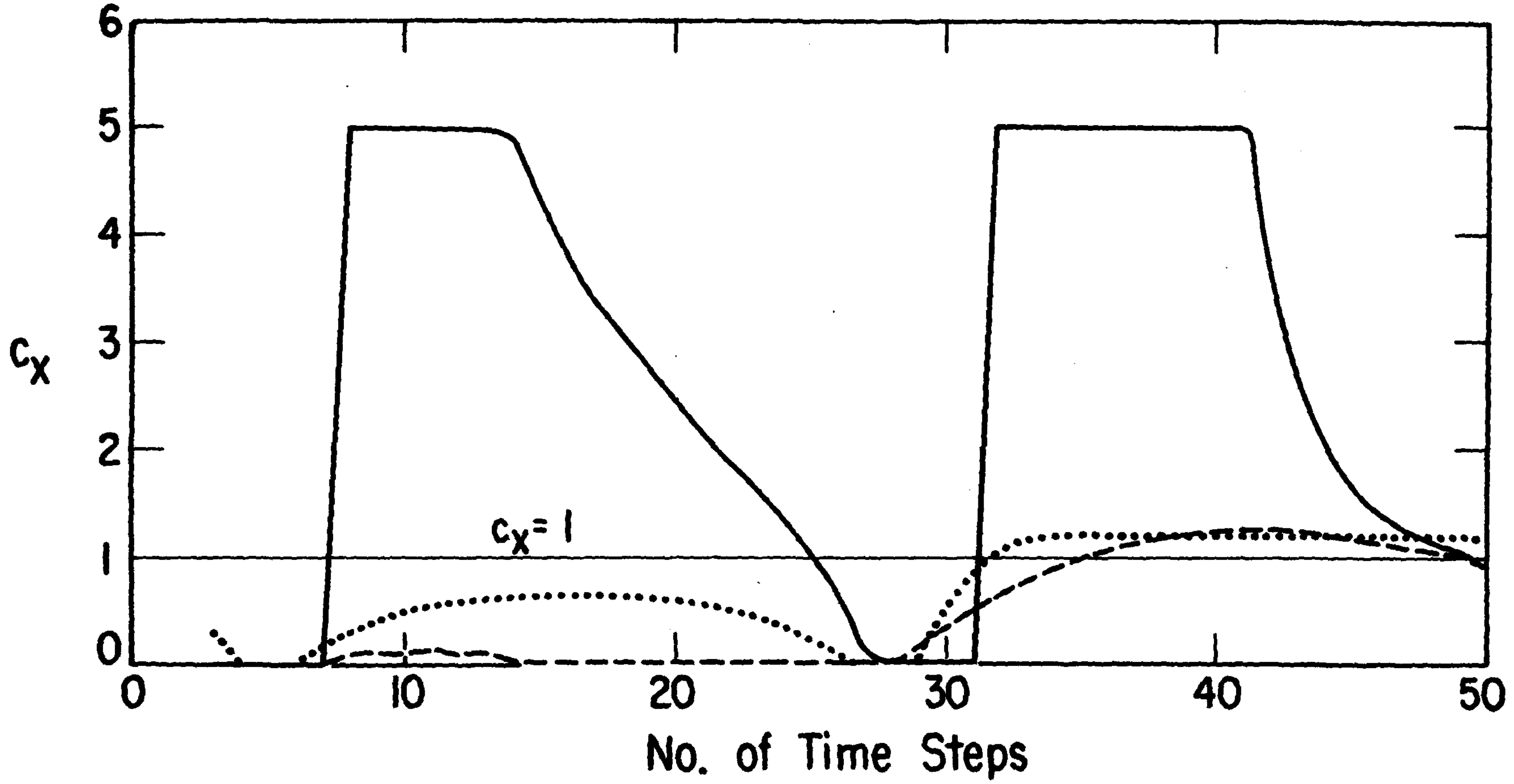

Fig. 1

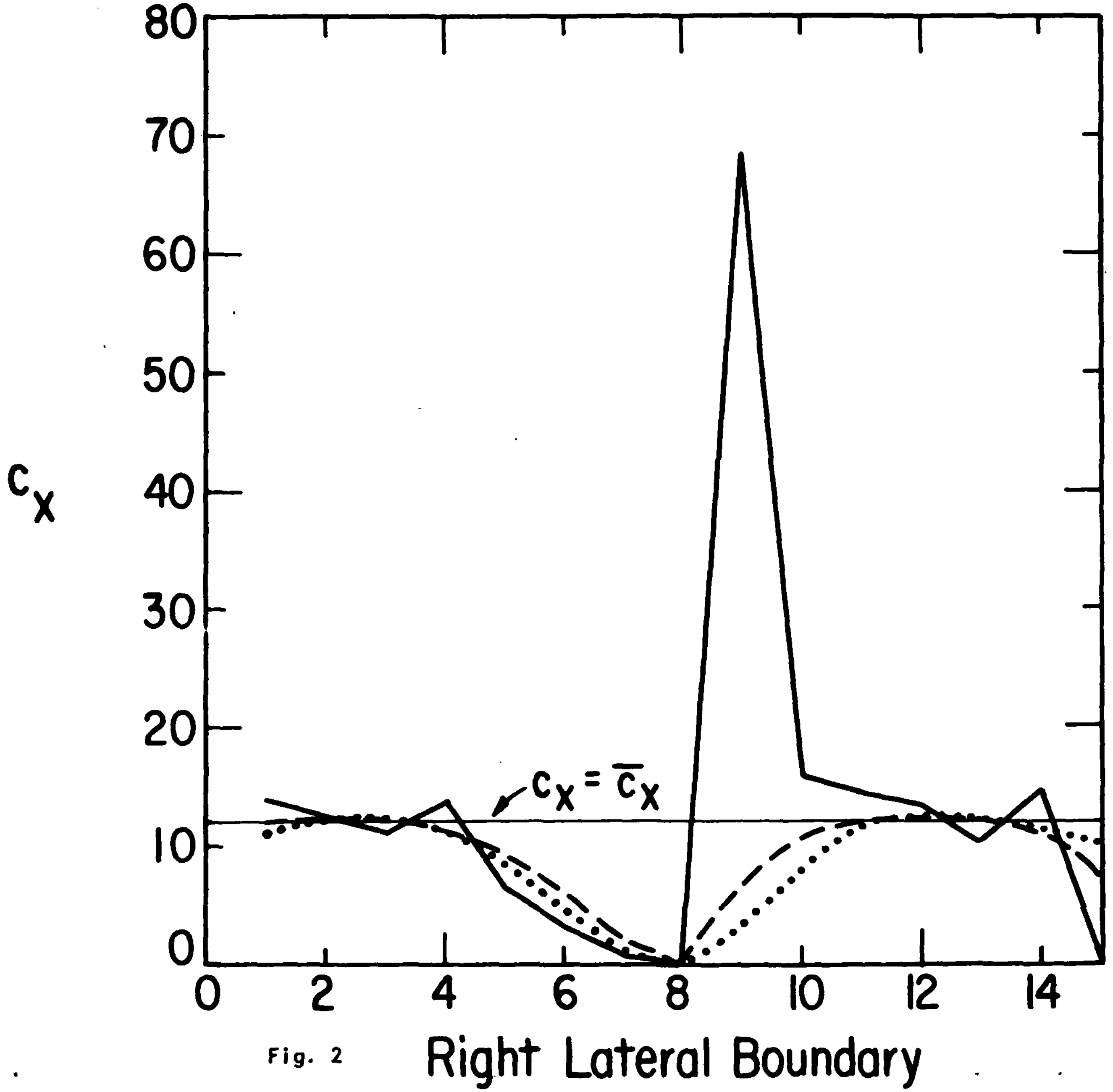
80
70
60
50
40
30
20
10
0
c_x
$c_x = \bar{c}_x$
0
2
4
6
8
10
12
14
Right Lateral Boundary

Fig. 2

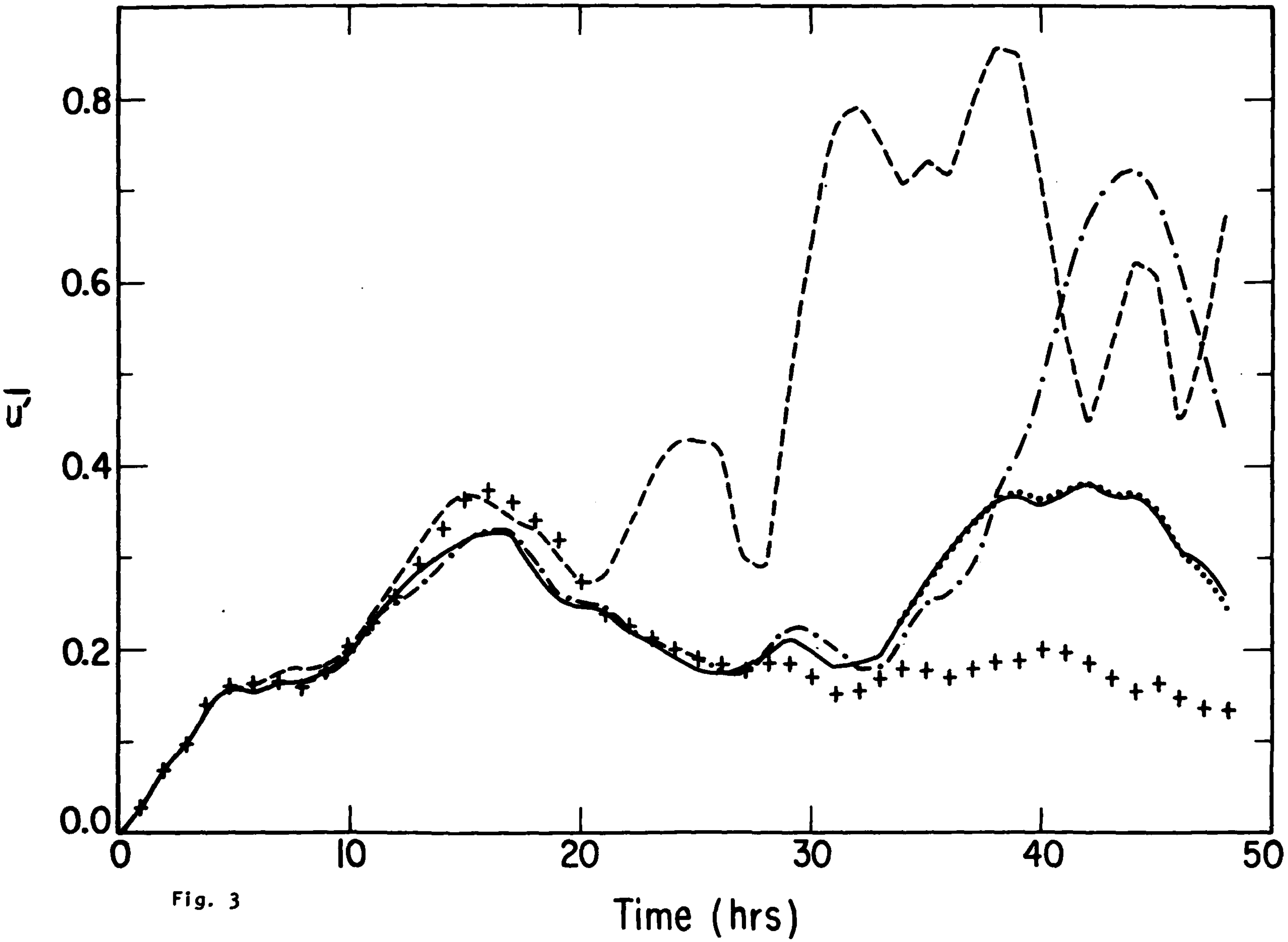

Fig. 3

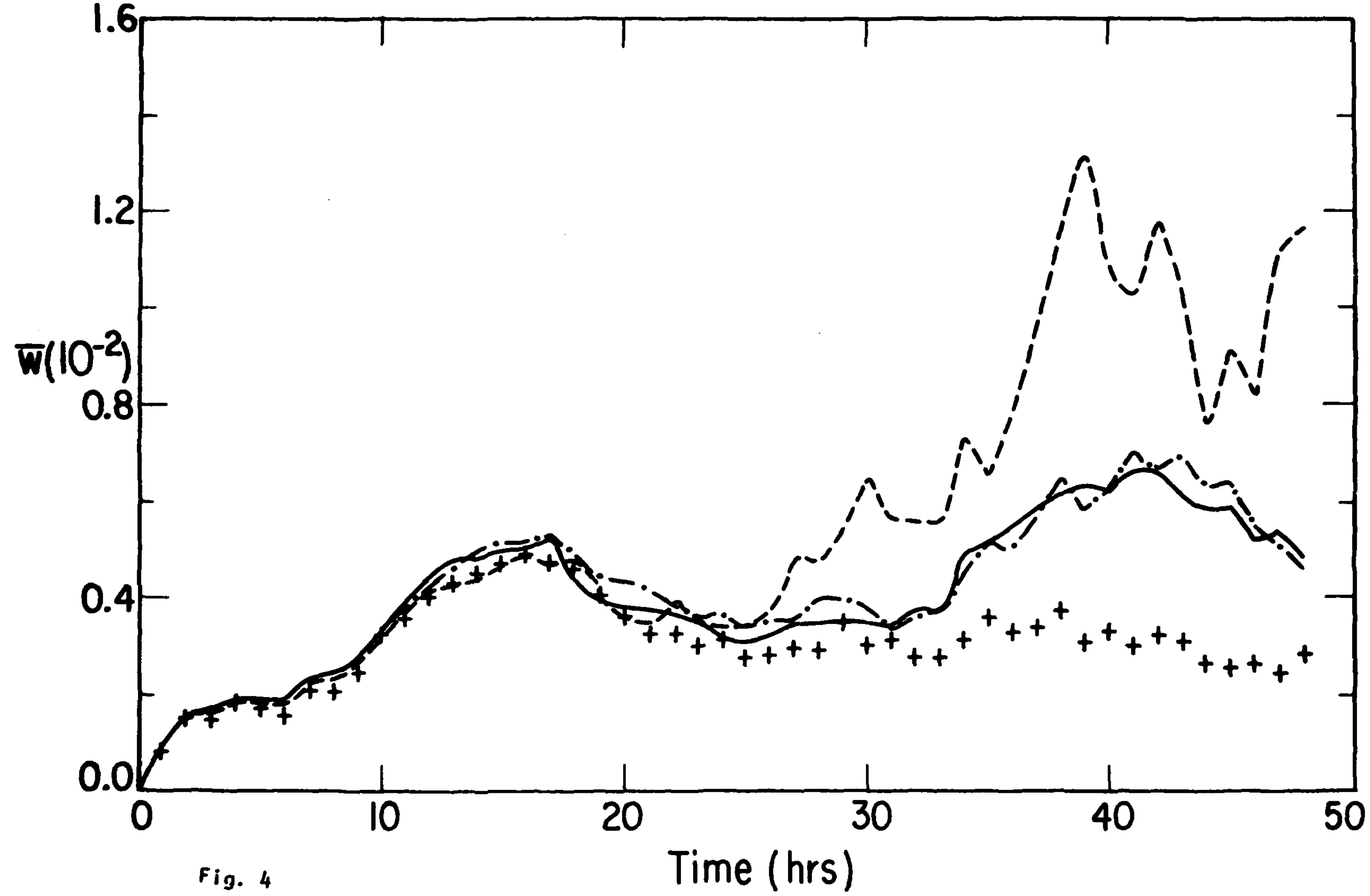

Fig. 4

Simulation of Laboratory Vortex Flow by Axisymmetric Similarity Solutions

Abstract

A similarity approach is utilized to investigate a simple axisymmetric steady-state model of the convergence region of a laboratory vortex. The resulting simplified set of equations are solved for a range of swirl angles by varying the tangential or radial velocity component at the outer rim. By increasing the swirl angle the flow is found to go from a one cell to a two cell configuration, i. e., the vertical velocity changes from everywhere positive to negative in the vicinity of the axis. Correspondingly the vertical vorticity maximum moves from the axis toward the radius of maximum tangential velocity, making the flow barotropically unstable with respect to unsymmetric perturbations.

AD-A113 086   CHICAGO UNIV IL DEPT OF GEOPHYSICAL SCIENCES   F/G 4/2
THEORETICAL STUDIES OF SQUALL-LINE TYPE AND TORNADO-LIKE DISTUR--ETC(U)
DEC 81   H L KUO, W H RAYMOND, K SEITTER   F19628-80-C-0012
UNCLASSIFIED   AFGL-TR-82-0005   NL

2 of 2

END
DATE
FILMED
4-82
DTIC

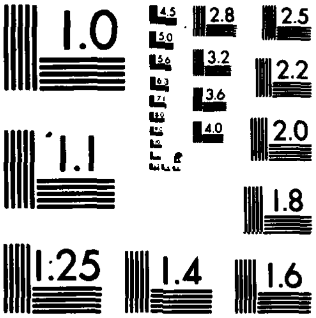

MICROCOPY RESOLUTION TEST CHART

1. Introduction

A variety of rotating or swirling motions are observed in the atmosphere. Of particular interest dynamically are the tornado type vortices. Various theories on the nature of the internal dynamics within these strong vortex flows have been discussed (e.g., see Davies-Jones and Kessler, 1974), but actual measurements are almost impossible to obtain due to the severity of the motions. To answer some of the major questions a number of laboratory vortex experiments have been conducted, e.g., Turner and Lilly (1963), Ying and Chang (1970), Ward 1972, Jischke and Parang (1974), Leslie (1977), Church _et al_. (1977), etc. One of the advantages of the modern vortex generator is its ability to reproduce the multiple vortex phenomena in an environment where it can be intensely studied, e.g., Ward (1970, 1972). Fujita (1971, 1972) first proposed that the cyloidal markings observed in tornado damage paths are produced by these secondary rotations. The presence of multiple vortices within some tornadoes has now been widely accepted and analysed in various studies, e.g. Agee _et al_. (1975) and Forbes (1978).

Because of the success of the laboratory simulations, a few elaborate numerical reproductions of the vortex generator have been attempted, e.g., Harlow and Stein (1974) and Rotunno (1977, 1979). These studies certainly have helped to identify various features of the dynamics, but questions still remain, e.g., what is the relationship between the vertical motion near the axis and the inflow angle at a large distance from the axis, and what is the nature of the instability that allows multiple vortices to generate. To help refine answers to these and other questions, a simple analytical-numerical steady-state model is investigated.

2. Formulation of the Problem

Our goal is to simulate in a simple manner a steady-state vortex similar to those produced in modern laboratory vortex generators and to study its behavior. These laboratory vortices are created mechanically in a specially designed arrangement which contains an exhaust fan and a rotating screen. Air is drawn radially inward, by the fan through the rotating screen till it reaches a central cylinder where it is allowed to rise through the cylinder and is expelled at the top.

The rotating screen imparts a background angular momentum which is nearly conserved as the air moves radially inward giving rise to a concentrated vortex core. The laboratory experiment is constructed so that it is geometrically and dynamically similar to conditions found in the atmosphere during, for example, a tornadic event. This similarity is established by requiring that the non-dimensional numbers that govern the flow in the mechanically generated vortex be in the same range as those observed in the atmosphere. Lewellen (1962) found three nondimensional parameters that govern the nature of the swirling flow. These are: the radial Reynolds number

$$Re_r = Q/2\pi\nu \quad ,$$

an internal aspect ratio

$$a = H/R \quad ,$$

and a swirl ratio

$$S = \tan\theta/2a \; .$$

Here Q is the volume flow rate per unit axial length, ν is the viscosity coefficient, H the inflow depth, R the radius of convergence and θ is the swirl or inflow angle. It is known that the swirl ratio and radial

Reynolds number describe the dynamics of the flow while the aspect ratio describes the geometry.

If all three of these numbers are of equal importance then the geometry of the simulator would have to be considered and/or duplicated in any numerical simulation. Davies-Jones (1973) however points out that the nature of the swirling flow is dominated by the swirl ratio. Because of this there is some hope that a restricted investigation ignoring the geometry and only dealing with just part of the vortex simulator, e.g. the region where convergence takes place, might be successful in explaining some of the general behavior that is observed in the laboratory vortex and thus consequently in the atmosphere. It is in this context that we adopt a similarity approach to simplify the governing equations. The procedure has been orchestrated so that we can examine the vortex flow configuration, as described in the simplified similarity equations, for a range of swirl angles.

3. The Mathematical Development

Assuming that the motion of the homogeneous fluid is steady and axisymmetric and that the Coriolis force can be neglected in comparison with the centrifugal force, then the swirling flow satisfies the following equations of motion in cylindrical coordinates (Kuo, 1966, 1969):

$$u\left(\frac{\partial v}{\partial r} + \frac{v}{r}\right) + w\frac{\partial v}{\partial z} = \nu\nabla_1^2 v \quad , \tag{1}$$

$$u\frac{\partial u}{\partial r} + w\frac{\partial u}{\partial z} - \frac{v^2}{r} = -\frac{1}{\rho}\frac{\partial p}{\partial r} + \nu\nabla_1^2 u \quad , \tag{2}$$

$$u\frac{\partial w}{\partial r} + w\frac{\partial w}{\partial z} = -\frac{1}{\rho}\frac{\partial p}{\partial z} - g + \nu\left(\nabla_1^2 w + \frac{w}{r^2}\right) \quad , \tag{3}$$

$$\frac{\partial(ur)}{\partial r} + r\,\frac{\partial w}{\partial z} = 0 \quad , \qquad (4)$$

where

$$\nabla_1^2() = \frac{\partial}{\partial r}\,\frac{1}{r}\,\frac{\partial r(\;)}{\partial r} + \frac{\partial^2}{\partial z^2}(\;)$$

r is the radial coordinate, z the vertical coordinate positive in the direction opposite to the gravitational acceleration represented by g, and u, v and w are the radial, the tangential and the axial component of velocity, p is the pressure and ρ is the density.

The velocity components u and w can be expressed in terms of the stream function ψ defined by

$$u = -\frac{1}{r}\,\frac{\partial\psi}{\partial z} \quad , \qquad w = \frac{1}{r}\,\frac{\partial\psi}{\partial r} \quad . \qquad (5a,b)$$

From Eqs. (2) and (3) we obtain the following equation for the azimuthal vorticity

$$\zeta \equiv \frac{\partial w}{\partial r} - \frac{\partial u}{\partial z} = \nabla_1^2(\psi/r) \quad : \qquad (6a)$$

$$\frac{\partial\psi}{\partial r}\,\frac{\partial}{\partial z}\,(\zeta/r) - \frac{\partial\psi}{\partial z}\,\frac{\partial}{\partial r}\,(\zeta/r) + \frac{2v}{r}\,\frac{\partial v}{\partial z} = \nu\nabla_1^2\,\zeta \quad . \qquad (6b)$$

Equations (6b) and (1) together form a closed system for the dependent variables v and ψ (after using (5a,b) and (6a) to eliminate u, w and ζ).

a. A Similarity Approach

Following the spirit of the similarity approaches utilized by Kuo (1966, 1969) the variables are first non-dimensionalized by the following transformations:

$$\psi = U_s r_s h\psi^* \quad , \qquad z = hz^*$$

$$m = U_s r_s m^* \quad , \qquad \nu = U_s r_s \nu^* \quad \text{and } x = r^2/4r_o^2 \quad . \qquad (7)$$

Here r_s is the radius of the rotating screen at the outer edge or rim, h is a measure of the effective depth, r_o is some measure in the radial direction and U_s is the radial velocity at the rim while $m = vr$ denotes the angular momentum. Note that ν^*, ψ^*, m^*, z^* and x are all dimensionless.

The dimensionless equivalent of Eq. (1) when written in terms of m^* becomes

$$-\frac{\partial\psi^*}{\partial z^*}\frac{\partial m^*}{\partial x} + \frac{\partial\psi^*}{\partial x}\frac{\partial m^*}{\partial z^*} = 2\nu^*\left[x\frac{\partial^2 m^*}{\partial x^2} + \delta^{-1}\frac{\partial^2 m^*}{\partial z^{*2}}\right] , \qquad (8)$$

while Eq. (6) reduces to

$$m^*\frac{\partial m^*}{\partial z^*} = \delta x^2\left[2\nu^*\frac{D^4\psi^*}{x} - \frac{\partial\psi^*}{\partial x}\left(\frac{D^2\psi^*}{x}\right)_{z^*} + \frac{\partial\psi^*}{\partial z^*}\left(\frac{D^2\psi^*}{x}\right)_x\right] , \qquad (9)$$

where the subscripts z^* and x denote partial differentiations and

$$\delta = h^2 r_o^{-2} , \qquad D^2\psi^* = x\frac{\partial^2\psi^*}{\partial x^2} + \delta^{-1}\frac{\partial^2\psi^*}{\partial z^{*2}}$$

and $D^4\psi^* = D^2(D^2\psi^*)$. Observe from (9) that the meridional flow is influenced by m^* only through the variation of m^* with z^*. To include this effect, we follow again the basic premise established by Kuo (1966,1969) by expanding the flow variables in power series expansions in $z^*$and including the zeroth order terms m_o and u_o in m^* and u^*. It can readily be shown that only the even order terms of z^* in m^* and u^* will contribute to these two variables and therefore we write m^* and ψ^* in the following forms

$$m^* = \nu^*[m_o + \delta z^{*2}m_1 + (\delta z^{*2})^2 m_2 + \ldots] , \qquad (10)$$

$$\psi^* = 2\nu^* z^*[F_o + \delta z^{*2}F_1 + (\delta z^{*2})^2 F_2 + \ldots] . \qquad (11)$$

Both m^* and ψ^* will be well defined provided the higher order terms are decreasing in importance.

From Eqs. (5a,b), (7), (10) and (11) we arrive at the following expressions for u, w and m:

$$u = -\frac{2\nu}{r}\left[F_o + 3\delta z^{*2}F_1 + 5\,(\delta z^{*2})^2F_2 + \ldots\right] \quad , \tag{12}$$

$$w = \frac{\nu z}{r_o^2}\left[F_o' + \delta z^{*2}F_1' + (\delta z^{*2})^2F_2' + \ldots\right] \quad , \tag{13}$$

$$m = vr = \nu\left[m_o + \delta z^{*2}m_1 + (\delta z^{*2})^2m_2 + \ldots\right] \quad . \tag{14}$$

The prime denotes differentiation with respect to x.

Using the expansions (10) and (11) in Eqs. (8) and (9) and setting the coefficients of the individual powers of δ to zero the partial differential equations are transformed into a system of coupled ordinary differential equations with independent variable x which is proportional to r^2. From the angular momentum equation (8), we obtain for m_o and m_1 the second order differential equations

$$xm_o'' + F_om_o' = -2m_1 \quad , \tag{15}$$

$$xm_1'' + F_om_1' - 2F_o'm_1 = -3F_1'm_o' - 12m_2 \quad . \tag{16}$$

From the vorticity equation (9), we find that F_o and F_1 are each defined by a fourth order differential equation,

$$\left[xF_o''' + (1+F_o)\,F_o'' - F_o'^2 + 12F_1'\right]' = \frac{m_om_1}{2x^2} - 6F_o^2\left(\frac{F_1}{xF_o}\right)' - \frac{120F_2}{x} \quad , \tag{17}$$

$$\left[xF_1''' + (1+F_o)F_1'' - 4F_o'F_1' + 3F_o''F_1\right]' + 6x^2\left(\frac{F_1^2}{x^3}\right)'$$
$$= \frac{1}{x^2}\left(m_om_2 + \frac{1}{2}m_1^2\right) - 20F_o\left(\frac{F_2}{x}\right)' + 60\frac{F_o'F_2}{x} - 40F_2'' - \frac{840F_3}{x} \quad . \tag{18}$$

Equations for the higher order terms in (10) and (11), can also be obtained but are not presented here. The system of equations becomes closed for any given cut-off limit.

5. Solution by perturbation expansion

Instead of treating the system of highly coupled nonlinear equations (15) - (18) directly, we shall solve them by expanding the dependent variables in powers of a coupling parameter α so as to separate the most fundamental part $F_{oo}(x)$ of $F_o(x)$ in (17) from the other variables to make F_{oo} satisfy an uncoupled equation, and obtain the coupling parts of the various functions by successive approximation. The expansions which serve this purpose can be written as

$$F_o = F_{oo} + \alpha F_{01} + \alpha^2 F_{02} + \dots \quad , \tag{19}$$

$$m_o = m_{oo} + \alpha m_{01} + \alpha^2 m_{02} + \dots \quad ,$$

$$F_1 = \alpha F_{10} + \alpha^2 F_{11} + \alpha^3 F_{12} + \dots \quad ,$$

$$m_1 = \alpha m_{10} + \alpha^2 m_{11} + \alpha^3 m_{12} \dots \quad ,$$

$$F_2 = \alpha^2 F_{20} + \alpha^3 F_{21} + \dots \quad ,$$

$$m_2 = \alpha^2 m_{20} + \alpha^3 m_{21} + \dots \quad , \text{ etc.}$$

Substituting these expansions in Eqs. (15) - (18) and equating the coefficients of the various powers of α to zero we then obtain the following system of equations: (first set)

$$[xF'''_{oo} + (1 + F_{oo})F''_{oo} - F'^2_{oo}]' = 0 \; , \tag{20}$$

$$[xF'''_{10} + (1 + F_{oo})F''_{10} - 4F'_{oo}F'_{10} + 3F''_{oo}F_{10}]' = 0 \; , \tag{20b}$$

$$xm''_{oo} + F_{oo}m'_{oo} = 0 \quad , \tag{20c}$$

$$xm''_{10} + F_{oo}m'_{10} - 2F'_{oo}m_{10} = -3F_{10}m'_{oo} \tag{20d}$$

(second set)

$$\left[xF'''_{01} + (1 + F_{oo})F''_{01} - 2F'_{oo}F'_{01} + F''_{oo}F_{01}\right]'$$

$$= \frac{1}{2x^2}\, m_{oo}m_{10} - 6F^2_{oo}\left(\frac{x^{-1}F_{10}}{F_{oo}}\right)' - 12F''_{10} \quad , \tag{21a}$$

$$\left[xF'''_{11} + (1 + F_{oo})F''_{11} - 4F'_{oo}F'_{11} + 3F''_{oo}F_{11}\right]' = -\,(F_{01}F''_{10} - 4F'_{01}F'_{10} + 3F''_{01}F_{10})'$$

$$+ \frac{1}{2x^2}(m^2_{10} + 2m_{oo}m_{20}) - 6x^2\left(\frac{F^2_{10}}{x^3}\right)' - 20F_{oo}\left(\frac{F_{20}}{x}\right)'$$

$$+ 60\,\frac{F'_{oo}F_{20}}{x} - 40F'_{20} \quad , \tag{21b}$$

$$xm''_{01} + F_{oo}m'_{01} = -\,F_{01}m'_{oo} - 2m_{10} \quad , \tag{21c}$$

$$xm''_{11} + F_{oo}m'_{11} - 2F'_{oo}m_{11} = -F_{01}m'_{10} + 2F'_{01}m_{10} - 3(F_{10}m'_{01} + F_{11}m'_{oo}) - 12m_{20} \quad , \tag{21d}$$

(Set 3, limited to F_{02} and m_{02} for brevity)

$$\left[xF'''_{02} + (1 + F_{oo})F''_{02} - 2F'_{oo}F'_{02} + F''_{oo}F_{02}\right]' = \frac{1}{2x^2}(m_{oo}m_{11} + m_{01}m_{10})$$

$$+ \left[-F_{01}F''_{01} + F'^2_{01}\right]' - 6F^2_{oo}\left(\frac{F_{11}}{xF_{oo}}\right)' - 6F^2_{01}\left(\frac{F_{10}}{xF_{o1}}\right)' - 120\,\frac{F_{20}}{x} \quad , \tag{22a}$$

$$xm''_{02} + F_{oo}m'_{02} = -2m_{11} - F_{01}m'_{01} - F_{02}m'_{oo} \quad . \tag{22b}$$

Eqs. (20a) and (20c) are found in Kuo (1966, 1969) while (21b) and (21d) differ somewhat from that given by Kuo due to the different δ used. Observe that Eq. (20a) is nonlinear but it contains F_{oo} alone, hence it can be solved together with the boundary conditions to yield F_{oo}, while all the other equations are linear and contain lower order functions as coefficients and non-homogeneous terms. Notice also that the inclusion of the F_1 term in (11) makes the tangential and the radial velocities coupled through equations (20d) to (22b).

c. The Boundary Conditions

At the axis we require that each of the variables be zero for the axisymmetric flow, i.e., at x = 0

$$m_{0i} = F_{0i} = 0 \quad , \quad i = 0,1, \ldots \qquad (23)$$
$$m_{1i} = F_{1i} = 0 \quad , \quad i = 0,1, \ldots$$

At the rim, $x = x_s$, we assume the vertical velocity is zero, that the radial inflow will vary slightly with height while the rotation rate does not vary in the vertical. Also, we shall take all the radial inflow and rotation in the first term in the α expansion, and none in the higher perturbations. Therefore at x_s the solutions satisfy

$$F'_{0i} = 0 \quad , \quad i = 0,1,\ldots, \qquad (24)$$
$$F_{0i} = 0 \quad , \quad i = 1,2,\ldots,$$
$$F'''_{0i} = 0 \quad , \quad i = 0,1,\ldots,$$
$$m_{0i} = 0 \quad , \quad i = 1,2,\ldots,$$
$$F'_{1i} = 0 \quad , \quad i = 0,1,\ldots,$$
$$F_{1i} = 0 \quad , \quad i = 1,2,\ldots,$$
$$F'''_{1i} = 0 \quad , \quad i = 0,1,\ldots,$$
$$m_{1i} = 0 \quad , \quad i = 0,1,\ldots,$$

while F_{00}, F_{10} and m_{00} are assigned non-zero values. The condition on the third derivative is needed to complete the requirement of four boundary conditions for the fourth order equations. Integrating (20a) from 0 to x_s, applying the boundary conditions given above and solving for $F''_{00}(x_s)$ yields

$$F''_{00}(x_s) = \frac{F''_{00}(0) - F'^{2}_{00}(0)}{(1+F_{00}(x_s))} \quad . \qquad (25)$$

This relation shows that $F''_{00}(x_s)$ is non-zero if $F''_{00}(0) \neq F'^{2}_{00}(0)$. A similar procedure applied to Eq. (20b) reveals that

$$F''_{10}(x_s) = \frac{F''_{10}(0) - 4F'_{oo}(0)F'_{10}(0) - 3F''_{oo}(x_s)F_{10}(x_s)}{(1 + F_{oo}(x_s))} , \tag{26}$$

which is also non-zero if the numerator is non-zero.

At the rim the swirl angle θ can be written in terms of m_o and F_o since Eqs. (12), (14) and the boundary conditions (24) give at the $z^* = 0$ level

$$\theta = - \tan^{-1}(v/u) = \tan^{-1}(m_o/2F_o) .$$

Note also at the rim we have $m_o(x_s) = m_{oo}(x_s)$ and $F_o(x_s) = F_{oo}(x_s)$.

d. Details of the Numerical Procedure

The non-linear ordinary differential equations described by Eqs. (20), (21) and (22) with their corresponding boundary conditions (23) and (24) are solved numerically, in the order listed above, using a shooting technique (Conte and de Boor, 1972). Each equation is rewritten as a system of first order equations and then discretized using the midpoint rule (Kreiss and Oliger, 1973). Thus, e.g., each fourth order equation is reduced to a system of four first order equations that must be solved iteratively. A fine grid is employed near the axis, e.g., $\Delta x = 10^{-4}$, but this spacing is allowed gradually to expand to a much coarser net near the rim, say $\Delta x = 10^{-1}$. As an example, a total of 575 grid points are used on the interval $x = 0$ to 20. Tests using nearly double this number of grid points yields no significant differences.

Utilizing a shooting technique to solve the fourth order differential equations for the various F's requires that initially a guess be made for the first and second derivatives at $x = 0$. Using these guesses the third derivative at $x = 0$ is then computed directly from the equation. The system of four first order equations are solved for all x using standard procedures and then the values for $F_{i,j}$ and its first derivative at $x = x_s$

are compared with the desired boundary conditions. If the differences exceed a specified small value, say 10^{-5}, the process is again repeated using new estimates to replace the values of the first and second derivatives at $x = 0$. These new values are obtained using Muller's method (Conte and de Boor, 1972).

We have only two degrees of freedom so the condition on the third derivative at the rim can not be strictly enforced but we except only those solutions for which the required condition is naturally approximately satisfied, i.e., $F'''_{i,j} \simeq 0$, $i = 0,1,\ldots$, $j = 0,1,\ldots$ The error introduced by this procedure is quite small since, e.g., the calculated value of $F''_{oo}(x_s)$ varies from that predicted by Eq. (25) typically only in the fourth significant decimal place.

Our equations actually possess multiple solutions that satisfy all the above stated boundary conditions, e.g., two separate solutions for F_{oo}, Eq. (20a), are known to exist and more may be possible. Using initial guesses with $F'_{oo}(0) > 0$ and $F''_{oo}(0) < 0$ we obtain a solution which contains all positive values of F'_{oo} (one cell vortex) while the second solution, obtained using initial guesses $F'_{oo}(0) < 0$ and $F''_{oo}(0) > 0$, contains negative values of F'_{oo} near the axis and positive values further away (two cell vortices). Kuo (1967), examining a vortex in an unstably stratified atmosphere, shows similar two cell solutions for the special case when all the derivatives are zero at the rim. Our two cell solutions remain essentially unchanged near the axis as the rim is moved further and further away. This behavior is not observed in the laboratory vortex (Ward, 1972 and Church et al., 1979), so in this study we disregard this solution and utilize only initial guesses that satisfy $F'_{oo}(0) > 0$ and $F''_{oo}(0) < 0$. The exact magnitude for these choices depends on the strength of the inflow at the rim.

The solution of the m equation is straight forward and does not change significantly with the change of the vertical velocity at the axis and therefore it will not be presented here.

4. Discussion of Results

In this study a similarity approach is utilized to obtain the solution of the two-dimensional nonlinear vortex equations for comparison with the results obtained from laboratory vortex simulators, so that the vertical and radial variations are uncoupled. For simplicity, the geometry of the vortex simulator is ignored and only the nature of the flow within the convergence or inflow region is investigated for a range of swirl angles. Care must be exercised in interpreting our results however since the similarity transform ignores the geometry and by limiting this study to within the convergence region we also ignore the source of the convergence, i.e., the exhaust fan, and thus there is no guarantee that different rim rotation rates, with the same specified radial inflow, will experience the same volume flow rate. Fortunately Davies-Jones (1973) has shown that within the experimental ranges for the three nondimensional quantities, namely, the radial Reynolds number, the aspect ratio and the swirl ratio, it is the swirl ratio that most strongly controls the laboratory vortex flow configuration. In our calculations some small variations of the aspect ratio and radial Reynolds number are inherent because of the nature of the similarity approach but these changes are thought to be minimal and should not distort the general conclusions. Also our model includes the viscous or diffusion terms but does not include the boundary layer explicitly since the motion predicted at $z^* = 0$ is non-zero and not the no-slip flow required in boundary layer theory. The zero value for z^* should be interpreted as occurring near the top of the surface boundary layer.

We will vary the boundary conditions at the rim ($x = x_s$) representing changes in the strength of the radial velocity or inflow ($F_{00}(x_s)$), the vertical variation of the radial velocity component ($F_{10}(x_s), F_{20}(x_s), \ldots$)

and the strength of the rotation or tangential velocity ($m_{oo}(x_s)$), and observe the predicted flow pattern. Note that the height dependency is determined by the first and higher order terms in Eq. (11) and is established by the choice of boundary conditions at the rim. Results will be presented normally for two boundary parameters fixed while the third is varied over some range. The resulting flows may not always be observed since in the laboratory vortex there may be some natural compensation at the rim in the vertical variation, for example, as changes occur there in either the strength of the radial inflow or rotation rate. Nevertheless we can clearly show the trends produced by individual changes in these boundary parameters.

Our results illustrated in Figs. 1 through 11 are displayed in terms of the dimensional radial variable $r = r^*$ or in $(r^*)^{1/2}$ scale to better visualize the predicted flow pattern near the axis. The first 10 figures are for an intense vortex similar to those produced in modern laboratory vortex simulators. The outer rim is located at $r^*(x_s) = 1.932$ m while the last figure shows a weaker configuration with maximum radius of 0.642 m. Because the intensity of the inflow and rotation at the outer rim greatly effects the location of the maximum tangential velocity in the x coordinate an appropriate choice for r_o must be established for each of the two cases to convert our calculations in x back into $r = r^*$ scale. The scaling factor r_o is calculated once for each case via the formula $x_{vmax} = r^2_{vmax} \cdot (2r_o)^{-2}$ by selecting 0.15 m as the appropriate radius for the maximum tangential velocity, in approximate agreement with laboratory simulations (Church <u>et al</u>., 1979). Both radii given above correspond to a maximum value for x of 20. This value is selected as typical from a large number of tests. Using numerical results representative of each case the scaling factor for the more intense flow is determined as $r_o = 0.215$ m while the weaker case uses $r_o = 0.0728$ m. The equations for F_o, m_o, ..., themselves are independent of r_o, δ and ν but to convert back to the dimensional variables requires some appropriate choices. The radial distance is labeled r* in the figures indicating that our choice of r_o has been used to convert from the x coordinate back into the dimensional $r = r^*$ coordinate.

Radial profiles of F'_o and its components are shown in Fig. 1. These are computed using $F_{oo}(x_s) = 250$, $F_{10}(x_s) = -0.8$ and $m_{oo}(x_s) = 194$ and are presented in a uniform $(r^*)^{1/2}$ scale. F'_o and its components should be interpreted as a measure of the vertical velocity (Eq. 13). The solid curve labeled F'_{oo}, obtained from (20a) has its maximum value at the axis, i.e. $r^* = 0$, and by itself is typical of the profile found in a one-cell vortex (Kuo, 1966). When higher order expansion terms, obtained from Eqs. (21a) and (22a) are included in $F'_o = F'_{oo} + \alpha F'_{01} + \alpha^2 F'_{02}$ with α taken as one, the profile is radically different since $F'_o \approx 0$ at $r^* = 0$ and thus represents the initial stage of a two cell vortex. The latter is generally characterized by negative vertical velocities at and near the axis with non-negative values further away. For our purposes three terms will be sufficient to approximate F_o or F'_o, since e.g., the dotted curve representing F'_{02} is significantly smaller in magnitude than either F'_{oo} or F'_{01} indicating the decreasing importance of higher order terms in the α expansion. Higher order terms in the (δz^{*2}) power series expansion Eqs. (10) and (11) like F_1, where $F_1 = \alpha F_{10} + \alpha^2 F_{11}$, are similarly much smaller than the zeroth-order terms. Note that $10.F'_{10}$ as plotted in Fig. 1 is still small in magnitude. The second term in F_1, i.e. F_{11}, is even smaller. We will neglect the very small contributions of F_2 and other higher order terms.

Included in Fig. 1 is the dashed-dot curve showing the radial profile of F'_o when terms generated by vertical diffusion are removed from the calculations. The resulting differences in F'_o are clearly small as seen by comparing the dashed-dot and solid curves and do not change the two cell nature of the vortex which results when radial and tangential motions are coupled. Our calculations show that as the vortex becomes more intense this small contribution is reduced even further (not displayed) while in the convergence region of a weak vortex vertical variations are more pronounced so that vertical diffusion becomes more important, as shown in Fig. 11. In this weaker vortex configuration, Fig. 11, the ratio of F_{10}/F_{oo} at x_s is an order of magnitude larger than that used to compute the more intense vortex described in Figs. 1 through 10.

According to Hall (1972) the vortex core is characterized, above the boundary layer, by a slight spreading out of the core with height hence a small decrease in radial and tangential velocities with height and the development of an adverse pressure gradient.

We tune our model to produce similar behavior by choosing F_1 as minutely negative at the rim, hence negative over the entire radius, giving an increasingly negative contribution with increasing height to the radial velocity component and consequently to the tangential velocity. Fig. 2 shows that the value of F_o' is sensitive to changes in F_1 since non-zero F_1 values allow the tangential velocity and radial motions to be coupled. If F_1 is identically zero everywhere then F_o will be identically F_{oo}, i.e., the radial motion becomes independent of the rotation rate. The magnitude of F_1 is chosen so that the coupling effects of F_1 and m_1 produce nearly zero values at the axis for F_o', solid line, when the swirl angle, $\theta = \tan^{-1} m_o/2F_o$, is in the neighborhood of twenty degrees in approximate agreement with results found in laboratory simulations (Church et. al., 1979, Church and Snow 1979).

In Fig. 3, radial profiles of F_o' are presented for four different rotation rates at the rim, i.e., with $m_{oo}(x_s) = 170, 194, 240$ and 280 while $F_{oo}(x_s) = 250$ and $F_{10}(x_s) = -0.8$ are each held fixed. This is equivalent to varying the swirl angle at the rim from 18.78° to 29.25° ($z^* = 0$) by adjusting the tangential velocity. It should be noted that laboratory simulations measure their swirl angle somewhere between the rotating screen and the updraft core and not at the rim exactly. For the smaller value of $m_{oo}(x_s)$ of 170 the F'_o profile, given by the dashed curve, is positive throughout the entire radius but already significantly reduced near the axis as seen when compared with the solid curve labeled F'_{oo} which does not include the coupling effect of the tangential flow. As the rotation rate is increased F'_o becomes increasingly smaller at the axis and is nearly zero when $m_{oo}(x_s) = 194$ (solid line). Further increases in the rotation rate produce negative F'_o values at the axis typical of the two celled vortex. Note that the profile away from the axis, say $r* > 0.25$ m, remains almost uneffected by variations in the swirl angle. In the laboratory simulator where the volume flow rate is unchanged in the experiment there would be somewhat more of an increase in this outer region, of the order of 10%, to compensate for the downwatf motion at the axis. Thus our results for increasing values of m_o at the boundary have a small *decreasing volume flow rate* for the same radial inflow rate. This may be interpreted as having a slightly decreasing aspect ratio and radial Reynolds number. Consequently the swirl ratio S will increase more than that predicted due to changes in the swirl angle alone since S is inversely proportional to the aspect ratio.

In Fig. 4 values of $x^{-1/2}F_o$, which is proportional to the radial velocity, are given up to a radius of 0.28 m. The two cell flow is very evident in the dashed-dot ($m_{oo} = 240$) and dotted curves ($m_{oo} = 280$) since both have negative values next to the axis. The solid curve labeled $x^{-1/2}F_{10}$ shows the smallness of the negative first order term when compared with zero order terms.

The development of the downward vertical motion at the axis is clearly seen to descend from high levels of z, in agreement with laboratory findings (Church et al. 1979), since negative vertical motion is possible when small positive zeroth-order and negative first-order terms are combined provided at some $z* > 0$

the expression $|\delta z^{*2}F_1'| > F_o'$ in Eq. (13) is first satisfied. This occurs when F_o' is much subdued but still positive at the axis, e.g., as does occur as shown in Fig. 3. The combination of zeroth and first order terms would then lead to a reduction with height in the vertical velocity, a stagnation or zero point and finally negative vertical motion above that level. This type of motion is clearly seen in the laboratory simulations of the vortex (Church et al., 1979, Ward 1972).

Profiles of the tangential velocities are shown in Fig. 5 for the same cases discussed in Figs. 3 and 4. As the swirl angle at $z^* = 0$ is increased in value for four cases between 18.78 to 29.25°, corresponding to the dashed through dotted curves respectively, the tangential velocity maximum moves further from the axis, a feature commonly observed in laboratory simulations (Church et al., 1979). *Outside the radius of maximum tangential flow* the shapes of the profiles are very similar. This follows since the value of the zeroth order angular momentum, $m_o = v_o r$, remains nearly constant. For example with a value of 194 at the rim the value of m_o is 192.8 at $r^* = 0.2422$m which is very close to the radius of maximum velocity at 0.15m. This means that the vertical velocity is confined within a region certainly less than twice the radius of the maximum tangential velocity. The flow behavior very near the axis is in a state of near solid rotation thus F_o, m_o, ... each are nearly proportional to x as shown in Table 1 for the case $m_{oo}(x_s) = 194$. Obviously the slope there will vary as the swirl angle is changed. Note that as $m_o(x_s)$ is increased from 170 to 194, dashed and solid line respectively in Fig. 5, the slope of the tangential velocity is slightly reduced near the axis but enhanced as it approaches its maximum value. Further increases in the swirl angle continue to steepen the slope just inside the radius of maximum velocity.

The tangential velocity is observed to become negative in the region of the core where the two cell vortex contains negative vertical velocity and outward radial velocity and hence gives rise to an advective loss of angular momentum in the core. In the laboratory simulator the downward motion at the axis in the two cell vortex appears to descend downward through the baffling near the top of the vortex generator down to the lower surface. Obviously our model which is restricted to the convergence region of the vortex cannot duplicate this behavior. The configuration given by the dashed-dot and dotted curves in Fig. 5, representing predicted rotational flow for a two celled vortex, will give rise to inertial instability since the gradient of the circulation changes signs (Rayleigh, 1916 and Synge, 1938).

Another type of instability is revealed in Fig. 6 by the radial profiles of m_o', here m_o' is proportional to the vertical vorticity and the prime denotes a derivative with respect to x. Even for the smaller boundary value of $m_{oo}(x_s) = 170$ (dashed curve) the gradient of m_o' changes sign revealing that the flow configuration is barotropically unstable. The slope of the uncoupled or zeroth order term m_{oo}' is of the same sign thus the instability portrayed in other curves arises because of the coupling effect of the radial and vertical flows back on the tangential motion. Note that the maximum value for m_{oo}' occurs at the axis while in the other curves, representing m_o' for increasing swirl angles, the maxima are achieved progressively further away from the axis and closer to the tangential velocity maxima. In fact these maxima occur where the gradient of the tangential velocity is very large as seen when comparing Figs. 5 and 6. These results indicate that azimuthally varying three-dimensional disturbances precluded from the present axisymmetric model will be created under these unstable conditions, which will even out the negative vorticity and negative rotation in the core to make them not observable in laboratory simulation. The possibility that the barotropic instability of the tangential flow profile may lead to generation of suction vortex type disturbance in tornadoes as suggested by Fujita (1972) has been investigated by Staley and Gall (1979). Snow (1978) has postulated the other alternative, i.e., an inertial instability.

Table 1. Values of F_o, F_1, m_o, m_1 and their components at two locations near the axis. All F and m values are to be multiplied by 10^{-5}.

x	r*	F_{oo}	F_{01}	F_{02}	F_{10}	F_o	F_1	m_o
0.0001	0.0043	196	-146	-49	-0.6	1.1	-0.9	13736
0.001	0.01359	1976	-1453	-499	-6.4	15.0	-8.6	109742

x	m_1
0.0001	-165
0.001	-1625

The radial profile of the scaled velocity magnitude ($|V|\nu^{-1} \cdot 10^{-2}$) at level $z = 0$ and its tangential and radial component are represented by the continuous, the dashed and the dotted curves in Fig. 7 respectively. This form of presentation is taken since a conversion to actual velocity would require the knowledge of the viscosity coefficient ν. Our model predicts less than a four-fold increase in the velocity magnitude from the rim to its maximum value. This appears to agree very well with laboratory simulations (Church et al., 1979). Also note that the radial component's contribution to the velocity magnitude is very small inside the radius of maximum tengential velocity but dominates near the rim.

For very small swirl angles (not shown), our model, in agreement with laboratory findings (Snow et al., 1980) gives weakly swirling flows without a central core. In this case the tangential component increases with radius right up to the rim.

Radial profiles proportional to the vertical velocity, the tangential velocity and the vertical vorticity are shown in Fig. 8 through 10, respectively. Three different values of the swirl angle ranging from 17.92 to 23.32° ($z^* = 0$) are used by varying the radial inflow component while keeping the rotation rate at the rim constant. As the boundary value of F_{oo} is decreased from 300 (dashed curve) to 225 (dotted curve) while $m_{oo}(x_s) = 194$ and $F_{10}(x_s) = -0.8$ are each held constant, the vertical flow is found to change from all positive values to the two cell configuration, in agreement with what happens as the swirl angle is increased. Correspondingly, the tangential velocity (Fig. 9) shows a decrease in magnitude with an outward expansion of the radius of the maximum value in accordance with the law of conservation of angular momentum. The curves in Fig. 10 show a similar pattern to that discussed earlier for the vertical vorticity.

Our equations are non-linear so the nature of their solutions might vary somewhat as the magnitudes of the boundary values are varied but we find that for a large range of boundary conditions they still behave similarly. A weaker flow configuration using $F_{oo}(x_s) = 25$ is shown in Fig. 11, but even in this case it still is possible to have the vertical velocity change from all positive (dashed line, $m_{oo}(x_s) = 10$) to that found in a two-celled vortex (dotted line, $m_{oo}(x_s) = 30$) by changing the tangential velocity at the rim. No negative tangential velocities are generated for this case where the swirl angle is varied from 11.31 to 30 .96°. Tests using $F_{oo}\ (x_s) = 500$ also generate the two-celled vortex with the appropriate choices of $m_{oo}(x_s)$. Note that when our results are converted into actual velocities the choice for the value of viscosity, used in scaling the equation, does not determine the nature of the flow since the same flow characteristics are found over a broad range of boundary values.

5. Conclusion

In this study a model of the convergence region of a laboratory vortex is investigated via a similarity approach. The predicted flow is shown to vary significantly only near the axis as the swirl angle at the outer rim is changed. This type of response appears to be exactly similar to that observed in the laboratory. Of course, not all the details of the flow found in the laboratory vortex generator can be reproduced here, but the nature or trend of changes predicted in this study appears to be generally valid.

Acknowledgement: This research is supported by Air Force Geophysics Laboratory through Contract No. F19628-80-C-0012.

References

Agee, E.M., C.R. Church, C. Morris and J.T. Snow, 1975: Some synoptic aspects and dynamic features of vortices associated with the tornado outbreak of 3 April 1974. Mon. Wea. Rev., 103, 318-333.

Church, C.R., J.T. Snow and E.M. Agee, 1977: Tornado vortex simulation at Purdue University. Bull. Amer. Meteor. Soc., 58, 900-908.

_____________, and J.T. Snow, 1979: The dynamics of natural tornadoes as inferred from laboratory simulations, J. Rech. Atmos., 13, 111-133.

_____________, J.T. Snow, G.L. Baker and E.M. Agee, 1979: Characteristics of tornado-like vortices as a function of swirl ratio: a laboratory investigation. J. Atmos. Sci., 36, 1755-1776.

Conte, S.D., and C. deBoor, 1972: Elementary Numerical Analysis: An Algorithmic Approach. McGraw-Hill, New York, 396 pp.

Davies-Jones, R.P., 1973: The dependence of core radius on swirl ratio in a tornado simulator. J. Atmos. Sci., 30, 1427-1430.

_____________, and E. Kessler, 1974: Tornadoes, Weather and Climate Modification, W.N. Hess, Ed., Wiley, 842 pp. (See chap. 16).

Forbes, G.S., 1978: Three scales of motion associated with tornadoes. Ph.D. Thesis, Univ. of Chicago, Chicago, Illinois. 359 pp. [Available from National Technical Information Service, Springfield, Virginia 22161.]

Fujita, T.T., 1971: Proposed mechanism of suction spots accompanied by tornadoes. Preprint, Seventh Conf. Severe Local Storms, Boston: Amer. Meteor. Soc. pp. 208-213.

______________, 1972: Proposed mechanism of suction spots accompanied by tornadoes. SMRP Research Paper No. 102, The University of Chicago, 14pp.

Hall, M.G., 1972: Vortex breakdown. *Ann. Rev. Fluid Mech.*, *4*, 195-213.

Harlow, F.H. and L.R. Stein, 1974: Structural analysis of tornado-like vortices. *J. Atmos. Sci.*, *31*, 2081-2098.

Jischke, M.C., and Parang, 1974: Properties of simulated tornado-like vortices. *J. Atmos. Sci.*, *31*, 506-512.

Kreiss, H., and J. Oliger, 1973: Methods for the approximate solution of time dependent problems. WMO II CSN Joint Organizing Committee, GARP Publication Series No. 10, 107 pp.

Kuo, H.L., 1966: On the dynamics of convective atmospheric vortices. *J. Atmos. Sci.*, *23*, 25-42.

_________, 1967: Note on the similarity solutions of the vortex equations in an unstably stratified atmosphere. *J. Atmos. Sci.*, *24*, 95-97.

_________, 1969: Axisymmetric flows in the boundary layer of a maintained vortex. University of Chicago, Planetary Circ. Proj., Rept. No. 15, 54 pp.

Leslie, F.W., 1977: Surface roughness effect on suction vortex formation: a laboratory simulation. *J. Atmos. Sci.*, *34*, 1022-1027.

Lewellen, W.S., 1962: A solution for three-dimensional vortex flows with strong circulation. *J. Fluid Mech.*, *14*, 420-432.

Rayleigh, Lord, 1916: On the dynamics of revolving fluids. *Proc. Roy. Soc. London*, A93, 148-154.

Rotunno, R., 1977: Numerical simulation of a laboratory vortex. *J. Atmos. Sci.*, *34*, 1942-1956.

__________, 1979: A study of tornado-like vortex dynamics. J. Atmos. Sci., 36, 140-155.

Snow, J.T., 1978: On inertial instability as related to the multiple-vortex phenomenon. J. Atmos. Sci., 35, 1660-1677.

__________, C.R. Church and B.J. Barnhart, 1980: An investigation of the surface pressure fields beneath simulated tornado cyclones. J. Atmos. Sci., 37, 1013-1026.

Staley, D.O., and R.L. Gall, 1979: Barotropic instability in a tornado vortex. J. Atmos. Sci., 36, 973-981.

Synge, J.L., 1938: On the stability of a viscous fluid between rotating coaxial cylinders, Proc. Roy. Soc. London Ser. A, 167, 250-256.

Turner, J.S., and D.K. Lilly, 1963: The carbonated water tornado vortex. J. Atmos. Sci., 20, 468-471.

Ying, S.J., and C.C. Chang, 1970: Exploratory model study of tornado-like vortex dynamics. J. Atmos. Sci., 27, 3-14.

Ward, N.B., 1970: The exploration of certain features of tornado dynamics using a laboratory model. NOAA Tech. Mem. ERLTM-NSSL 52, 22 pp.

__________, 1972: The exploration of certain features of tornado dynamics using a laboratory model. J. Atmos. Sci., 29, 1194-1204.

List of Figures

Fig. 1. Radial profiles of F'_o which is proportional to the vertical velocity, and its components are given. F_{10} is also displayed. First subscript denotes the δz^2 expansion while the second indicates location in α expansion. Boundary values: $F_{oo} = 250$, $m_{oo} = 194$ and $F_{10} = -0.8$. Dashed-dot curve is F'_o when vertical diffusion is ignored.

Fig. 2. Radial profiles of F'_o computed using three different boundary values for F_{10}, i.e. (solid) $F_{10} = -0.8$, (dotted) $F_{10} = -1.1$ and (dashed) $F_{10} = -0.6$. Other boundary values same as in Fig. 1.

Fig. 3. Radial profiles of F'_o computed for four different swirl angles obtained by varying the tangential velocity. Boundary values used are (solid) $m_{oo} = 194$, (dashed) $m_{00} = 170$, (dashed-dot) $m_{oo} = 240$ and (dotted) $m_{oo} = 280$. Other boundary values same as in Fig. 1.

Fig. 4. Same as Fig 3 except showing $x^{-1/2}F_o$, which is proportional to the radial velocity, on a linear scale near the axis.

Fig. 5. Same as Fig. 3 except showing $x^{-1/2}m_o$ which is proportional to the tangential velocity.

Fig. 6. Same as Fig. 3 except showing m'_o which is proportional to the vertical vorticity.

Fig. 7. Radial profiles (time 10^{-2}) of $(u^2+v^2)^{1/2}\nu^{-1}$ (solid), $v\nu^{-1}$ (dashed) and $u\nu^{-1}$ (dotted). Boundary values same as used in Fig. 1.

Fig. 8. Radial profiles of F'_o for three swirl angles obtained by varying the radial velocity component. Boundary values: (solid) $F_{oo} = 250$, (dashed) $F_{oo} = 300$ and (dotted) $F_{oo} = 225$. Other boundary values same as Fig. 1.

Fig. 9. Same as Fig. 8 except showing $x^{-1/2}m_o$.

Fig. 10. Same as Fig. 8 except showing m_o'.

Fig. 11. Radial profiles of F_o' for three swirl angles. Computed using boundary values (solid) $m_{oo} = 20$, (dashed) $m_{oo} = 10$ and (dotted) $m_{oo} = 30$. Otherwise $F_{oo}(x_s) = 25$ and $F_{10}(x_s) = -0.3$. The dashed-dot curve is F_o' when vertical diffusion is ignored.

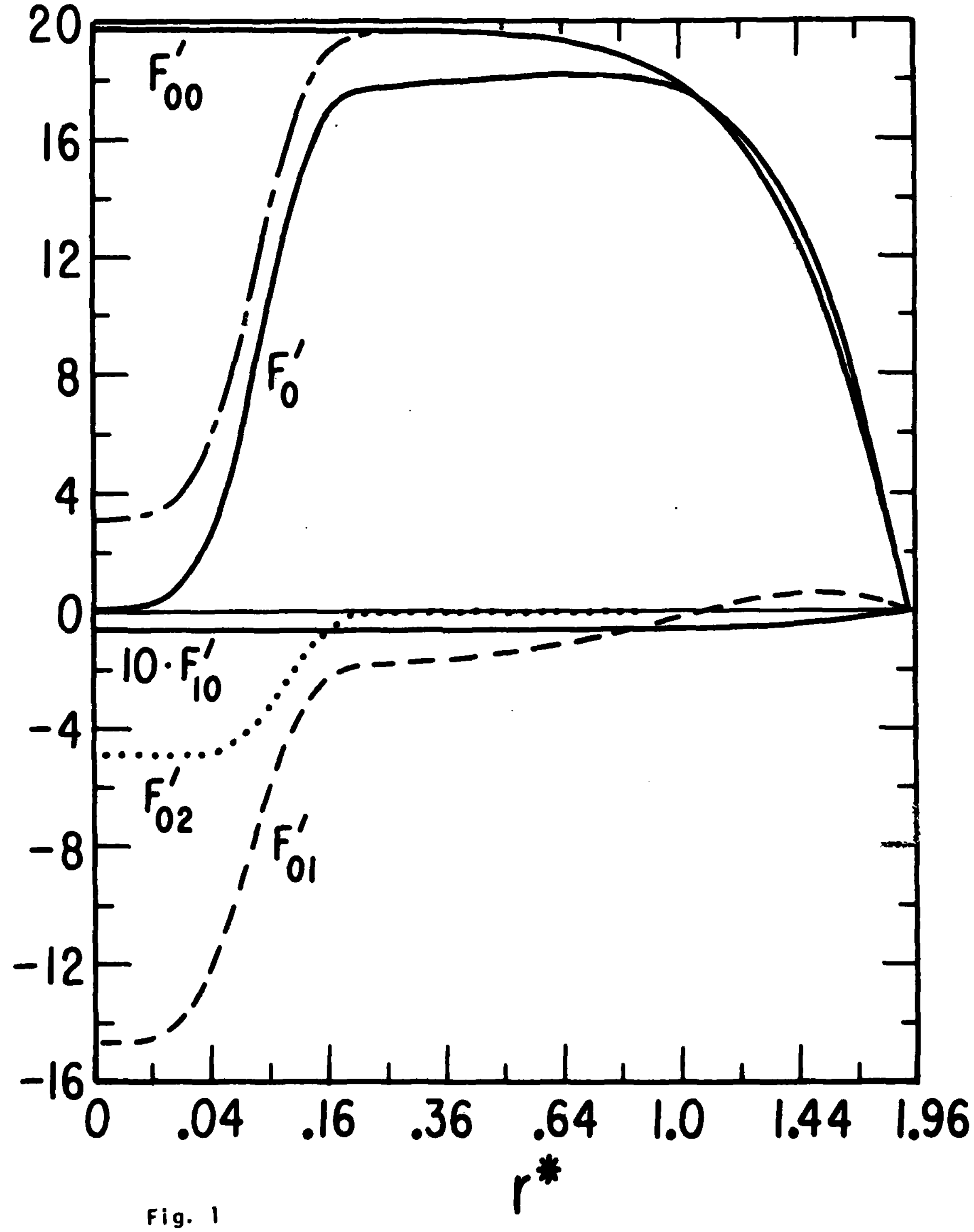
20
16
12
8
4
0
-4
-8
-12
-16
F'_{00}
F'_0
$10 \cdot F'_{10}$
F'_{02}
F'_{01}
0
.04
.16
.36
.64
1.0
1.44
1.96
r^*

Fig. 1

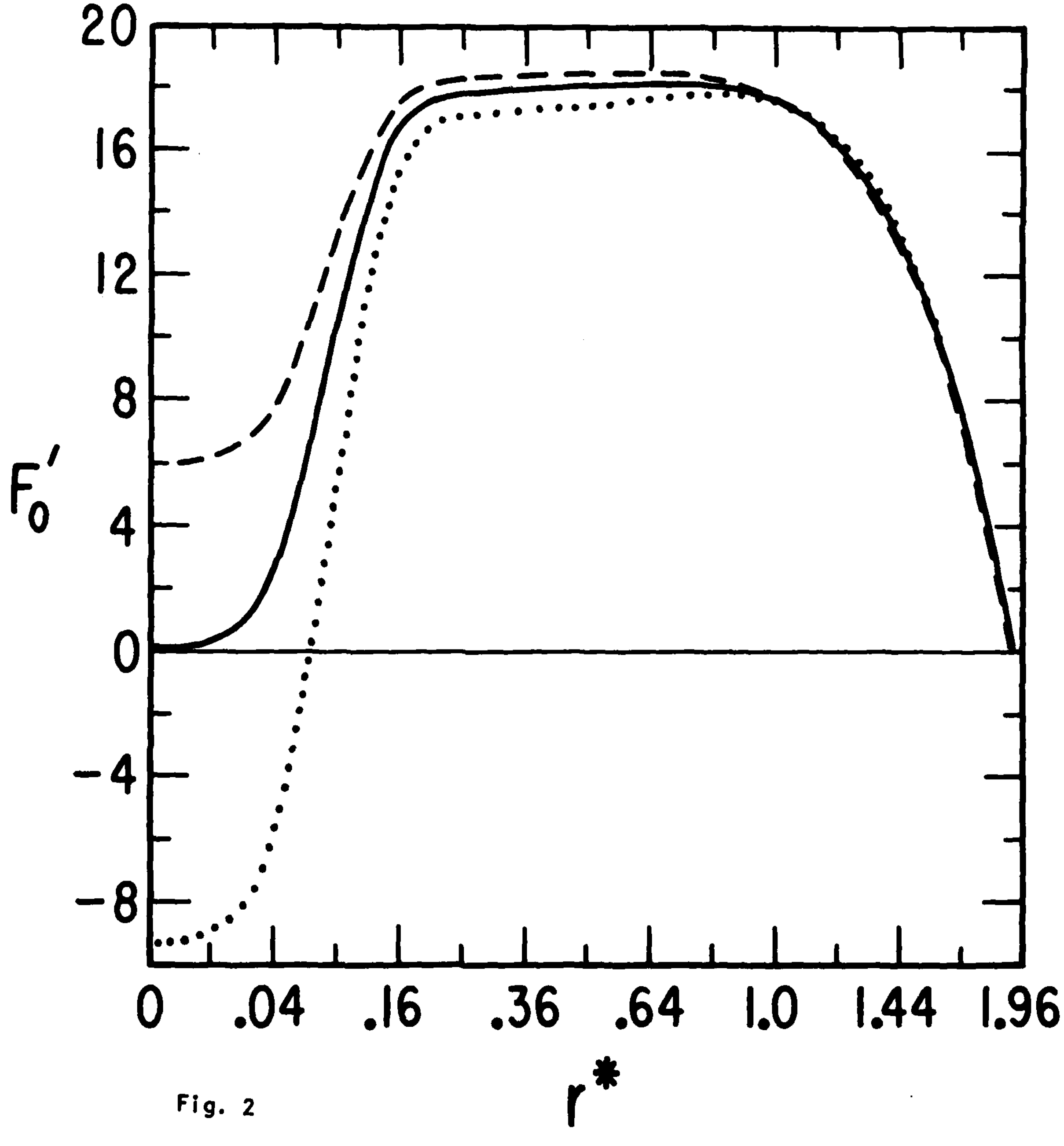

Fig. 2

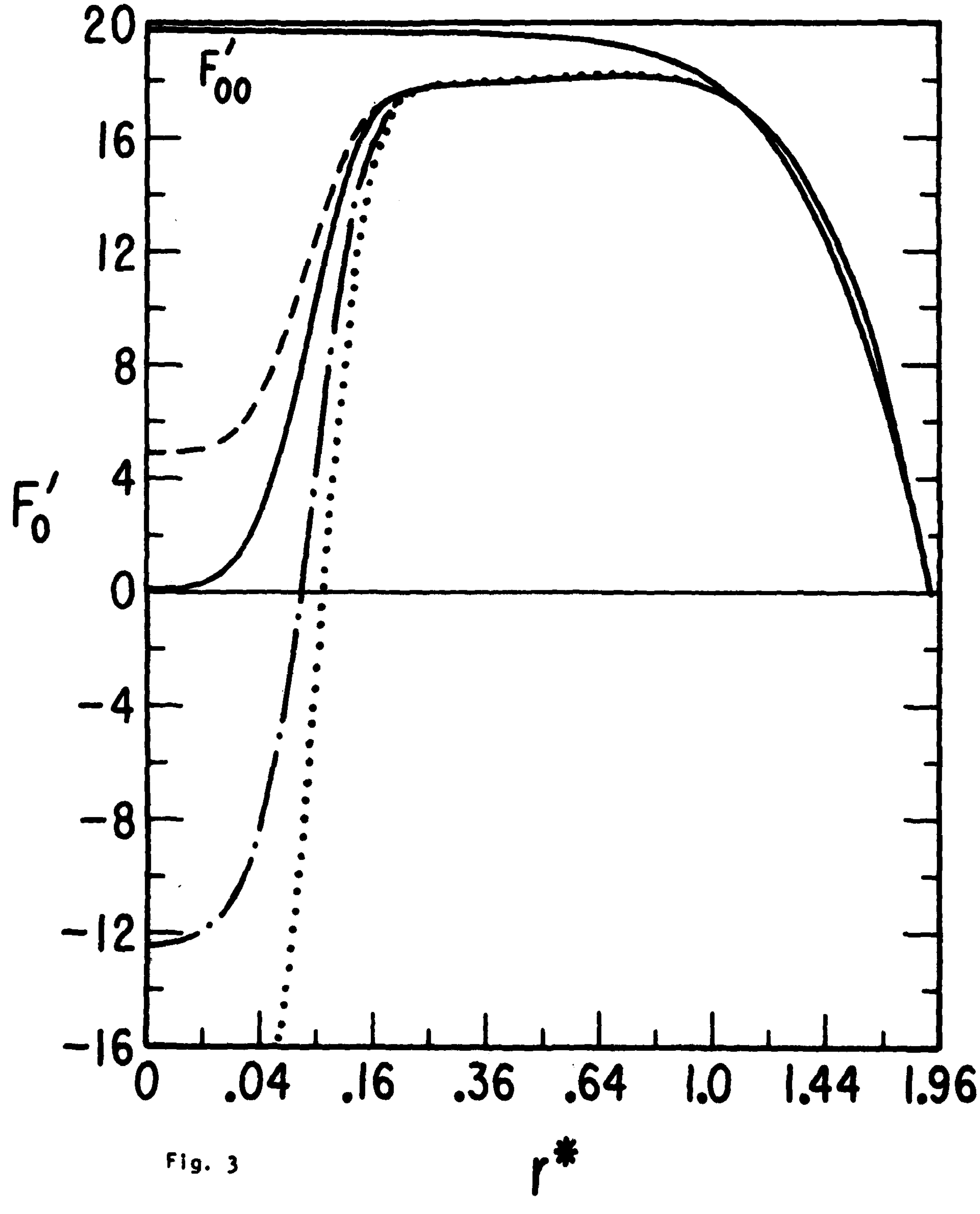

Fig. 3

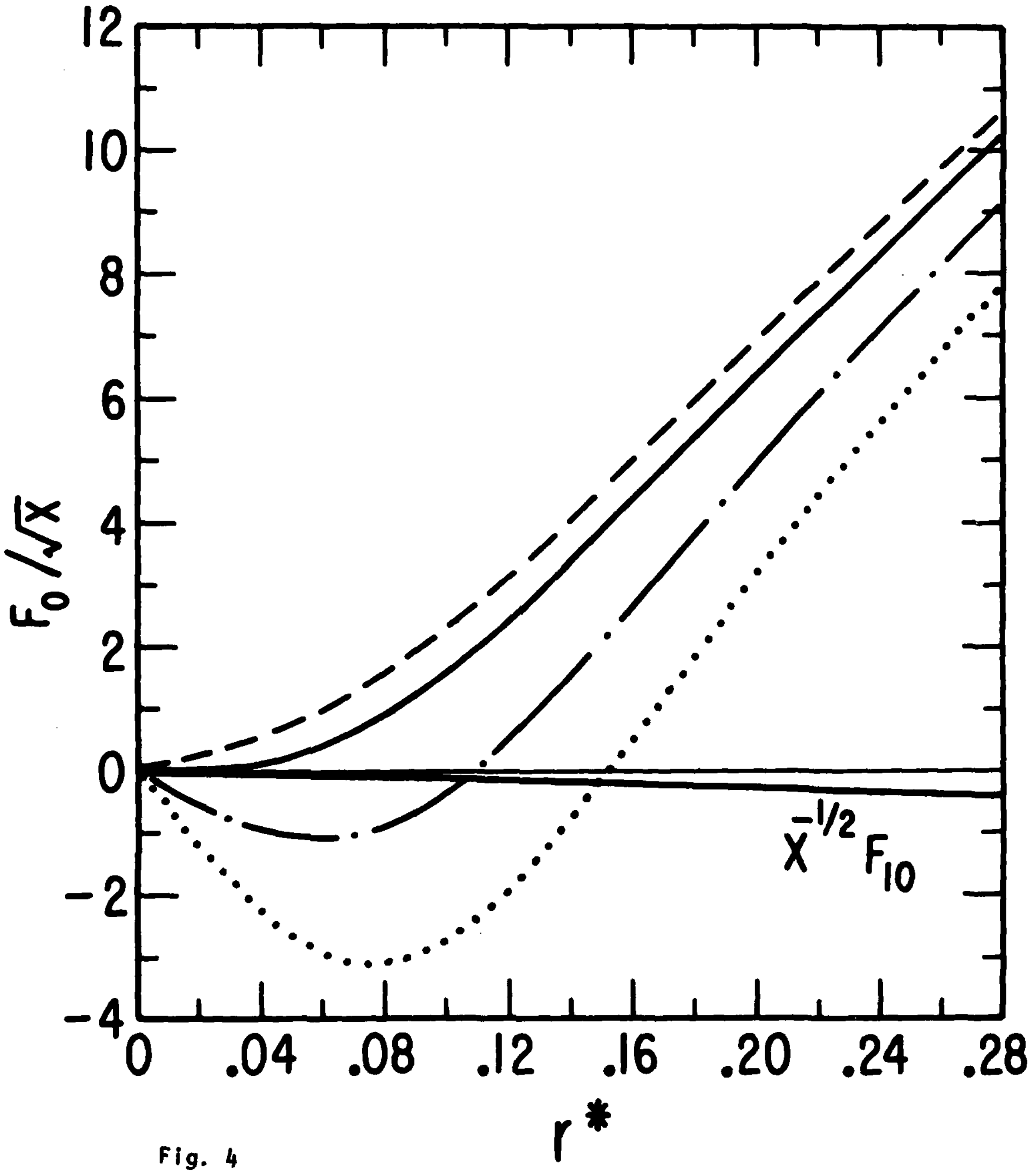

Fig. 4

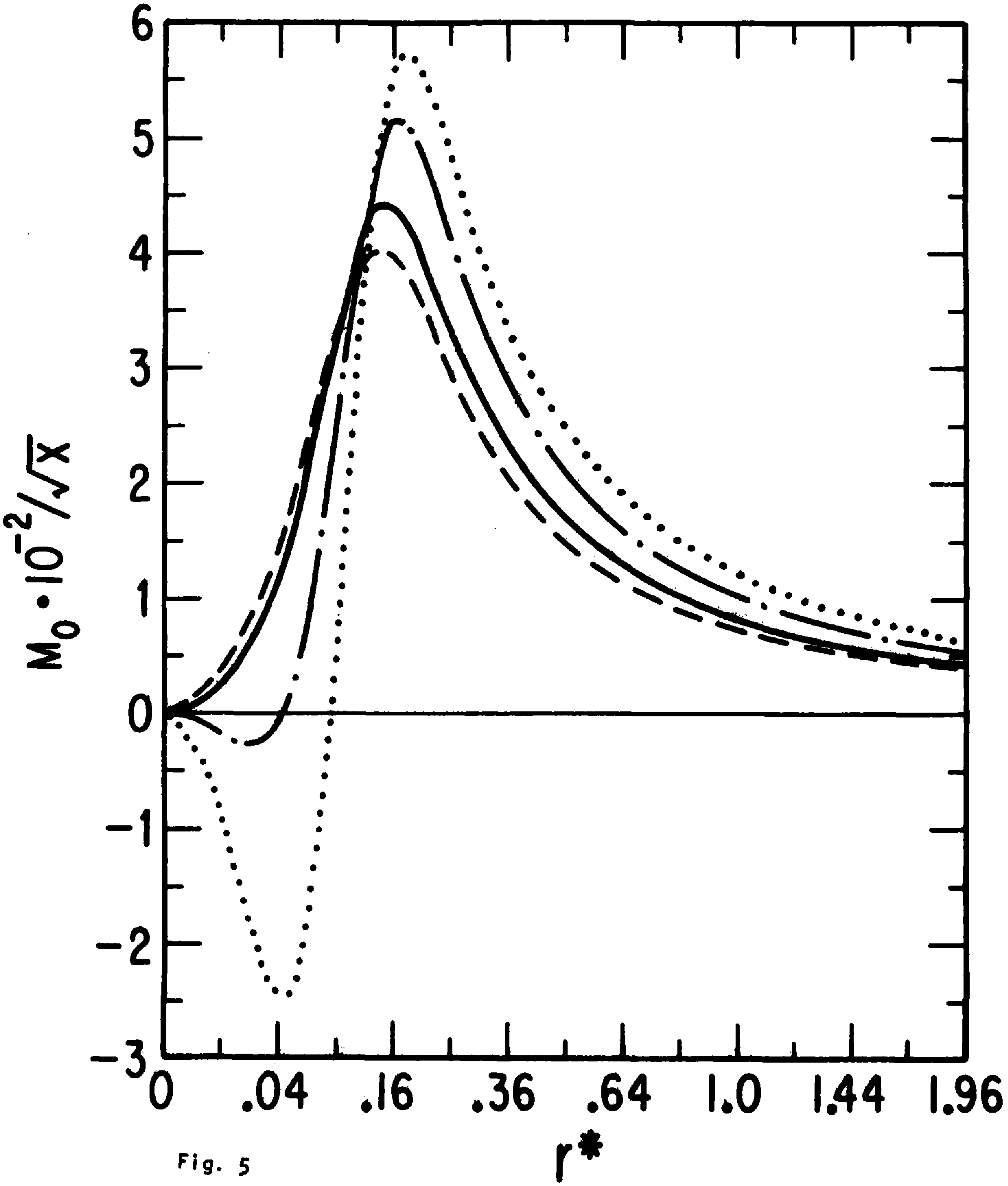

Fig. 5

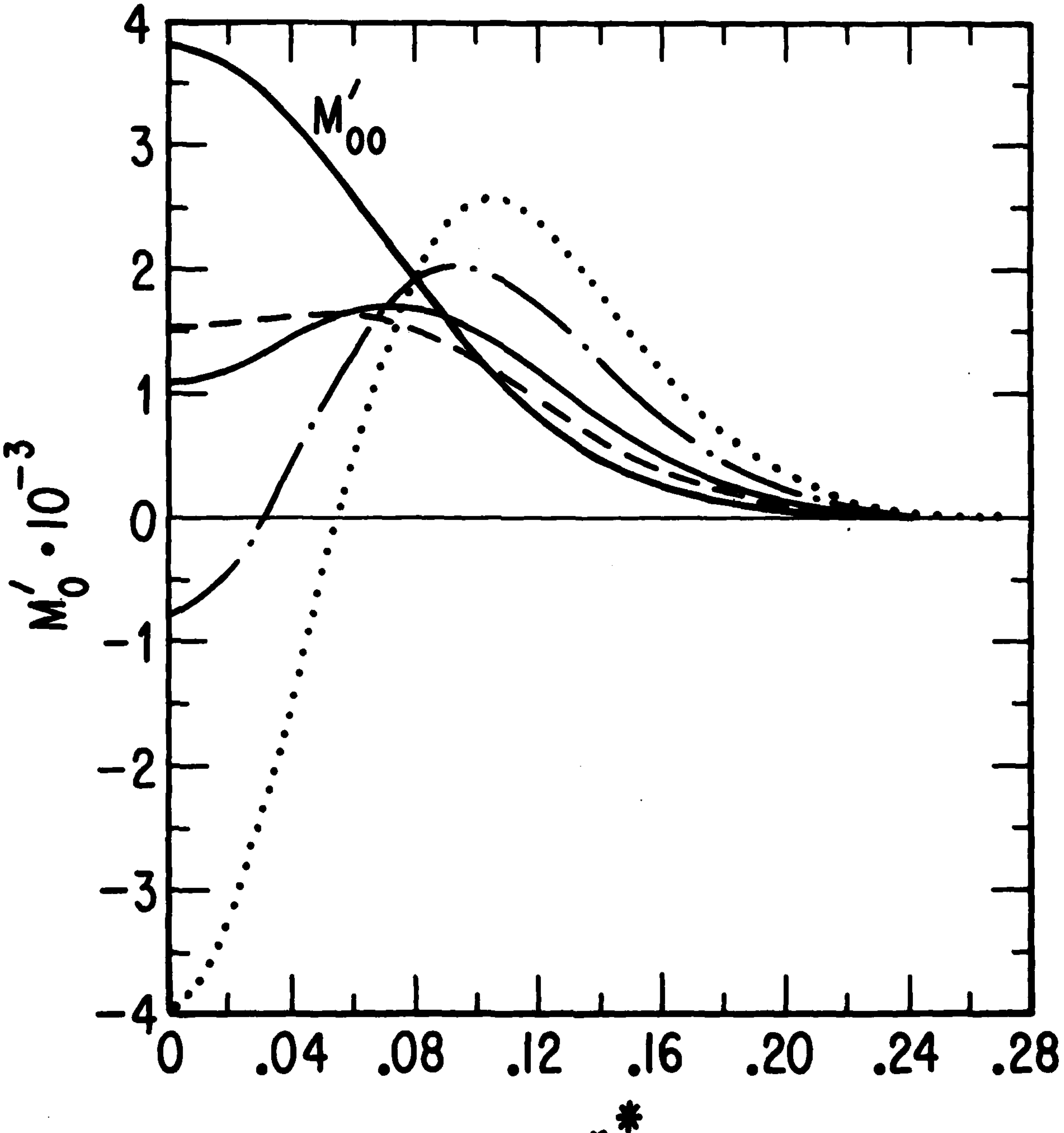

Fig. 6

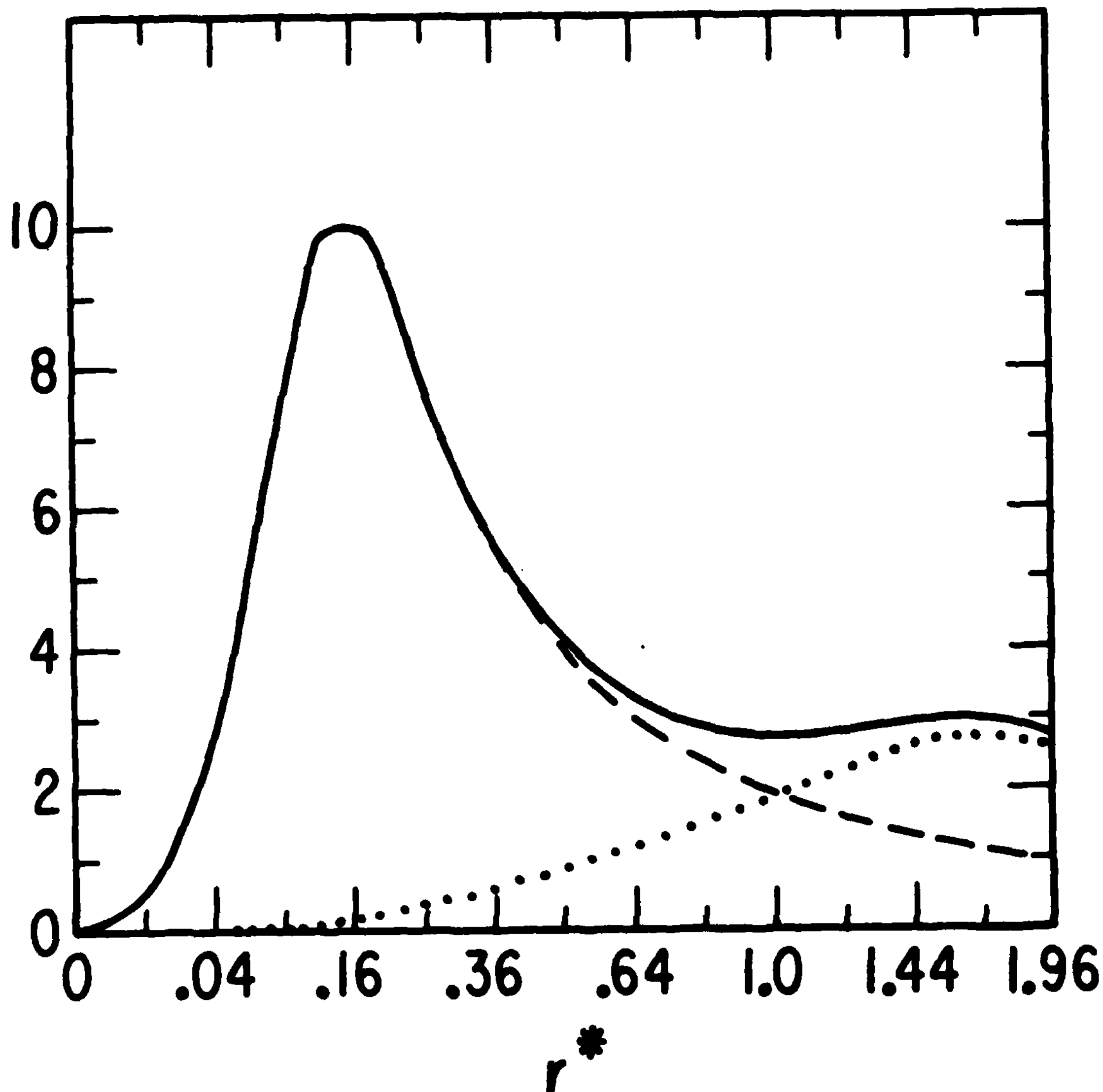

Fig. 7

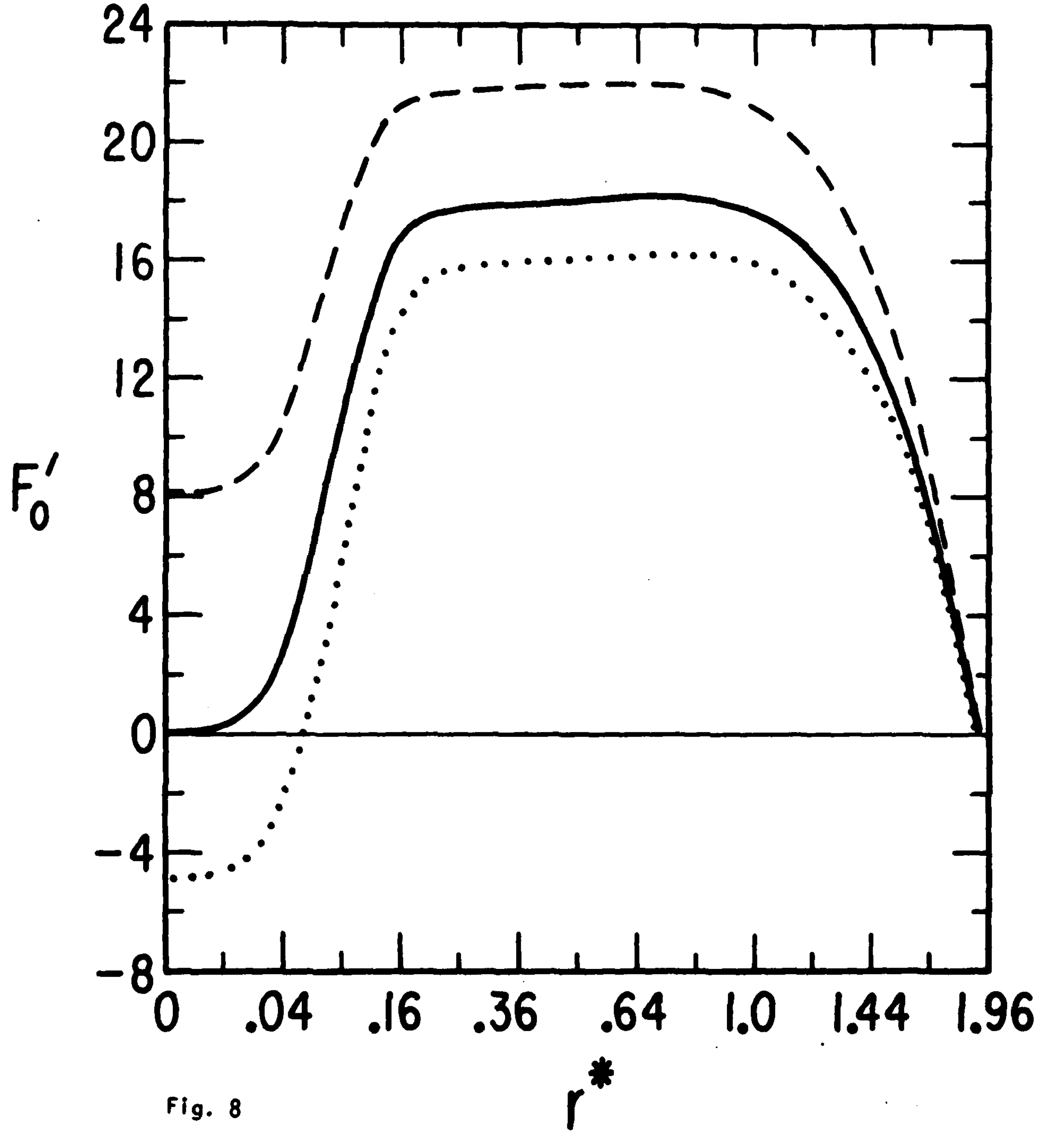

Fig. 8

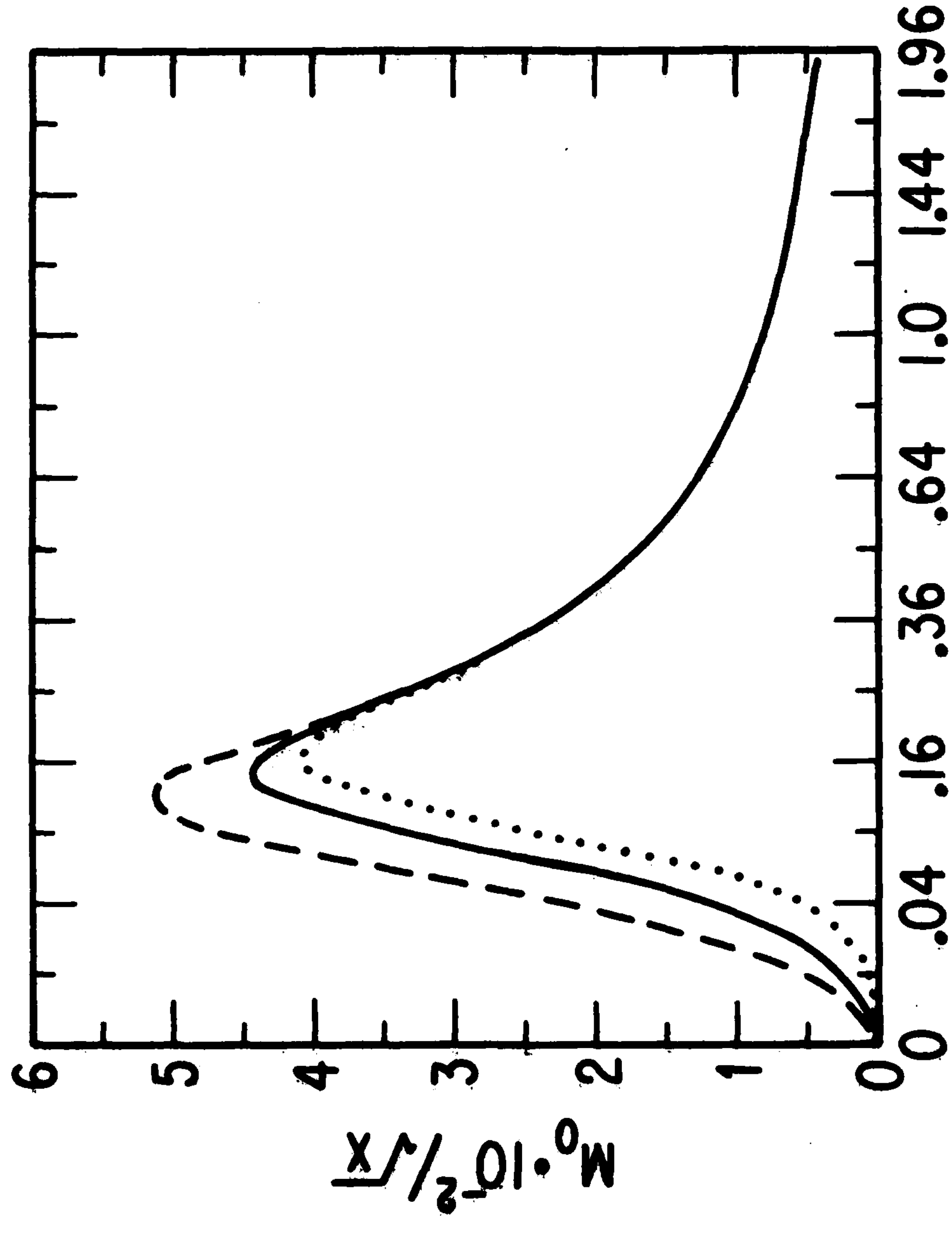

Fig. 9

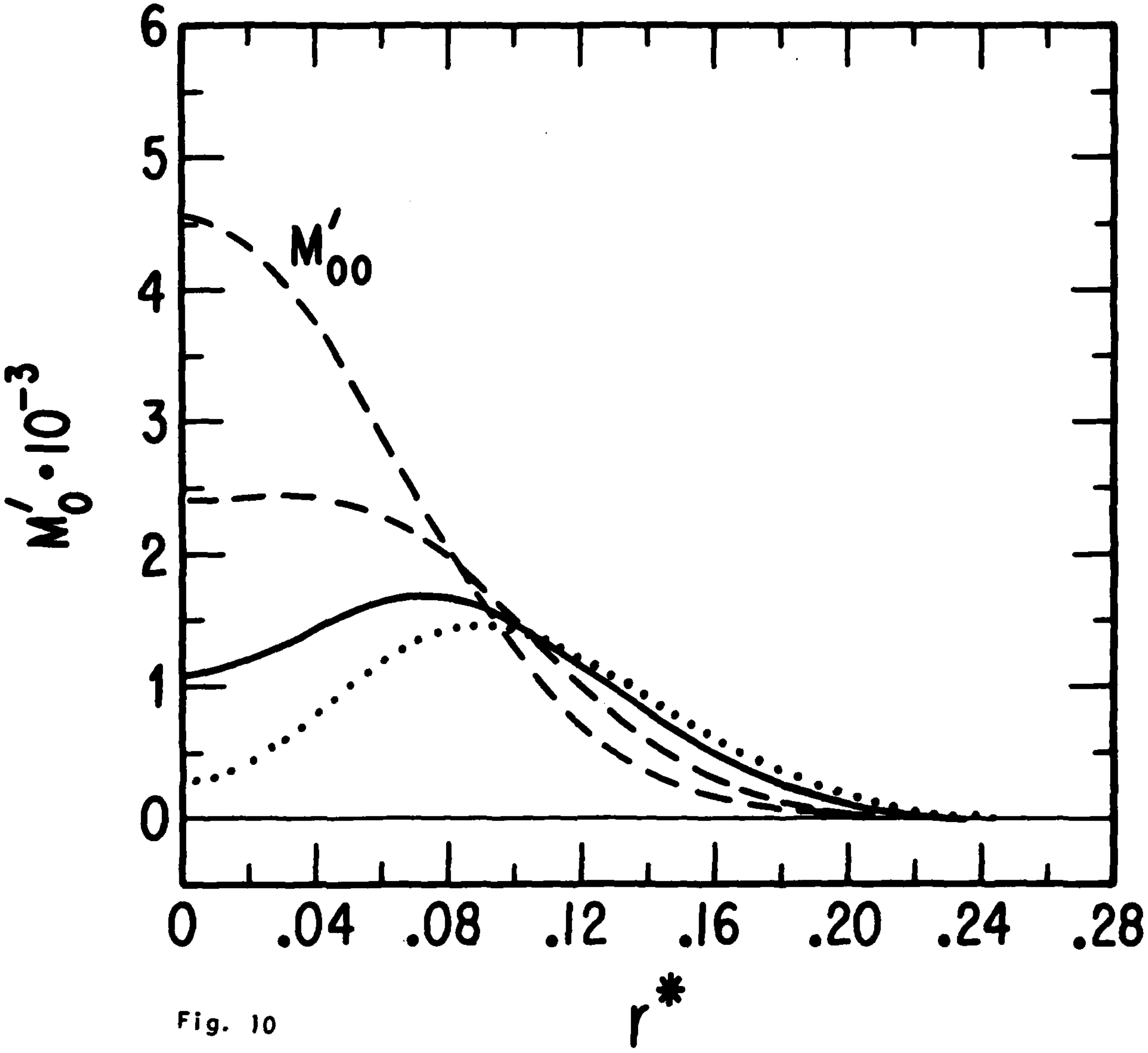

Fig. 10

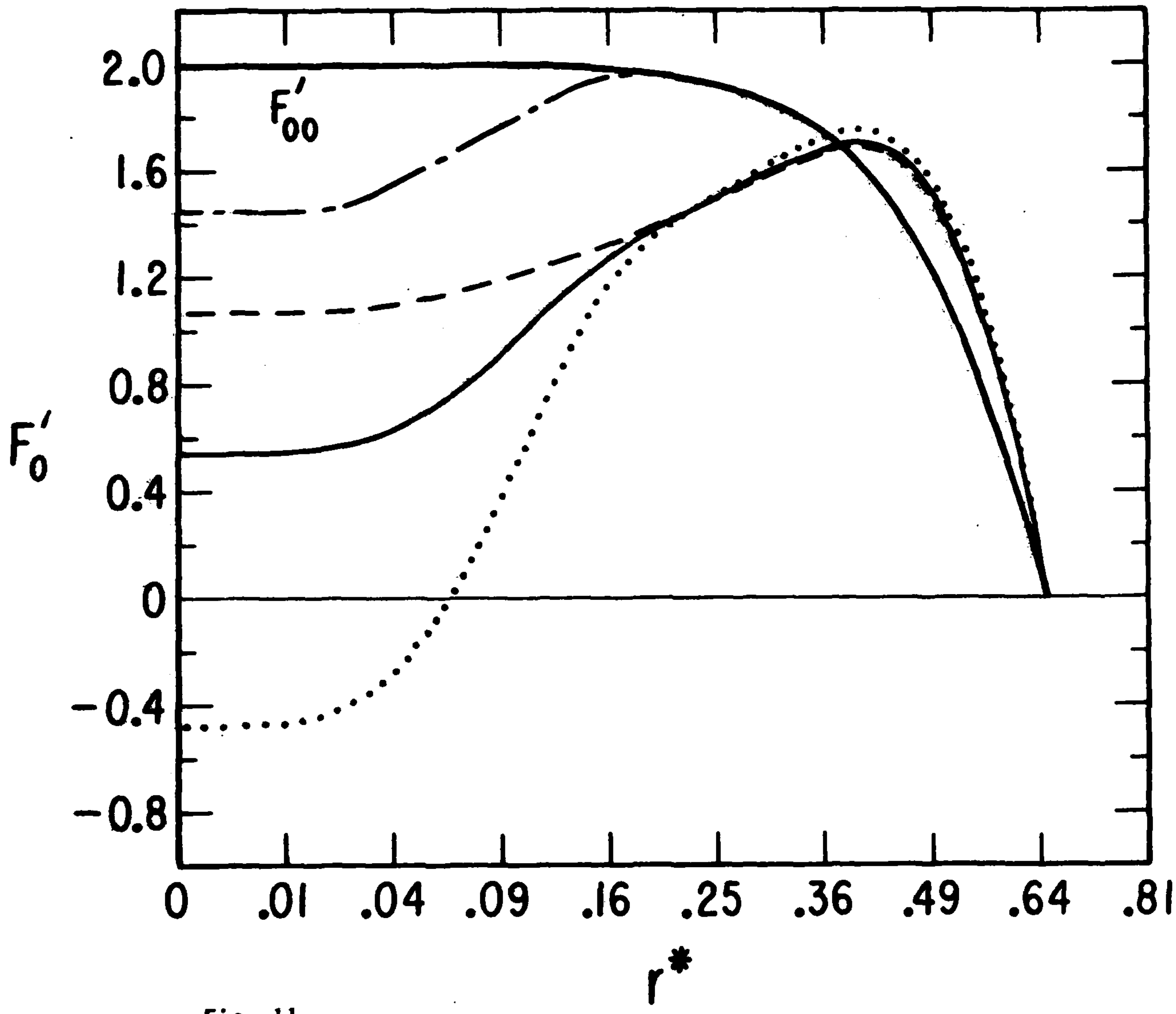

Fig. 11